Title

Distinguishing molecular environments in supported Pt catalysts and their influences on activity and selectivity

Author

Jones, Louis Chin

Publication Date

2014

UNIVERSITY OF CALIFORNIA

Santa Barbara

Distinguishing molecular environments in supported Pt catalysts and their influences on activity and selectivity

A dissertation submitted in partial satisfaction of the
requirements for the degree Doctor of Philosophy
in Chemical Engineering

by

Louis Chin Jones

Committee in charge:

Professor Michael Gordon, Co-Chair

Professor Bradley Chmelka, Co-Chair

Professor Eric McFarland

Professor Horia Metiu

June 2014

The dissertation of Louis Chin Jones is approved.

Horia Metiu

Eric McFarland

Bradley Chmelka, Co-Chair

Michael Gordon, Co-Chair

June 2014

Distinguishing molecular environments in supported Pt catalysts and their influences on activity and selectivity

by

Louis Chin Jones

ACKNOWLEDGEMENTS

The Universe, all that is in it, a part of it, responsible for it, and especially the Light that fills it, both seen & unseen...Thank you for Being, allowing Us to become Ourselves

To my wonderful Mom & Dad...who made & Love their Chinese-American Alloy. Thank you for always supporting me, and for everything you have given & continue to give. This is only one of the many things that we will always share. Love Us Always!

To mi Katita, for saving my life many times over, freeing me from the dungeon, and being mi Lova...Thank you for being the woman of my dreams, many more adventures await us!

To my advisors, professors, and educators that lead me here...Thank you for the challenge and opportunity to learn so much about the Universe, Myself, and Others. I hope we can work together again...I won't forget your teachings.

To everyone I've had the pleasure of meeting in the UCSB ChE department, & to all to the Music sessions & Church communions, & to my Bruddah(wo)men all around the world...Let's keep going, we'll all be together soon!!!

VITA OF LOUIS CHIN JONES

March 2014

EDUCATION

Bachelor of Science in Chemical Engineering (Chemistry Minor), University of California, Berkeley, May 2008
Doctor of Philosophy in Chemical Engineering, University of California, Santa Barbara, March 2014

PROFESSIONAL DEVELOPMENT

2005-2008: Research Assistant, Lawrence Berkeley National Laboratory, University of California, Berkeley
2009-2012: Teaching Assistant, Department of Chemical Engineering, University of California, Santa Barbara

PUBLICATIONS

M. Koebel, L. C. Jones, & G. Somorjai. "Preparation of size-tunable, highly monodisperse PVP-protected Pt-nanoparticles by seed-mediated growth." *J. Nanoparticle Res.* **10**, 1063-1069 (2008).

Y. Borodko, L. Jones, H. Lee, H. Frei, & G. Somorjai. "Spectroscopic Study of Tetradecyltrimethylammonium Bromide Pt-C_{14}TAB Nanoparticles: Structure and Stability." *Langmuir* **25**, 6665-6671 (2009).

L. J. Giovanetti, J. M. Romallo-López, M. Foxe, L. C. Jones, M. M. Koebel, G. A. Somorjai, A. F. Craievich, M. B. Salmeron, & F. G. Requejo. "Shape changes of Pt nanoparticles induced by deposition on mesoporous silica." *Small* **8**, 468-473 (2012).

L. C. Jones, Z. Buras, & M. J. Gordon. "Partial Hydrogenation of C_2H_2 on Ag-Doped Pt Nanoparticles." *J. Phys. Chem. C* **116**, 12982-12988 (2012).

L. C. Jones & M. J. Gordon. "Influence of Step-Edge vs. Terrace Sites on Temperature-Dependent C_2H_2 Hydrogenation with Ag-Doped Pt Nanoparticles." *J. Phys. Chem. C* **116**, 23472-23476 (2012).

S. H. Donaldson Jr., S. Das, M. Gebbie, M. Rapp, L. C. Jones, Y. Roiter, P. Koenig, Y. Gizaw, & J. Israelachvili. "Asymmetric electrostatic and hydrophobic-hydrophilic interaction forces between mica surfaces and silicone polymer thin films." *ACS Nano* **7**, 10094-10104 (2013)

L. C. Jones, M. J. Gordon, & B. F. Chmelka. "Measuring distinct molecular ^{195}Pt environments of surface platinum species in bulk and supported Pt oxides and sulfides." *To be submitted.*

M. Soorholtz, D. Samuelis, C. Weidenthaler, L. C. Jones, B. F. Chmelka, R. J. White, M.-M. Titirici, D. Cullen, T. Zimmermann, M. Antonietti, J. Maier, R. Palkovits, & F. Schüth."Local compositions and structures of a heterogeneous analogue to Periana's homogeneous Pt catalyst." *To be submitted.*

AWARDS

Alumni Scholar, University of California, Berkeley, 2004

National Science Foundation, Partnership for International Research & Education - Electron Chemistry & Catalysis at Interfaces, Santa Barbara, 2010

National Science Foundation, Integrative Graduate Education & Research Traineeship, Santa Barbara, 2012-2013

FIELDS OF STUDY

Studies of Fe nanoparticles under high pressure aqueous conditions with Prof. Mario Farias & Dr. Matthias Koebel

Pt nanoparticle synthesis and activity for ethylene hydrogenation with Dr. Matthias Koebel

Pt nanoparticle surfactant evolution and site characterization using *in situ* infrared spectroscopy with Dr. Yuri Borodko

Alloy nanoparticle synthesis, *in situ* molecular characterization, and automated catalytic testing with Prof. Michael Gordon and Prof. Bradley Chmelka

OUTREACH

Oasis Tutoring: Math & English elementary school tutor, Oakland, CA, 2005

Research Mentor: Advised UCSB students (5) in nanoparticle research, 2008-2013

Discover Engineering Weekend: Mentor local Santa Barbara High School students to build alternative energy vehicles, 2009 & 2011

Materials Research Laboratory K-12 Science Activities: Buckyball Workshop, Solar Car Workshop, It's a Material World, 2012-2013

ABSTRACT

Distinguishing molecular environments in supported Pt catalysts and their influences on activity and selectivity

by

Louis Chin Jones

This thesis entails the synthesis, automated catalytic testing, and *in situ* molecular characterization of supported Pt and Pt-alloy nanoparticle (NP) catalysts, with emphasis on how to assess the molecular distributions of Pt environments that are affecting overall catalytic activity and selectivity. We have taken the approach of (a) manipulating nucleation and growth of NPs using oxide supports, surfactants, and inorganic complexes to create Pt NPs with uniform size, shape, and composition, (b) automating batch and continuous flow catalytic reaction tests, and (c) characterizing the molecular environments of Pt surfaces using *in situ* infrared (IR) spectroscopy and solid-state ^{195}Pt NMR. The following will highlight the synthesis and characterization of Ag-doped Pt NPs and their influence on C_2H_2 hydrogenation selectivity, and the implementation of advanced solid-state ^{195}Pt NMR techniques to distinguish how distributions of molecular Pt environments vary with nanoparticle size, support, and surface composition.

TABLE OF CONTENTS

LIST OF FIGURES

Chapter 1:

Chapter 2:

Chapter 3:

Chapter 4:

Chapter 5:

Chapter 6:

Chapter 7:

LIST OF TABLES

Chapter 1

Heterogeneous Pt nanoparticle catalysts

1.1. Introduction

Heterogeneous Pt catalysts play a vital role in many large-scale chemical processes. In these materials, chemical reactions take place on surfaces that commonly consist of supported metal and metal oxide clusters or nanoparticles (NPs). Adsorption of reacting molecules onto catalytically active Pt NP surfaces increases the rate of reaction dramatically due to a lowering of activation energies. This attribute has enabled the development of modern-day agriculture and production of petrochemicals and fine chemicals on a global scale. However, while Pt-based catalytic processes are necessary for ~20% of all consumer goods, it is a precious metal with low natural abundance in the earth's crust.[1] Thus, it is of critical importance to understand how to utilize Pt catalysts more effectively by understanding molecular origins of their reactivity, so as to produce desired chemicals with minimal materials and by-products.

Understanding the functionality of heterogeneous Pt NP catalysts requires correlating their local electronic, chemical, and morphological structure to catalytic activity and selectivity. Catalytic reactions are mediated by unique active sites found at NP terraces, kinks, edges, steps, and metal-oxide interfaces. The active site, first proposed by H.S. Taylor, provides highly unsaturated or electronically distorted atoms that can strongly bind and dissociate adsorbates.[2] However, supported Pt NP catalysts contain distributions of molecular environments that are significantly affected by size, morphology, composition, and support, all of which can influence catalytic activity and selectivity (Figure 1.1). For example, Pt is a well-known

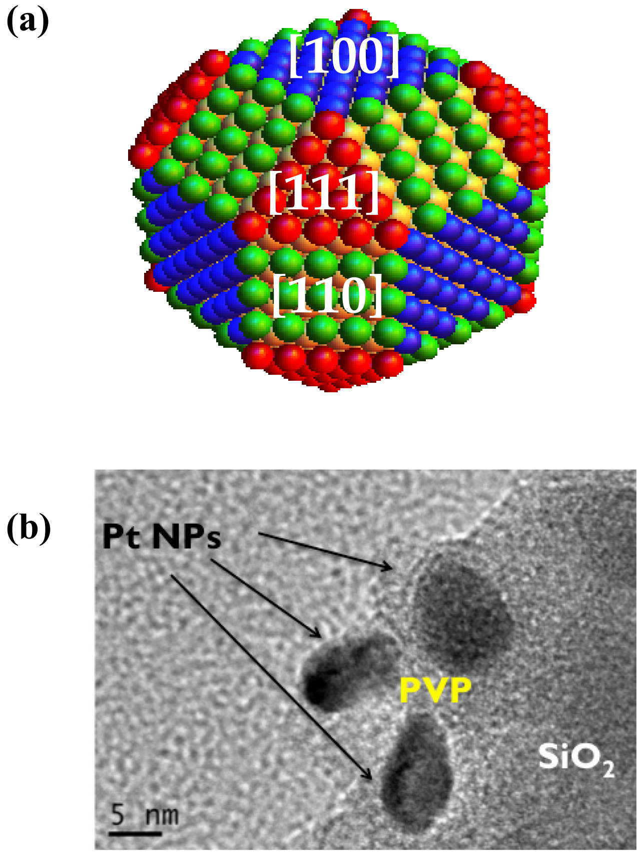

Figure 1.1 (a) Idealized representation of crystalline FCC NP showing a distribution of [100], [111], and [110] faces. (b) Transmission electron microscopy (TEM) image of Pt NPs supported on SiO_2 and capped with polyvinylpyrrolidone (PVP).

hydrogenation catalyst that becomes selective for cyclohexene dehydrogenation when NP size is below 8 nm.[3] With highly controlled Pt NP synthesis routes, model catalysts can be made with a high degree of uniformity. By establishing active site distributions in these materials and making correlations with measured reactivity, one can distinguish molecular signatures that are necessary for desired catalytic behavior.

1.2. Background and Motivation

Platinum is an ideal model catalyst displaying high activity for hydrogenation and oxidation reactions, temperature stability, and corrosion resistance. These properties make it one of the most widely used and studied catalysts for gas and liquid-phase reactions.[4] For example, UHV studies on single crystals of Pt (e.g., electron diffraction, temperature programmed desorption, scanning tunneling microscopy, and vibrational spectroscopy) have identified several adsorbate structures and their reactivity on different sites (e.g., [111], [110], [100], other high index planes, as depicted in Figure 1.2).[5] While these studies have proven useful in providing information about the activity of active sites, single crystals and UHV environments are not representative of supported Pt NP catalysts during at conditions. On the contrary, supported NP catalysts have broad distributions of surface sites and environments that can dynamically rearrange during the higher pressure conditions of practical catalytic applications. The situation becomes even more complex with a Pt NP alloy, where bulk and surface compositions are distinct and can vary with reaction conditions. A significant gap of information exists, which specifically relates to how distributions of supported Pt and Pt-alloy NP environments coordinate or compete to mediate adsorption, diffusion, and reaction.

Filling this gap of knowledge necessarily requires the ability to produce uniform Pt and Pt-alloy NP environments that can be reproducibly interrogated using surface-specific *in situ* characterization techniques. Refined solution-phase synthesis methods have demonstrated the ability to produce Pt NPs with uniform size,

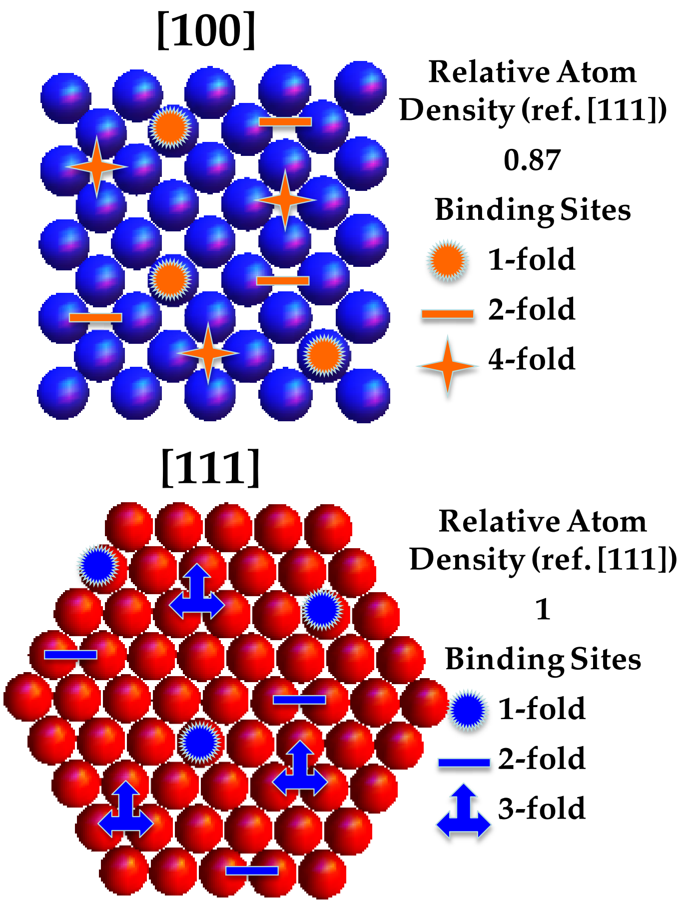

Figure 1.2. [111] and [100] single crystal planes showing relative surface atom density and potential binding site configurations of adsorbates.

morphology, and composition.[6] Some of these synthesis methods can produce Pt NPs with a predominance of specific sites that affect catalytic behavior. For example, shaped-directed Pt NPs (cubes, cuboctahedron, octahedron), which have distinct distributions of [111] and [100] surfaces, show marked differences in selectivity for benzene hydrogenation.[7] These synthesis methods are applied here to develop model Pt NP catalysts that can be characterized to establish molecular signatures of unique active site distributions.

Surface-specific *in situ* characterization techniques, such as infrared (IR) and solid-state ^{195}Pt nuclear magnetic resonance (NMR) spectroscopy, provide molecular details regarding the structure of adsorbates on surfaces and distributions of Pt environments in supported catalysts. IR spectroscopy probes molecular vibrational modes (stretching and bending) and detects adsorbate structure and Pt atom coordination with high sensitivity. ^{195}Pt NMR can distinguish differences in local electronic structure by probing ^{195}Pt spins in bulk and surface environments. A variety of *ex situ* bulk and surface-specific interrogation methods (e.g., X-ray diffraction, X-ray photoelectron spectroscopy, transmission electron microscopy) can be used to complete the molecular description of supported Pt NPs. These complementary techniques are applied here to establish correlations between Pt and Pt-alloy NP molecular surface distributions and resultant catalytic activity and selectivity.

The focus of this thesis is to establish relationships between Pt NP surface environments and catalytic activity and selectivity through: (1) manipulation of nucleation and growth from molecular precursors to create specified active site distributions, (2) measurements of activity and selectivity using automated catalytic testing, and (3) elucidation of catalytically active sites and mechanisms using IR and ^{195}Pt NMR spectroscopy methods. The following chapters highlight my work in each of these areas and demonstrate experimental concepts that can be further developed here at UCSB. Briefly, chapters 2-3 focus on the synthesis, characterization, catalytic testing, and *in situ* IR spectroscopy of Ag-doped Pt nanoparticle catalysts, where thermodynamic phase segregation causes Ag to remain at the surface of Pt nanoparticles. This thermodynamic driving force resulted in stable Ag surface compositions up to 300 ^{o}C. With ~0.5 ML of Ag coverage, the catalyst was able to achieve higher activity and selectivity for C_2H_4 during C_2H_2 hydrogenation compared to Pt-only, Pd-only, and the industrially employed PdAg supported catalysts. Chapters 4-7 focus on the implementation and development of novel solid-state ^{195}Pt NMR methods to establish distributions of Pt environments in bulk, supported, and molecular catalysts. Using a new wideband excitation methodology, large ^{195}Pt spectral distributions were measured with greater resolution (~10X) and in far less time than previously possible (~10X). In combination with a homebuilt NMR probehead for cyrogenic applications, influences of oxidation, sulfidation, reduction, size, and support on ^{195}Pt distributions in bulk, supported, and molecular Pt catalysts were readily established.

1.3. In situ IR and solid-state ^{195}Pt NMR Spectroscopy

While many experimental techniques are useful in determining distributions of surface environments in supported Pt nanoparticle catalysts, the ability to conduct *in situ* adsorption measurements with IR and solid-state ^{195}Pt NMR provides an advantage that is necessary for elucidating molecular origins of unique catalytic reactivity. Moreover, their complementary molecular information provides subtle details regarding distributions of surface Pt atoms. As such, a brief description of the methodology for IR and solid-state ^{195}Pt NMR is given.

1.3.1. IR Spectroscopy

IR spectroscopy, which measures the absorption of vibrational energy by molecular bonds (in units of cm^{-1}), can identify and establish changes in molecular coordination when CO is adsorbed on Pt. CO vibrational energies are sensitive to Pt atom surface density (i.e., [111] vs. [100]), as well as linear, 2-fold, 3-fold, and 4-fold bonding configurations (Fig. 1.3).[8] Isotopically labeled ^{13}CO and experiments can provide definitive peak assignments by comparing observed frequencies to theoretical shifts calculated using the harmonic oscillator approximation. The high detection sensitivity of IR is ideal for *in situ* experiments to probe adsorbed states of gas phase molecules on the surface of supported Pt NPs. IR reflectance techniques, such as diffuse reflectance Fourier Transform infrared spectroscopy (DRIFTS), can be used to measure diffuse IR scattering from loose powders and thin films on solid surfaces. Furthermore, DRIFTS reactors can be automated (i.e., gas flow, temperature, and measurement control), which enables reproducible *in situ* tests to be carried out under a variety of conditions for long periods of time.

As an example, DRIFTS measurements (Fig. 1.4) of PVP-capped Pt NPs synthesized with 0, 1.1, 9.9, and 24.2 mol% Ag show changes in CO adsorption on specific Pt sites (e.g., step, terrace, [111] vs. [100]) that are being affected by

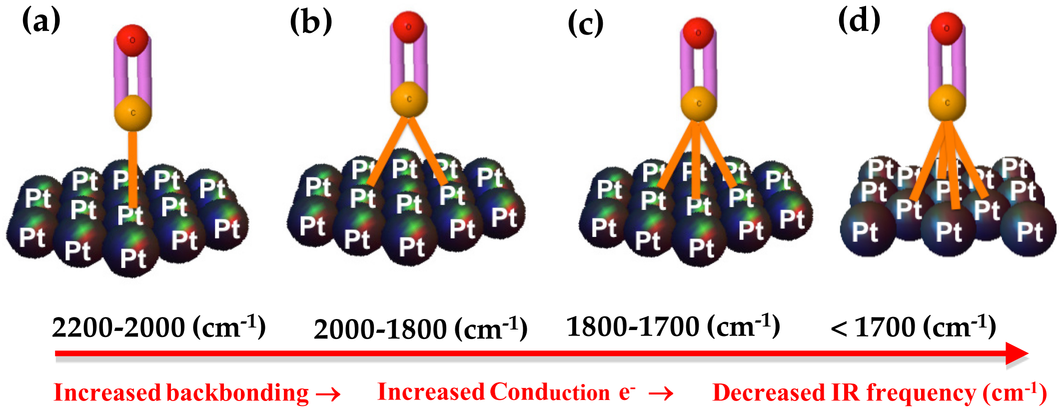

Figure 1.3. Illustrations showing possible bonding configurations of CO on FCC Pt: (a) linear, (b) 2-fold (bridge), (c) 3-fold, and (d) 4-fold. These interactions cause an increase of conduction electron backbonding from Pt surfaces to CO, which can be distinguished by characteristic IR frequencies.

adsorbed Ag and PVP moieties. IR spectra were recorded before and after exposure to 1% CO diluted in N_2 and evacuation to ~ 1 mTorr, confirming the appearance of CO on the surface of the Pt NPs. Pt NPs with 0 mol% Ag show two peaks at wavenumbers of 1982 cm^{-1} and 2043 cm^{-1}, which can be assigned to bridge-bonded and linear CO adsorbed on Pt,[9] respectively. The addition of 1.1% Ag results in a loss of bridge bonded CO at 1982 cm^{-1} and a small shift of the linear bonded species to 2045 cm^{-1}. Loss of intensity at 1982 cm^{-1} arises from Ag species that block bridge-bonded CO sites. Previous studies of CO on [100] single crystal surfaces agree well with peak positions of 2043 and 2045 cm^{-1} for 0 and 1.1 mol% Ag-doped Pt NPs, respectively, suggesting that cubes with [100] faces are present.[8] Increasing Ag content to 9.9 mol% results in two new distinct sites at 2022 cm^{-1} and 2085 cm^{-1},

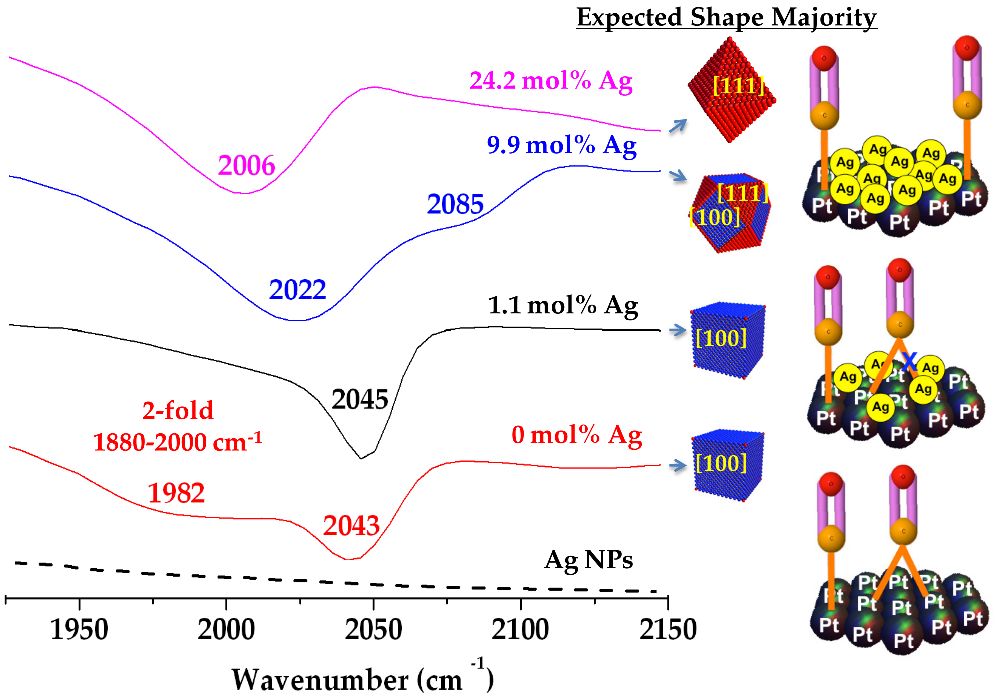

Figure 1.4. DRIFTS spectra of CO adsorbed on PVP-capped Pt NPs synthesized with (a) 24.2, (b) 9.9, (c) 1.1, and (d) 0 mol% $AgNO_3$. Peak positions indicate the presence of linear (2,200-2,000 cm^{-1}) and 2-fold (2,000-1,800 cm^{-1}) bonding sites that evolve with increasing Ag content. Idealized NP shape and adsorption of CO for each sample are illustrated on the right.

consistent with two linear CO species bonded to [111] and Ag-covered, stepped [100] surfaces of cuboctahedral Pt NPs. Increasing Ag content further to 24.2 mol% results in only a single species at 2006 cm^{-1}, consistent with the formation of octahedral Pt NPs with Ag-covered [111] surfaces. The shift to 2006 cm^{-1} for linear-bonded species implies that CO molecules are unable to dipole couple to one another, which would result in a shift to higher cm^{-1} (~ 2100 - 2200 cm^{-1}).[10] This

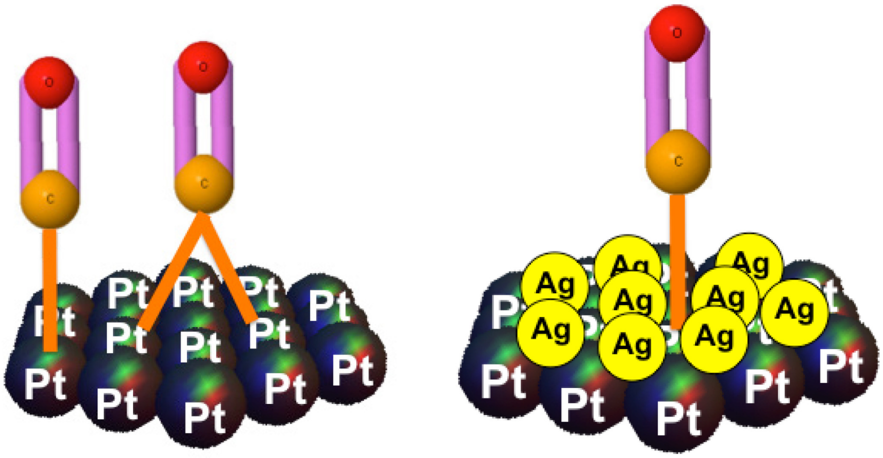

0 mol% Ag **24.2 mol% Ag**

Figure 1.5. Illustration of potential bonding configurations on PVP-capped Pt NPs with (a) 0 and (b) 24.2 mol% Ag. Ag atoms block Pt sites, permitting only linear and isolated bonding configuration for CO.

isolation of CO molecules on the surface of Pt NPs synthesized with 24.2 mol% $AgNO_3$ suggests Pt sites are blocked by Ag atoms on the Pt NP surface, as illustrated in Figure 1.5. A separate adsorption experiment on PVP-capped Ag NPs shows no detectable adsorbed CO, which provides further evidence that alloyed Ag atoms on the surface of the Pt NPs merely block sites and do not adsorb CO.

Peak identification of adsorbed CO species on 1.1 mol% Ag Pt NPs was made by observing the DRIFTS frequency shift of isotopically labeled ^{13}CO. Vibrational frequencies can be derived by solving Schrodinger's equation for the harmonic oscillator, which are proportional to the inverse square root of the reduced mass, $\mu^{-1/2}$. By performing isotopically labeled adsorption experiments, one can observe

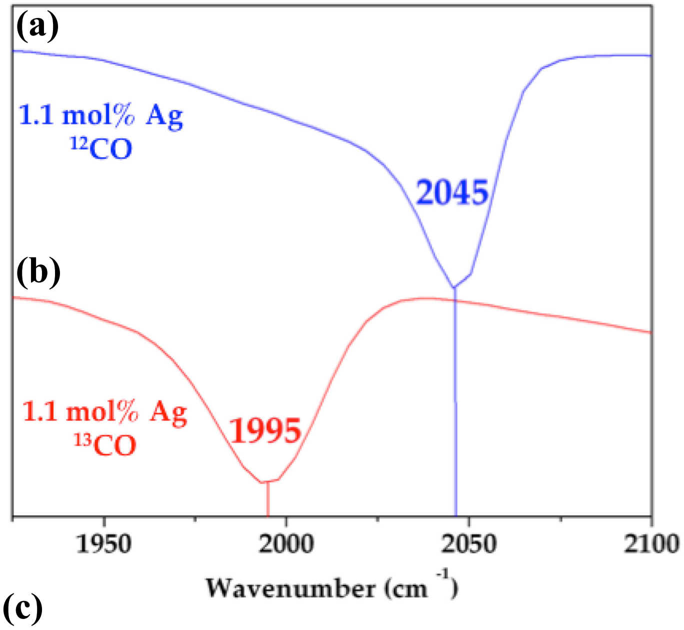

(c)

$$\left(\frac{v_{12CO}}{v_{13CO}}\right)_{Expt} \sim 1.025 \qquad \left(\frac{v_{12CO}}{v_{13CO}}\right)_{Theory} \sim 1.025$$

Figure 1.6. DRIFTS spectra of (a) ^{12}CO and (b) ^{13}CO adsorbed on PVP-capped Pt NPs synthesized with 1.1 mol% AgNO$_3$. (c) A comparison of experimental and theoretical (using the harmonic oscillator approximation) frequency ratios of ^{12}CO and ^{13}CO, confirms the peak identification of CO adsorbed on Pt NPs.

the calculated frequency shift using IR to validate peak assignments. Figure 1.6 shows DRIFTS spectra of CO and isotopically labeled ^{13}CO adsorbed on 1.1 mol% Ag-doped Pt NPs. The signal of ^{13}CO appears at 1995 cm^{-1}, resulting in a shift of ~50 cm^{-1}. The ratios between ^{12}CO and ^{13}CO frequencies, measured using IR and calculated using the change in reduced mass, are shown in Figure 1.6c, confirming the expected shift of ^{13}CO within the resolution of the spectrometer. Using *in situ* DRIFTS and isotopically labeled compounds, the evolution of site distributions on Pt NPs can be monitored, quantified, and correlated to catalytic activity and selectivity.

1.3.2. Solid-state ^{195}Pt NMR Spectroscopy

Solid-state NMR can detect subtle energy differences between spin angular momentum states of nuclei under an applied magnetic field. Valence and conduction electrons shield nuclei from the applied magnetic field, causing a "chemical" shift in the frequency (measured in ppm) necessary to excite these spin states. These shifts, and the subsequent relaxation of excited spin-states, provide information about the molecular environments of nuclei. In non-metallic spin-1/2 compounds, such as ^{1}H and ^{13}C, valence electrons are the primary contributor to magnetic shielding, and chemical shift ranges are typically ~20 ppm and ~200 ppm (Fig. 1.7). In metalllic spin-1/2 compounds, such as ^{195}Pt, the sea of conduction electrons is the primary source of magnetic shielding, which results in large (Knight[11]) shifts of ~50,000 ppm.

The Knight shift can be used to study changes in conduction electron densities of bulk and surface Pt atoms in NPs with decreasing size. The origin of Knight shifts arises from Fermi contact interactions between polarized conduction electron spins and ^{195}Pt nuclei in an applied magnetic field, as illustrated in Figure 1.8. The strength of Fermi contact interactions depends on the conduction electron spin density, which varies with radial distance from the center of a NP.[12] Slichter *et al.* has demonstrated

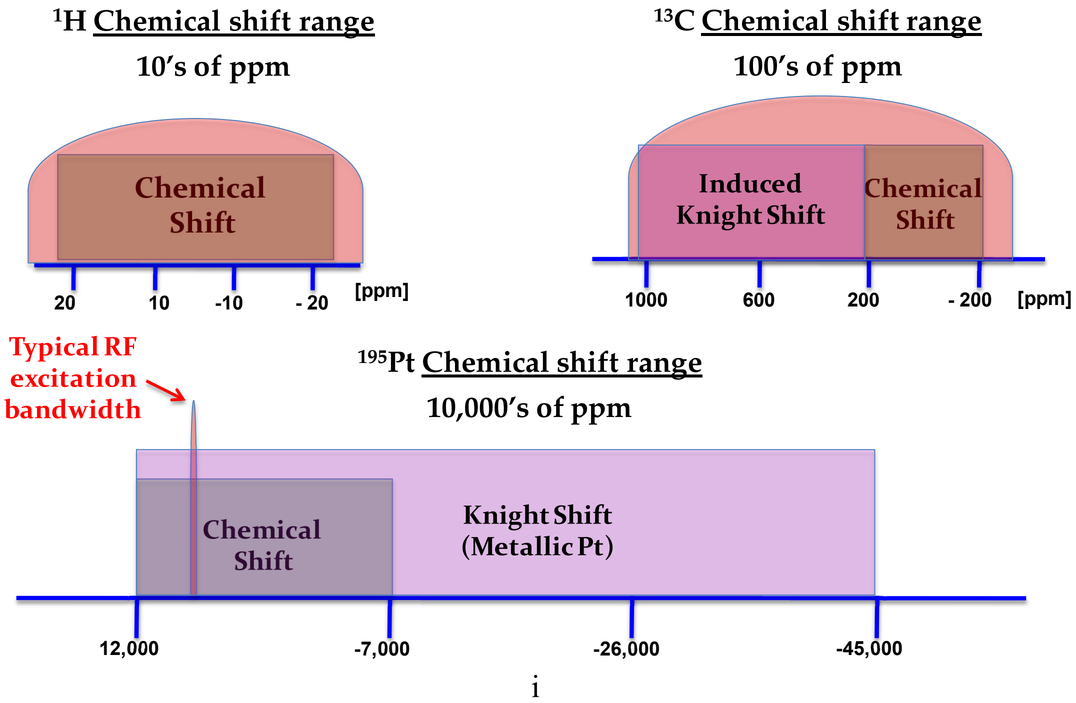

Figure 1.7. Illustration showing the chemical and Knight shift ppm ranges for ^{1}H, ^{13}C, and ^{195}Pt nuclei. Excitation bandwidths achievable using conventional constant-frequency RF pulse techniques are overlaid in shaded red.

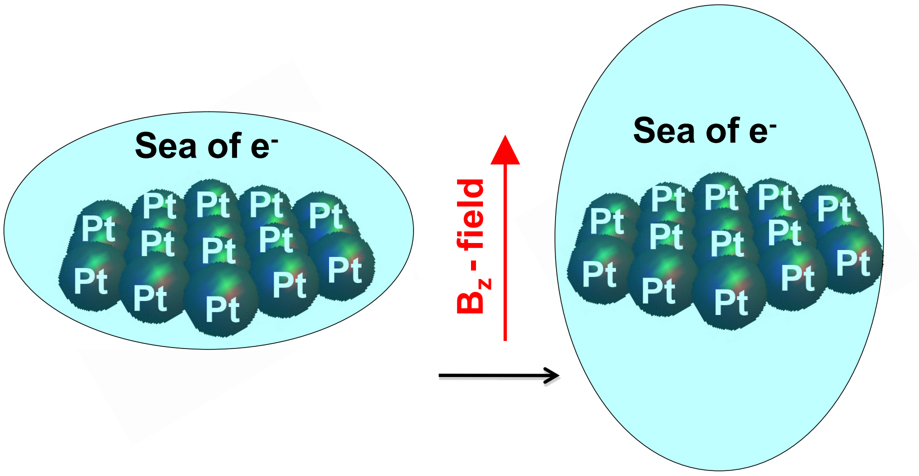

Figure 1.8. Illustration showing the polarization Pt of conduction electrons in an applied magnetic field that cause ^{195}Pt Knight shifts of 10,000's of ppm.

that smaller Pt NPs (< 5nm) have a much broader metallic line-shape that extends over the entire chemical and Knight shift range of ~50,000 ppm; with sufficiently small sizes (< 1 nm), the line-shape becomes narrow and is located within the typical range of ^{195}Pt chemical shifts (7,000 to -7,000 ppm).[13] These observations suggest that surface Pt atoms are not Knight shifted or that smaller-sized NPs no longer have sufficient conduction electron contributions to create strong Fermi interactions with ^{195}Pt nuclei. In theory, ^{195}Pt NMR can be used to establish distributions of bulk and surface Pt environments, which can then be correlated to size, morphology, composition, and catalytic reactivity of supported Pt NPs.

As an example, solid-state ^{195}Pt NMR spectra of bulk compounds (Fig. 1.9) are compared to provide an initial understanding of the effects of Knight shifts and the breadth of the entire ppm range expected for supported Pt NPs. ^{195}Pt NMR spectra of α-PtO_2, H_2PtCl_6, and Pt^0 span a chemical shift range of ~50,000 ppm. H_2PtCl_6 (0 ppm) and α-PtO_2 (3,300 ppm) resonances are located in the typical range of ^{195}Pt compounds (7000 to -7,000 ppm). Pt^0, acquired under static conditions at 140 K, is Knight shifted to -38,900 ppm. This extremely large Knight shift range can provide high-resolution detail about electronic properties within reduced Pt NPs, but exciting such a large spectral range is difficult in practice due to the limited excitation bandwidths of conventional methods. Moreover, conduction electron effects require measurements to be conducted at low temperatures. Such characteristics of ^{195}Pt NMR spectra present experimental challenges when applying standard NMR

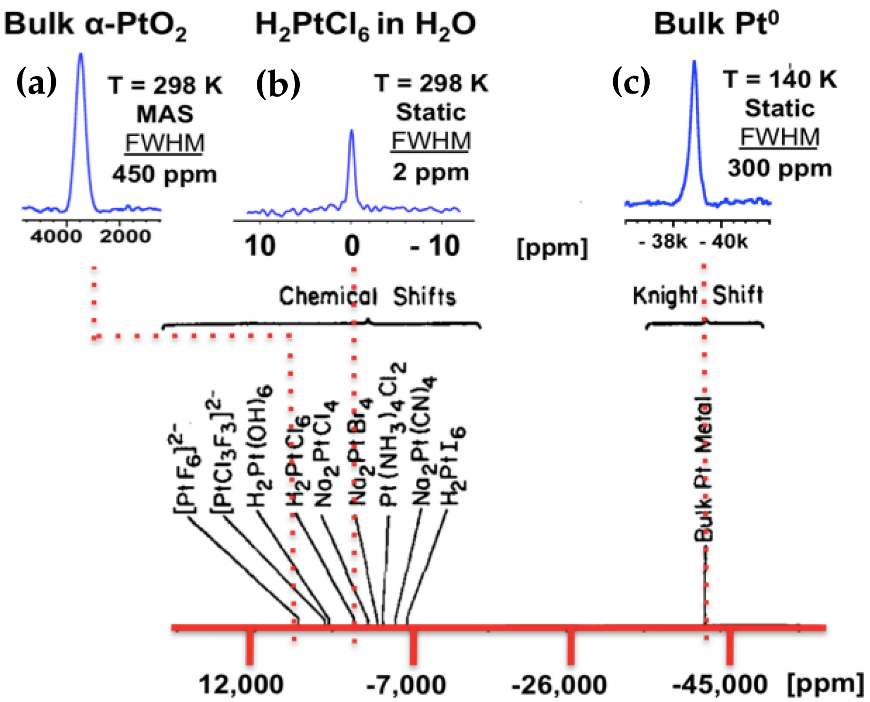

Figure 1.9. Measured (above) solid-state ^{196}Pt NMR spectra (300 MHz, 7.05 T) for (a) α-PtO_2 (b) H_2PtCl_6 dissolved in H_2O, and (c) Pt^0 powder, as compared to previously measured (below) compounds, adapted from reference.[13] The temperature, MAS/static conditions, and full width at half maximum (FWHM) of each acquired signal are listed next to each spectrum.

techniques, but can be circumvented by implementing more advanced broadband NMR radiofrequency irradiation methods at cryogenic temperatures. With this advanced methodology, molecular influences of surface composition, size, and support interactions on bulk and surface ^{195}Pt environments can be distinguished.

1.4. References

(1) a. Matthey, Johnson. "Price Charts." *Platinum Today* **2009**. b. Matthey, Johnson. "Production-Resources in South Africa." *Platinum Today* **2002**. c. Matthey, Johnson. "Platinum Group Metals Price Bulletin." *Platinum Today* **2012**.

(2) Taylor, H. *Proceedings of the Royal Society of London. Series A* **1925,** *107*, 4.

(3) Somorjai, G. A.; Park, J. *Angewandte Chemie International Edition* **2008**, *47*, 9212.

(4) Park, S.; Xie, Y.; Weaver, M. *Langmuir* **2002**, *18*, 5792.

(5) Zaera, F.; Somorjai, G. A. *Langmuir* **1986**, *2*, 686.

(6) Chen, J.; Lim, B.; Lee, E.; Xia, Y. *Nano Today* **2009**, *11*, 81.

(7) Somorjai, G. A.; Park, J. *Topics in Catalysis* **2008**, *49*, 126.

(8) Chang, S.; Leung, L.; Weaver, M. *J. Phys. Chem*. **1989**, *93*, 5341.

(9) J. W. Niemantsverdriet, *Spectroscopy in Catalysis: An Introduction,* Wiley VCH, **2007**.

(10) Fox, S.; Browne, V.; Hollins, P. *JESRP* **1990**, *54/55*, 749.

(11) Townes, C.; Herring, C.; Knight, W. *Physical Review* **1950**, *77*, 852.

(12) Slichter, C. P. *Phil. Mag. B* **1999**, 79, 1253.

(13) Rhodes, H.; Wang, P.; Stokes, H.; Slichter, C.; Sinfelt, J. *Phys. Rev. B* **1982**, *26*, 3559.

Chapter 2

Partial Hydrogenation of C_2H_2 on Ag-Doped Pt Nanoparticles

Adapted from the Journal of Physical Chemistry C:

Louis C. Jones, Zachary Buras, and Michael J. Gordon, *J. Phys. Chem. C.* 116, 12982-12988 (**2012**).

Department of Chemical Engineering, University of California, Santa Barbara, Santa Barbara, California 93106-5080, USA

Abstract

Pt nanoparticles (NPs) with submonolayer Ag coverage were synthesized and catalytically tested to investigate the effects of surface Ag and NP shape on C_2H_2 hydrogenation activity and selectivity. Various NP shapes (cubes, cuboctahedra, and octahedra) in the 6−8 nm range were synthesized using colloidal methods with PVP (polyvinylpyrrolidone) as a capping ligand and Ag^+ for structure direction. Solid-state ^{13}C NMR of PVP−NP interactions, as well as electrochemical measurements of oxygen evolution reaction (OER) activity, revealed that submonolayer levels of Ag significantly modify both the physical and electronic structure of the Pt NP surface. Octahedral NP catalysts with 0.5 monolayers of Ag were found to be highly selective for C_2H_2-to-C_2H_4 hydrogenation (C_2H_4/C_2H_6 >8) at reaction rates comparable to total hydrogenation on pure Pt. Traditionally prepared PtAg catalysts synthesized via incipient wetness showed analogously high selectivities but lower site time yields compared to NPs. In contrast, total hydrogenation was observed for Pt, Pd, and PdAg catalysts under the H_2-rich reaction conditions used. Surface Ag, rather than nanoparticle shape or faceting, was found to be responsible for high selectivity in the PtAg case. This work demonstrates that bimetallic systems with inherent phase segregation (e.g., PtAg) offer a unique route toward thermally stable surface compositions that can promote high activity and selectivity over a large operating window.

2.1. Introduction

Many heterogeneous catalysts owe their functionality to the unique chemistry that occurs near defects or unsaturated atoms on the surface of metal (oxide) nanoparticles dispersed on a solid support. In particular, it is well-known that reactivities on nanoparticle (NP) surfaces differ significantly from their bulk counterparts. This behavior is due to a combination of finite size effects (i.e., unsaturated atoms at edges, kinks, and corners),[1] preferred morphologies or faceting which favor specific coordinations,[2,3] metal−support interactions,[4−6] or modification of the electronic structure of the NP surface due to alloying.[7] In the latter case, judicious addition of “dopant” atoms to the NP interior or surface can result in higher turnover,[8] improved selectivity,[9] multiple functions,[10] or enhanced resistance to deactivation.[11] For example, alkalimetal- promoted PdAg catalysts are used industrially at low temperature (30−100 °C) to remove alkyne contaminants from alkene streams;[12−16] the current hypothesis is that surfaces enriched with Ag minimize β-hydride formation in/on Pd and decrease the heat of adsorption of alkene relative to alkyne.[14] In addition, small levels of CO are often added to Pd only systems to promote partial hydrogenation;[15] however, CO level fluctuations can result in thermal runaway due to CO reduction.[16] Furthermore, surface composition and structure of alloy NP catalysts can also evolve during reaction as the temperature[17] or surrounding atmosphere changes.[18] These constraints not only impose limitations on accessible reactivity but also make it difficult to characterize and establish how NP morphology and surface chemistry influence catalytic reactivity.[19]

The tendency of particular bimetallic systems to phase segregate provides an opportunity to maintain more stable surface compositions over a larger range of catalyst operating conditions. For example, in contrast to PdAg, the PtAg system is immiscible in the bulk below 600 °C.[20] STM measurements of Ag deposited on Pt(111) at $T > 350$ °C have shown that Ag incorporation is limited to a single monolayer (i.e., a mixed Pt−Ag outer layer), after which further deposition results in Ag island formation.[21] Moreover, cluster calculations predict surface enrichment of Ag on PtAg nanoparticles at $T < 400$ °C.[22,23] The Somorjai group has also shown that Pt NPs synthesized with Ag have significantly lower turnover numbers for C_2H_4 hydrogenation compared to the Pt-only case;[24,25] they hypothesized that Ag is at the surface and/or diminishes electron density in the Pt 5d due to charge transfer to Ag. These results hint that surface enrichment of a particular chemical species, aided by a system's natural tendency to phase segregate, may be a straightforward route to modify the electronic structure of a NP surface, with the goal of achieving an active and selective catalyst that is stable over a wide range of conditions.

In this work, we demonstrate that submonolayer Ag "doping" of Pt nanoparticle surfaces can be used to create an active, selective, and stable catalyst for C_2H_2-to-C_2H_4 hydrogenation. Nanoparticle catalysts composed of a majority of Pt cubes, cuboctahedra, or octahedra in the 6−8 nm range, with different quantities of surface Ag, were formed using a colloidal synthesis technique with Ag^+ and PVP as structure-directing and capping agents, respectively. Solid-state ^{13}C NMR analysis of PVP−nanoparticle interactions and cyclic voltammetry showed that Ag significantly changes molecular interactions and H_2/O_2 evolution reactivity on Pt nanoparticle surfaces. Catalytic testing of supported Pt_xAg_y NPs on SiO_2 in a recirculating batch reactor revealed that ~0.5 ML of Ag on a Pt NP surface results in a highly selective and active catalyst for C_2H_2-to-C_2H_4 hydrogenation between 180 and 220 °C. Traditionally prepared PtAg catalysts synthesized via incipient wetness showed analogously high selectivities but lower site time yields compared to NPs; in contrast, unpromoted Pd and PdAg catalysts were not selective, even at low temperatures (30−50°C), under identical reaction conditions.

2.2. Experimental Section

2.2.1. Synthesis and Characterization of Pt, PdAg, and PtAg Catalysts

Ag-doped Pt NPs with different shapes were synthesized using PVP (MW = 29 K) as a capping ligand and $AgNO_3$ for structure direction, as mentioned elsewhere.[26] Briefly, the synthesis involved dropwise addition of H_2PtCl_6 and PVP solutions to refluxing ethylene glycol with varying amounts of $AgNO_3$ (1, 10, and 24 mol % Ag based on total Pt + Ag for cubes, cuboctahedra, and octahedra, respectively). After a 30 min reflux, the reaction was quenched and NPs were isolated and washed (3−5 cycles of centrifugation, decanting, and redissolution in ethanol to wash away excess PVP and soluble byproduct). All chemicals (Sigma-Aldrich) were used as received, and solutions were made using dry solvents. Supported catalysts were prepared by mixing PVP-capped Pt_xAg_y NPs (1−2 wt % Pt basis) with colloidal SiO_2 (~50 nm, Nissan Chemical) in isopropanol, followed by vacuum drying overnight and grinding to −325 mesh. Ground catalysts were calcined at 300 °C in 20 min cycles of O_2 and H_2 to remove PVP, which was confirmed by thermogravimetic analysis (TGA). Ag-only NP catalysts were synthesized in a similar fashion with PVP + $AgNO_3$, while "Ag-free" Pt NP catalysts were realized by etching supported Pt_xAg_y samples in 8 M HNO_3 at 60 °C for 30 min.[24]

Traditional silica-supported Pt, PdAg, and PtAg catalysts, without alkali metal promoters were made via incipient wetness using $Pd(NO_3)_2 \cdot 2H_2O$, $H_2Pt(OH)_6$, and $AgNO_3$ precursors with 2 wt % metal loading. Catalysts were dried overnight in vacuum at 120 °C, followed by successive calcination in O_2 (4 h, 20 sccm), Ar (1 h, 20 sccm), and H_2 (2 h, 20 sccm) at 500 °C. A 5 wt % Pd on SiO_2 commercial catalyst from BASF (Escat 1315) was also tested for comparison. Catalyst morphology (e.g., crystallinity, size, and sintering) and Ag content were monitored using transmission electron microscopy (TEM), X-ray diffraction (XRD), inductively coupled plasma elemental analysis (ICP), and X-ray photoelectron spectroscopy (XPS).

2.2.2. NMR of Surfactant−Nanoparticle Interactions

Solid-state $^{13}C\{^1H\}$ CP-MAS NMR (cross-polarization of ^1H to ^{13}C, magic angle spinning) of PVP bound to the surface of Pt_xAg_y NPs was used to probe surface composition directly after synthesis. Measurements were performed on a 300 MHz Bruker NMR system with ~300 mg of sample, spinning rates of 2−5 kHz, and a contact time of 1 ms.

2.2.3. Electrochemistry

Cyclic voltammetry (CV) was conducted in deoxygenated, 0.1 M $HClO_4$ with Luggin capillaries, Pt mesh counter electrode, and a saturated calomel reference electrode (SCE). NP solutions were drop-cast onto FTO (fluorinated tin oxide) working electrodes and vacuum-dried overnight at 100 °C. Samples were measured before and after low voltage (−0.35 to 0.65 V SCE, 500 CV scans at 500 mV/s) and high voltage (−0.35 to 1.5 V SCE, 500 CV scans at 500 mV/s) electrochemical cleaning cycles. SCE potentials were corrected to the standard hydrogen electrode (SHE) by adding 241 mV.27

2.2.4. Gas-Phase Hydrogenation Testing

Supported NPs or traditional catalysts (~1−10 mg) were mixed with calcined colloidal silica (40−50 mg, −325 mesh) and loaded into a quartz tubular reactor (6 mm × 150 mm) with 15 mg of silica packing before and after the active catalyst layer. The reactor was connected to a 500 cc mixing vessel with a stainless steel bellows pump (~80 cc/min) for recirculation. The reacting gas volume was autosampled (~750 μL) at regular intervals (5 min), and product distributions were analyzed using gas chromatography. The NP surface was prepared prior to reaction with 10 sccm H_2 at the reaction temperature of interest for 20 min, followed by 10 sccm He for 10 min, and subsequent evacuation and isolation from the mixing vessel; after charging the mixing vessel to 760 Torr with a C_2H_2:H_2:He mixture (2:8:70 mol ratio), the reaction was initiated by circulating the gas through the preheated reactor. 100% excess H_2 (C_2H_6 basis) was used to purposefully push the reaction toward the fully hydrogenated product (C_2H_6) to test the inherent chemical selectivity of the catalyst to produce C_2H_4.

2.3. Results

2.3.1 Catalyst Morphology

TEM images of as-made Pt cubes (~1 mol % $AgNO_3$) and octahedra (~24 mol % $AgNO_3$) are shown in Figure 2.1; particles were highly crystalline with sizes inthe 6−8 nm range. Given that surfactant-stabilized NPs must be “cleaned” before catalytic testing, post-synthesis thermal treatment was required to burn away PVP. However, calcination can induce agglomeration,[28] phase separation,[29] or changes in morphology[30] that can influence particle reactivity. As such, catalyst morphology and Ag content were monitoredafter various treatment steps using TEM, XRD, ICP, and XPS. TEM imaging of the supported octahedra NP catalyst (Figure 2.1c) after 300 °C heat treatment for 2 h under reaction conditions shows that particles do not sinter; particle size distributions after calcination were ~9 ± 2 nm (1σ), with particles becoming more spherical at higher reaction temperatures. Diffraction analysis (see Figure 2.2) demonstrates that NP size and crystallinity do not change after 300 °C

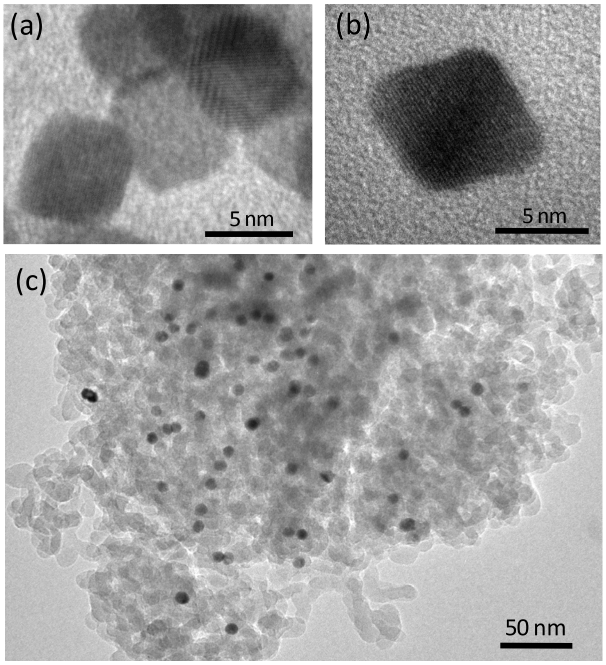

Figure 2.1. TEM images of as-made, Ag-doped Pt NPs: **(a)** cubes, synthesized with 1 mol% Ag and **(b)** octahedra, synthesized with 24 mol% Ag. **(c)** Supported PtAg octahedra catalyst after calcination and 2 hr at 300 °C in reaction gas; particle sintering was not observed.

redox cycling to remove PVP or after 8 M HNO_3 etching; no signs of NP agglomeration (Scherrer analysis gave 7−8 nm), lattice constant variation, or formation of bulk Ag domains were seen.

Bulk and surface compositions of Pt_xAg_y NPs were quantified and estimated before and after HNO_3 etching using XPS and ICP analysis. This data, along with composition and particle sizes for the traditional catalysts, are given in Table 1. XPS analysis of NP catalysts showed an increase in Ag 3d signals from cubes, to

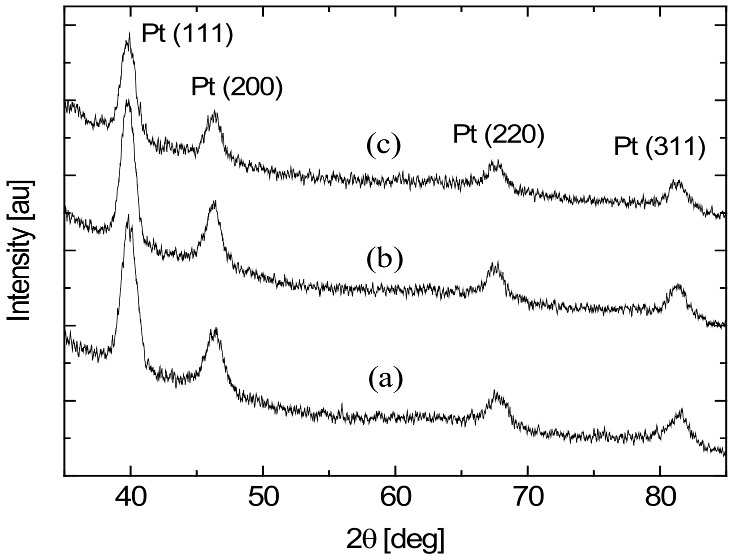

Figure 2.2. XRD patterns of supported octahedra ($Pt_{91}Ag_9$ stoichiometry) in the **(a)** as-made case, **(b)** after redox cycling (O_2/H_2) at 300 °C, and **(c)** after 8M HNO_3 treatment at 60 °C.

cuboctahedra, to octahedra as more $AgNO_3$ was incorporated. Composition estimates from XPS were lower than that used in the synthesis mixture (9 vs. 10 and 14 vs. 24 mol % Ag) due to removal of the AgCl byproduct during particle washing/centrifugation and redispersion; Ag was below the XPS detection limit for the as-made 1.1 mol % $AgNO_3$ case. ICP quantifications prior to etching were also consistently lower than compositions estimated from XPS. We note that XPS probesthe entire particle volume (i.e., the photoelectron mean free path is ~2 nm); notwithstanding, ICP and XPS quantification differences may be attributed to Ag surface enrichment. Ag coverage, assuming all the Ag went to the particle surface, was estimated from ICP results and XRD/TEM particle sizes for each catalyst using

Pt- and Pd-atom surface areas of 0.084 and 0.076 nm^2[31] respectively. After HNO_3 etching, Ag content in NPs decreased, but Pt loading remained constant (along with particle size from XRD). These results suggest that Ag is on the Pt NP surface; however, more direct measures (NMR and electrochemistry) of surface Ag and its effects are summarized in sections II and III.

2.3.2 Surfactant-nanoparticle interactions

Prior to PVP removal for catalytic testing, solid-state ^{13}C NMR was conducted to assess surface enrichment of Ag by monitoring changes in molecular interactions of PVP with nanoparticle surfaces. As shown in Fig. 2.3, the NMR spectrum of bulk PVP (#1) is very similar to PVP bound to Pt-only NPs (#2). However, after 1 mol% $AgNO_3$ is added (cubes, #3), new ^{13}C resonances appear at 20, 46, and 63 ppm (shading). Further incorporation of Ag (9 mol%, octahedra, #4) produces an NMR spectrum that is nearly identical to PVP bound to Ag-only NPs, which were synthesized without Pt (#5). Thus, PVP interactions with Pt appear to be molecularly distinct from those with Ag, which may also play a role in stabilization of Ag on the surface of Pt during synthesis. These qualitative observations are consistent with enrichment of Ag on the Pt NP surface.

Further inspection of resonances that disappear as more Ag is added provides insight into possible intermediates that play a role in directing Pt_xAg_y NP shape. The simultaneous disappearance of PVP resonances (29, 40, and 174 ppm) and appearance of hydro-carbon and amine resonances (20 and 46/63 ppm, respectively)

Table 2.1. Elemental and particle size analysis of supported catalysts

Shape or Stoich.(1)	Synthesis Mix	Pre-etch		Surface Coverage(3)	Post-etch ICP	Pt or Pd Loading(4)	Particle Size(5)
		XPS(2)	ICP				
	[mol% Ag]	[mol% Ag]		[ML]	[mol% Ag]	[wt.%]	[nm]
Nanoparticle Catalysts							
M	0	n/a	n/a	n/a	n/a	1.0	7-8
C	1.1	ND(6)	1	0.06	<0.03	1.9	7-8
CO	9.9	9	7	0.47	2	1.8	7-8
O	24.3	14	9	0.51	3	2.0	7-8
Traditional Catalysts							
Pd BASF	n/a	n/a	n/a	0	n/a	5.0	8
Pt	0	↓	↓	0	↓	2.0	24-25
$Pt_{87}Ag_{13}$	13			>1		1.9	28
$Pd_{77}Ag_{23}$	23			>1		1.8	3

---

[1] Nanoparticle shape (M = no Ag, C = cubes, CO = cuboctahedra, and O = octahedra) or stoichiometry of the traditionally-prepared catalyst.

[2] XPS quantification based the Ag 3d and Pt 4f peak areas.

[3] Ag coverage (monolayers - ML) based on TEM particle size, shape, and ICP data if all the Ag went to the particle surface.

[4] Pt or Pd loading of the supported catalyst.

[5] Particle size from Scherrer analysis of XRD data.

[6] Not detected.

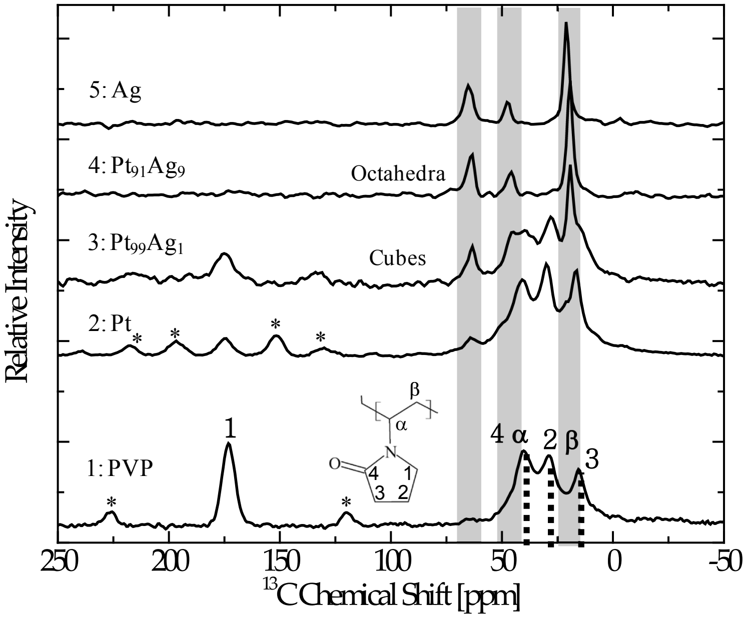

Figure 2.3. Solid-state $^{13}C\{^{1}H\}$ NMR of bulk PVP **(#1)** and PVP bound to the surfaces of different nanoparticles: **(#2)** Pt-only, **(#3)** Pt cubes ($Pt_{99}Ag_{1}$), **(#4)** Pt octahedra ($Pt_{91}Ag_{9}$), and **(#5)** Ag-only. Note: * denotes spinning side-bands of C=O groups within PVP and MAS rates ranged from 2-5 kHz.

suggest that Ag addition promotes $4,\alpha$ and $2,\beta$ bond cleavage to form hydrocarbon and amine fragments.[32] Since ^{13}C signals of PVP bound to Ag-covered surfaces showed no signs of characteristic C=O functional groups (174 ppm), it is possible that pyrrolidone units have decomposed to form X-C=O groups, which would not be detected because H-atoms are no longer in nanometer proximity to C-atoms (i.e., cross-polarization cannot occur). This molecular evidence shows that Ag addition to Pt NPs may promote the formation of new ligands (i.e., from PVP decom-position during synthesis) that bias surface growth rates, and thus, the formation of specific particle shapes (e.g., cubes vs. octahedra).

2.3.3 Electrocatalysis

The presence of Ag on Pt NP surfaces and Ag's influence on Pt reactivity was evaluated electrochemically using cyclic voltammetry (CV) to probe Pt redox behavior and overpotentials required for oxygen evolution (OER), hydrogen evolution (HER), and hydrogen oxidation (HOR). $HClO_4$ electrolyte was chosen to minimize anion-specific interactions (i.e., the bi-sulfate effect[33-35]) that can bias H-adsorption and HER/HOR activities measured in H_2SO_4. In addition, it has been previously shown that surfactant contamination of Pt single crystals[36,37] and NP surfaces[38-40] obscures electrochemical results if exhaustive measures are not used to properly clean catalyst surfaces. As such, NP samples were electrochemically cleaned through extensive voltage cycling (see experimental section) to assess the influence of PVP surfactant and Ag on electrochemical activity.

CV curves for the unetched Pt cubes (0.06 ML Ag) and octahedra (0.51 ML Ag) before and after the 500 cycle cleaning step are shown in Figure 2.4. Several observations should be noted: (1) octahedra have little OER activity (~1.7V SHE) before cycling, (2) cubes have significant OER activity before and after cycling, (3) OER and Pt oxide reduction on the cathodic scan (~0.6 V SHE) increase >10X after cycling for octahedra, and (4) HER/HOR activity (~0V SHE) for both particles is similar before and after cycling. In contrast, HNO_3-etched particles (Fig. 2.5), which

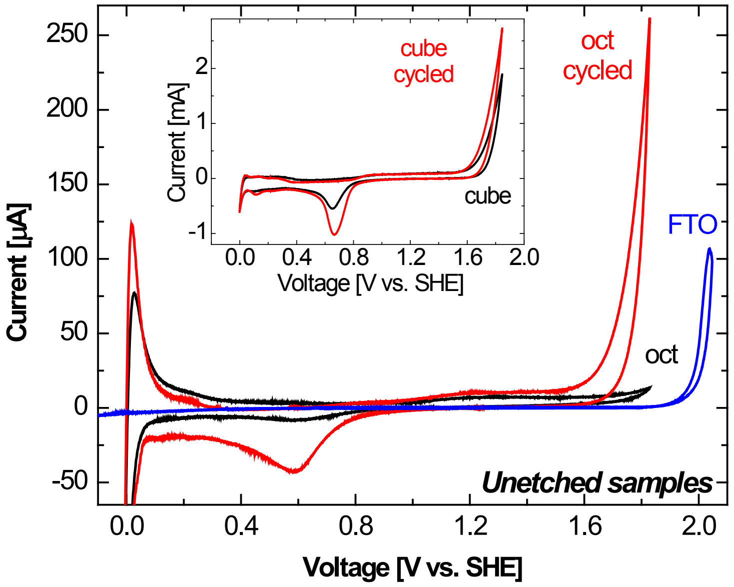

Figure 2.4. Tenth CV scan of unetched PtAg octahedra (0.51 ML Ag) and Pt cubes (0.06 ML Ag, inset) on FTO in 0.1M $HClO_4$. CV scans were recorded at 50 mV/s before (black traces "oct" and "cube") and after (red traces "oct cycled" and "cube cycled") a 500 cycle cleaning procedure. A clean FTO substrate (blue trace "FTO") is shown for comparison.

have substantially less (or no) surface Ag (see Table 1), have similar CV curves before and after cycling.

These trends can be rationalized in the following manner: voltage cycling and/or direct acid etching in HNO_3 removes surface Ag and exposes more Pt, as evidenced by the increase in the Pt oxide reduction peak and OER onset at potentials nearer to clean Pt. Voltage cycling (500x) to 0.65V SCE (~0.9V SHE) should quickly remove sub-monolayer levels of Ag because $Ag \rightarrow Ag^+$ occurs at low pH for potentials

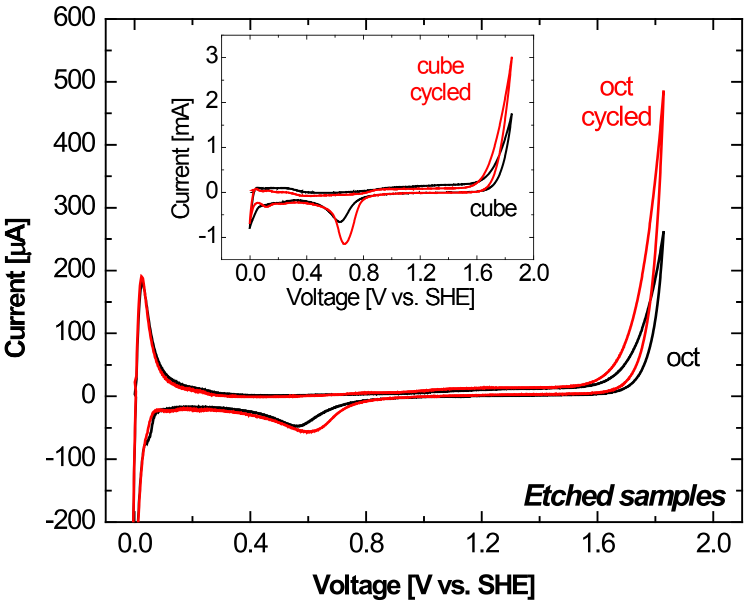

Figure 2.5. Tenth CV scan of 8M HNO_3 etched PtAg octahedra and Pt cubes on FTO in 0.1M $HClO_4$ (c.f. Fig. 2.4). CV scans were recorded at 50 mV/s before (black traces "oct" and "cube") and after (red traces "oct cycled" and "cube cycled") a 500 cycle cleaning procedure.

above 0.8V SHE (e.g., see Pourbaix diagrams[41]); however, it is surprising that several CV cycles to 1.5V SCE were required to activate OER on PtAg octahedra. This result suggests that PVP interactions with Ag may be stronger than with Pt, i.e., PVP binds to and stabilizes the PtAg surface, resulting in minimal OER activity until Ag is removed. We note that this latter hypothesis is consistent with differences in the molecular interactions of PVP with Pt vs. Ag, as witnessed by ^{13}C NMR results (see Fig. 2.3). Given that Ag is known to lower heats of adsorption for C_2H_2 and

C_2H_4,[14,42] the segregation of Ag at the surface ofPt octahedra should produce a catalyst that is selective for partial hydrogenation of C_2H_2.

2.3.4 Gas-phase hydrogenation of C_2H_2

The influence of Ag on the reactivity and stability of Pt NP surfaces was investigated by measuring C_2H_2 hydrogenation activity and selectivity for each catalyst (i.e., various NP shapes, with and without Ag at 1-2 wt% Pt loading on SiO_2) in a recirculating batch reactor from 30-220 °C. Overall, Pt NP surfaces with sub-monolayer quantities of Ag showed high C_2H_4-to-C_2H_6 selectivity ($S_{C2H4/C2H6}$, based on product mole fraction ratios; see Figure 2.6).

Evolution of $S_{C2H4/C2H6}$ for various NP catalysts at different operating conditions is summarized in Figure 2.7; these data clearly demonstrate that sub-monolayer levels of Ag have a dramatic effect on selectivity, even at low C_2H_2 partial pressures. For instance, Pt cubes with ~0.06 ML Ag were more selective at higher conversion compared to Pt-only catalysts at both 100 and 120 ^{o}C; however, the partial hydrogenation channel for both catalysts decreased with increasing temperature (arrows). In stark contrast, $S_{C2H4/C2H6}$ for $Pt_{91}Ag_9$ octahedra increased slightly with temperature and remained high (>6) for conversions up to 80%. This observation suggests that ~0.50 ML Ag coverage is sufficient to alter a majority of the NP surface, which is sustained even at high temperatures.

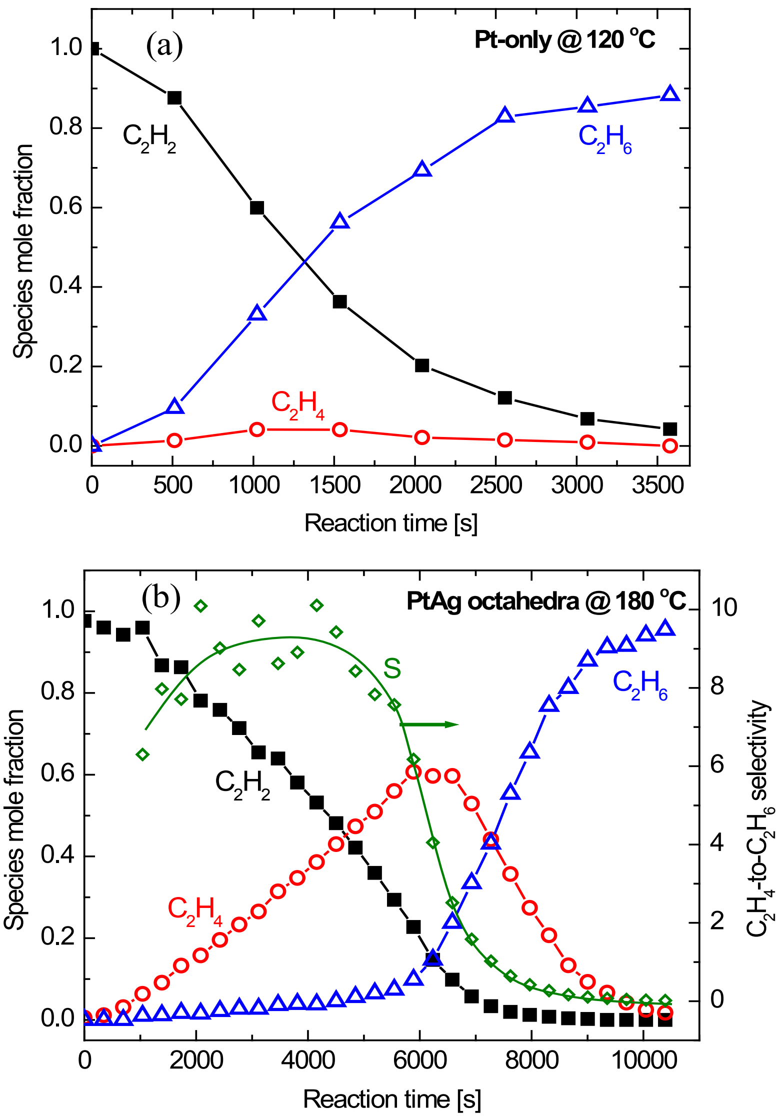

Figure 2.6. Catalytic data for C_2H_2 hydrogenation using supported (a) Pt-only nanoparticles at 120 °C and (b) PtAg octahedra at 180 °C in a recirculating batch reactor. C_2H_4-toC_2H_6 selectivity, obtained from product mole fractions at each reaction time, is plotted for the octahedra case. Lines are only intended to guide the eye.

Obtaining high turnover rates for partial hydrogenation of C_2H_2 at high temperatures is challenging because (1) surface coverage is lower, (2) preferential adsorption of C_2H_2 compared to C_2H_4 is washed out (i.e., the difference in adsorption equilibria decreases[43]), and (3) surface alloy compositions can change. However, adding Ag to the Pt surface appears to maintain preferential C_2H_2 adsorption, even at high temperatures for both NP and traditionally-prepared PtAg catalysts. Figure 2.8 shows that the common temperature-induced tradeoff between rate and selectivity (i.e., higher rate at the expense of lower selectivity) does not apply to the $Pt_{91}Ag_9$ octahedra and $Pt_{87}Ag_{13}$ catalysts. In contrast, pure Pt and Pd, as well as PdAg, are not selective over all temperature ranges tested (30-100 °C). The latter is not surprising, given that PdAg catalysts are often promoted with alkali metals (0.05-5 wt.%) to become selective for partial hydrogenation.[15,16]

Evolution of $S_{C2H4/C2H6}$ for various NP catalysts at different operating conditions is summarized in Figure 2.7; these data clearly demonstrate that sub-monolayer levels of Ag have a dramatic effect on selectivity, even at low C_2H_2 partial pressures. For instance, Pt cubes with ~0.06 ML Ag were more selective at higher conversion compared to Pt-only catalysts at both 100 and 120 ^{o}C; however, the partial hydrogenation channel for both catalysts decreased with increasing temperature (arrows). In stark contrast, $S_{C2H4/C2H6}$ for $Pt_{91}Ag_9$ octahedra increased slightly with temperature and remained high (>6) for conversions up to 80%. This observation suggests that ~0.50 ML Ag coverage is sufficient to alter a majority of the NP surface, which is sustained even at high temperatures.

Obtaining high turnover rates for partial hydrogenation of C_2H_2 at high temperatures is challenging because (1) surface coverage is lower, (2) preferential adsorption of C_2H_2 compared to C_2H_4 is washed out (i.e., the difference in adsorption equilibria decreases[43]), and (3) surface alloy compositions can change. However, adding Ag to the Pt surface appears to maintain preferential C_2H_2 adsorption, even at high temperatures for both NP and traditionally-prepared PtAg catalysts. Figure 2.8 shows that the common temperature-induced tradeoff between rate and selectivity (i.e., higher rate at the expense of lower selectivity) does not apply to the $Pt_{91}Ag_9$ octahedra and $Pt_{87}Ag_{13}$ catalysts. In contrast, pure Pt and Pd, as well as PdAg, are not selective over all temperature ranges tested (30-100 °C). The latter is not surprising, given that PdAg catalysts are often promoted with alkali metals (0.05-5 wt.%) to become selective for partial hydrogenation.[15,16]

2.4. Discussion

Synthesis of Pt NPs in the presence of PVP surfactant and Ag^+ as a growth promoter resulted in shaped NPs (e.g. cubes, cuboctahedra, and octahedra) with Ag-doped Pt surfaces. Ag^+ ions are thought to selectively deposit onto (100) planes of Pt and promote galvanic exchange with H_2PtCl_6 to form shaped NPs during synthesis.[26] While the majority of $AgNO_3$ reacts to form AgCl, this work has established that sub-monolayer quantities (i.e., 1-9 mol% Ag, 0.06-0.5 ML) remain on the surface of

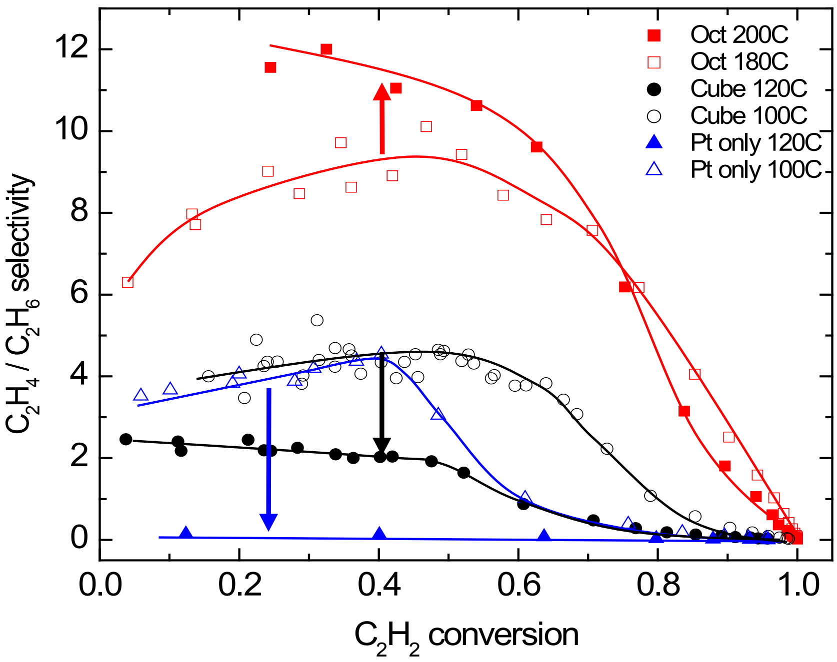

Figure 2.7. Evolution of C_2H_4-toC_2H_6 selectivity for Pt-only (triangles), $Pt_{99}Ag_1$ cube (circles), and $Pt_{91}Ag_9$ octahedra (squares) catalysts at different reaction temperatures. As shown, selectivity decreases at high C_2H_2 conversion and catalysts with low Ag content (Pt-only and cubes) become less (or non) selective at higher reaction temperatures. Lines are only intended to guide the eye.

~7 nm cubic and octahedral Pt NPs. Surface segregation of Ag was qualitatively assessed using solid-state $^{13}C\{^1H\}$ CP NMR of PVP bound to the NP surfaces, which revealed nearly identical spectra for Ag-only and octahedral Ag-doped Pt NPs. Furthermore, loss of α, β, and C=O ^{13}C resonances of PVP suggests surface Ag promotes polymer cleavage to form hydrocarbon, amine, and X-C=O fragments that may play a pivotal role in the formation of different NP shapes.

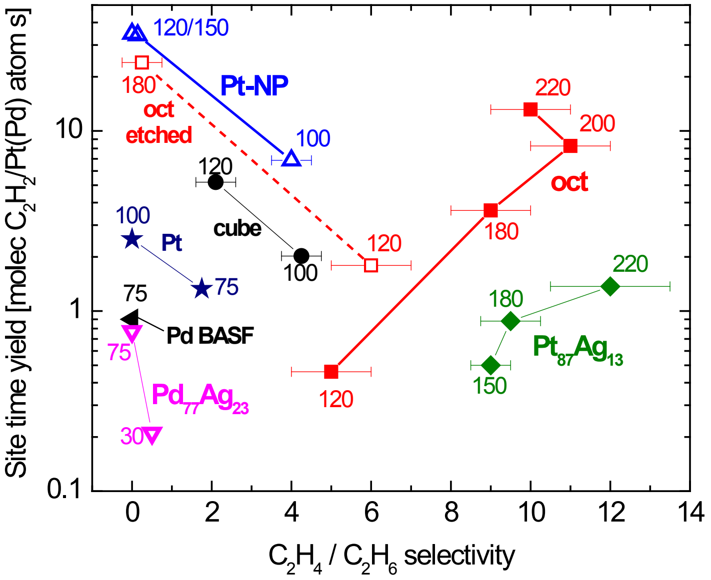

Figure 2.8. Site time yield (STY)-selectivity behavior for different SiO_2 supported catalysts. *Nanoparticles:* Pt-only NPs (up triangles), $Pt_{99}Ag_1$ cubes (circles), as-made $Pt_{91}Ag_9$ octahedra (closed squares), and etched $Pt_{97}Ag_3$ octahedra (open squares). *Traditionally-prepared:* Pt (stars), Pd-BASF Escat 1315 (left triangle), $Pd_{77}Ag_{23}$ (down triangle), and $Pt_{87}Ag_{13}$ (diamonds). STY is calculated as C_2H_2 molecules reacting per surface Pt (Pd) atom per second, based on the Ag-free Pt(Pd)-atom dispersion calculated from particle size and shape. Higher temperatures (annotated) result in high rate and low selectivity for catalysts with low Ag content (Pt-only, Pt-cubes with <0.06 ML Ag, and etched octahedra), whereas, higher Ag content ($Pt_{91}Ag_9$ octahedra and $Pt_{87}Ag_{13}$) resulted in reasonable rate and high selectivity above 180 °C. Unpromoted $Pd_{77}Ag_{23}$ on SiO_2 was the least active and (non)selective catalyst tested. Error bars on the selectivity axis represent the range of selectivity values measured for C_2H_2 conversions from ~10-50%. Lines are only intended to guide the eye.

Qualitative assessments on the effect of surface Ag on Pt NP reactivity for OER and HER/HOR was made using electrochemical methods. As Ag coverage increased, CVs showed a significant decrease in OER activity (higher overpotential) relative to a Pt-only surface. In addition, CV scans before and after rigorous electrochemical cleaning of particles revealed that Ag was much more difficult to remove than anticipated, possibly due to stronger PVP-Ag interactions that are consistent with ^{13}C NMR. The removal of Ag, via CV cycling and HNO_3 etching, lowered OER overpotentials to that of pure Pt. Interestingly, both HER and HOR activity were retained before and after removal of Ag, an example of how alloying can promote combinations of reactivity that originate from the parent elements.

The presence of sub-monolayer quantities of Ag on the surface of Pt (nanoparticles especially) was seen to favorably influence C_2H_2 hydrogenation selectivity. When compared to Pt-only NP catalysts, 0.06 ML Ag on cubic Pt NP catalysts resulted in lower activities with no increase in selectivity. However, ~0.5 ML Ag on octahedral Pt NPs resulted in significantly higher selectivity with C_2H_2 STY's comparable to Pt-only catalysts. The ability of Ag to promote preferential adsorption of C_2H_2 over C_2H_4 at high reaction temperatures suggests that the surface Ag composition is stable over a large operating window (100-220 °C). This capability with PtAg is contrasted to the PdAg case, where (1) higher temperatures can cause surface restructuring that often results in catastrophic drops in selectivity,[18] and (2) alkali metal promotion is required for high selectivity.[15,16] Thus, in systems where surface enrichment is driven by low solubility, bimetallic NP catalysts with stable surface compositions and novel reactivity can be realized.

Changes in activity-selectivity regimes as more Ag is doped onto Pt surfaces suggest how active sites on initially shaped Pt NPs are being modified. Ag has been observed previously to migrate towards step sites on Pt (111) surfaces prior to monolayer mixing.[21] In addition, step and edge sites on Pt are known to have high reactivity,[44] which are likely responsible for total hydrogenation of C_2H_2.[45] A significant decrease in overall activity for 0.06 ML Ag coverage would suggest that Ag blocks steps, edges, and corners of cubic, and likely octahedral, Pt NPs If the highly active edge sites of a cubic Pt NP (~10% in our case) are indeed blocked by Ag, then the reactivity observed reflects chemical transformations occurring primarily on (100) terraces. It can be envisioned that after blocking of highly active edge sites on a cube or octahedron, the electronic structure and reactivity will be further altered if more Ag is incorporated onto either Pt (100) or (111) terraces. As C_2H_2 hydrogenation is thought to be structure-insensitive,[46] the observed changes in surface reactivity are likely due to Ag coverage rather than reactivity differences due to faceting (i.e., (111) vs. (100)). For 0.5 ML Ag coverage, there is enough Ag to block edge sites and be incorporated onto (111) planes of an octahedral Pt NP. The higher Ag coverage for this case provides preferential access to chemically-selective C_2H_2 hydrogenation sites. Indeed, the high STY and selectivity at high temperatures for the 0.5 ML Ag case (octahedra), as compared to the 0.06 ML Ag case (cubes), shows that higher Ag coverage biases the C_2H_2 to C_2H_4 adsorption equilibrium towards partial hydrogenation. It is possible that further sub-monolayer Ag doping may promote higher selectivity at elevated temperatures (>200 °C) so long as NP sintering does not occur. However, additional Ag MLs on Pt produce lower STYs with comparable selectivities, as demonstrated by the traditionally-prepared $Pt_{87}Ag_{13}$ catalyst; clearly, there should be an optimal Ag coverage that can achieve the highest STY-selectivity combination. Furthermore, it is also possible that thermally-induced rearrangements and exchange of surface Ag and Pt atoms at elevated temperatures may provide access to new reactivity regimes for other reactions of interest, even for traditionally-prepared PtAg catalysts.

2.5. Conclusions

This work has demonstrated that sub-monolayer quantities of Ag on the surface of Pt provide a more effective surface environment, compared to Pt-only, Pd, and PdAg catalysts, for partial hydrogenation of C_2H_2 to C_2H_4 under H_2-rich conditions. Modification of the physical and electronic environment of Pt NP surfaces via Ag doping was evidenced by ^{13}C NMR of PVP-nanoparticle interactions and changes in HER/OER electrocatalytic activity. Octahedral PtAg NPs in the 6-8 nm range with 0.5 ML Ag, as well as traditionally-prepared $Pt_{87}Ag_{13}$ catalysts, provided a unique combination of reasonable turnover and selective formation of C_2H_4 over a wide range of C_2H_2 partial pressures and temperatures (100-220 °C). This work has shown that bimetallic systems with limited solubility can promotestable surface compositions, whichcan provide access to novel reactivity that may not be obtainable with miscible alloys or systems requiring alkali metal promotion.

2.6. Acknowledgments

This research work was supported by the National Science Foundation CAREER Program under Award No. CHE-0953441 and utilized facilities supported by the MRSEC Program of the National Science Foundation under Award No. DMR-1121053. The authors also thank the NSF-IOSE-PIRE Program, Award No. 0968399 for fellowship support.

2.7. References

(1) Henry, C. Adsorption and Reaction at Supported Model Catalysts. In Catalysis and Electrocatalysis at Nanoparticle Surfaces; Wieckowski, A., Savinova, E. R., Vayenas, C. G., Eds.; *Marcel-Dekker, Inc*.: New York, **2009**.

(2) Bratlie, K. M.; Lee, H.; Komvopoulos, K.; Yang, P.; Somorjai, G. A. *Nano Lett.* **2007**, *7*, 3097.

(3) Sun, Y.; Xia, Y. *Science* **2002**, *298*, 2176.

(4) Minato, T.; Susaki, T.; Shiraki, S.; Kato, H. S.; Kawai, M.; Aika, K. *Surf. Sci.* **2004**, *566*, 1012.

(5) Molina, L.; Hammer, B. *Phys. Rev. B* **2004**, *69*, 155424.

(6) Yoon, B.; Häkkinen, H.; Landman, U.; Wörz, A. S.; Antonietti, J.; Abbet, S.; Judai, K.; Heiz, U. *Science* **2005**, *307*, 403.

(7) Nørskov, J.; Bligaard, T.; Rossmeisl, J.; Christensen, C. *Nat. Chem.* **2009**, *1*, 37.

(8) Stephens, I. E. L.; Bondarenko, A. S.; Perez-Alonso, F. J.; Calle-Vallejo, F.; Bech, L.; Johansson, T. P.; Jepsen, A. K.; Frydendal, R.; Knudsen, B. P.; Rossmeisl, J.; Chorkendorff, I. *J. Am. Chem. Soc.* **2011**, *133*, 5485.

(9) Fu, Q.; Li, W.; Yao, Y.; Liu, H.; Su, H.; Ma, D.; Gu, X.; Chen, L.; Wang, Z.; Zhang, H.; Wang, B.; Bao, X. *Science* **2010**, *328*, 1141.

(10) Yamada, Y.; Tsung, C.-K.; Huang, W.; Huo, Z.; Habas, S. E.; Soejima, T.; Aliaga, C. E.; Somorjai, G. A.; Yang, P. *Nat. Chem.* **2011**, *3*, 372.

(11) Iglesias-Juez, A.; Beale, A.; Maaijen, K.; Weng, T.; Glatzel, P. *J. Catal.* **2010**, *276*, 268.

(12) Müller, S.; Zunger, A. *Phys. Rev. Lett.* **2001**, *87*, 165502−1.

(13) Bos, A.; Westerterp, K. *Chem. Eng. Proc.* **1993**, *32*, 1.

(14) Studt, F.; Abild-Pedersen, F.; Bligaard, T.; Sorensen, R.; Christensen, C.; Nørskov, J. *Angew. Chem., Int. Ed.* **2008**, *47*, 9299.

(15) Cheung, T.-T.; Johnson, M.; Brown, S.; Zisman, S.; Kimble, J. U.S. Patent 5,510,550, **1996**.

(16) Blankenship, S.; Voight, R.; Perkins, J.; Fried Jr., J. U.S. Patent 6,509,292 B1, **2003**.

(17) Wakabayashi, N.; Takeichi, M.; Uchida, H.; Watanabe, M. *J. Phys. Chem. B* **2005**, *109*, 5836.

(18) Jin, Y.; Datye, A.; Rightor, E.; Gulotty, R.; Waterman, W.; Smith, M.; Holbrook, M.; Maj, J.; Blackson, J. *J. Catal.* **2001**, *203*, 292.

(19) Somorjai, G.; Park, J. *Angew. Chem., Int. Ed.* **2008**, *47*, 9212.

(20) Durussel, P.; Feschotte, P. *J. Alloys Compd.* **1996**, *239*, 226.

(21) Röder, H.; Schuster, R.; Brune, H.; Kern, K. *Phys. Rev. Lett.* **1993**, *71*, 2086.

(22) Calvo, F.; Cottancin, E.; Broyer, M. *Phys. Rev. B* **2008**, *77*, 121406(R).

(23) Strohl, J. K.; King, T. S. *J. Catal.* **1989**, *116*, 540.

(24) Rioux, R.; Song, H.; Grass, M.; Habas, S.; Niesz, K.; Hoefelmeyer, J.; Yang, P.; Somorjai, G. *Top. Catal.* **2006**, *39*, 167.

(25) Grass, M.; Yue, Y.; Habas, S.; Rioux, R.; Teall, C.; Yang, P.; Somorjai, G. A. *J. Phys. Chem. C* **2008**, *112*, 4797.

(26) Song, H.; Kim, F.; Connor, S.; Somorjai, G.; Yang, P. *J. Phys. Chem. B* **2005**, *109*, 188.

(27) Bard, A. J.; Faulkner, L. R. Electrochemical methods: fundamentals and applications, 2nd ed.; *John Wiley & Sons, Inc.*: New York, **2001**.

(28) Dixit, S.; Mahadeshwar, A.; Haram, S. *Colloids Surf., A* **1998**, *133*, 69.

(29) Onsgaard, J.; Godowski, P.; Li, Z. *J. Vac. Sci. Techol.,* A **2012**, *30*, 01A111−1.

(30) Peng, Z.; Yang, H. *Nano Today* **2009**, *4*, 143.

(31) Benson, J.; Boudart, M. *J. Catal.* **1965**, *4*, 704.

(32) Zheng, S.; Guo, Q.; Mi, Y. *J. Polym. Sci., Part B: Polym. Phys.* **1999**, *37*, 2412d.

(33) Markovic, N. M.; Gasteiger, H. A.; Ross, P. N. *J. Phys. Chem.* **1995**, *99*, 3411.

(34) Faguy, P. W.; Markovic, N.; Adzic, R. R.; Fierro, C. A.; Yeager, E. B. *J. Electroanal. Chem.* **1990**, *289*, 245.

(35) Wieckowski, A.; Zelanay, P.; Varga, K. *J. Chem. Phys.* **1991**, *88*, 1247.

(36) Solla-Gullon, J.; Rodriguez, P.; Herrero, E.; Aldaz, A.; Feliu, J. M. *Phys. Chem. Chem. Phys.* **2008**, *10*, 1359.

(37) Conway, B. E.; Angerstein-Kozlowska, H.; Sharp, W. B. A. *Anal. Chem.* **1973**, *45*, 1331.

(38) Solla-Gullon, J.; Montiel, V.; Aldaz, A.; Clavilier, J. *J. Electroanal. Chem.* **2000**, *491*, 69.

(39) Solla-Gullon, J.; Montiel, V.; Aldaz, A.; Clavilier, J. *J. Electrochem. Soc.* **2003**, *150*, E104.

(40) Sanchez-Sanchez, C. M.; Solla-Gullon, J.; Vidal-Iglesias, F. J.; Aldaz, A.; Montiel, V.; Herrero, E. *J. Am. Chem. Soc.* **2010**, *132*, 5622.

(41) Hansen, H. A.; Rossmeisl, J.; Nørskov, J. K. *Phys. Chem. Chem. Phys.* **2008**, *10*, 3722.

(42) Bond, G.; Wells, P. *J. Catal.* **1965**, *4*, 211.

(43) Huang, W. H.; McCormick, J. R.; Lobo, R. F.; Chen, J. G. *J. Catal.* **2007**, *246*, 40.

(44) Tao, F.; Dag, S.; Wang, L.-W.; Liu, Z.; Butcher, D.; Bluhm, H.; Salmeron, M.; Somorjai, G. *Science* **2010**, *327*, 850.

(45) Arafa, E. A.; Webb, G. *Catal. Today* **1993**, *17*, 411.

(46) Sheth, P.; Neurock, M.; Smith, C. *J. Phys. Chem. B* **2005**, *109*, 12449.

Chapter 3

Influence of Step-Edge vs. Terrace Sites on Temperature-Dependent C_2H_2 Hydrogenation with Ag-doped Pt Nanoparticles

---

Adapted from the Journal of Physical Chemistry C:

Louis C. Jones and Michael J. Gordon, *J. Phys. Chem. C.* 116, 23472-23476 (**2012**).

Department of Chemical Engineering, University of California, Santa Barbara, Santa Barbara, California 93106-5080, USA

Abstract

Ag-doped Pt nanoparticles (NP) were tested for continuous-flow C_2H_2 hydrogenation reactivity and CO adsorption−desorption from 100 to 300 °C to investigate how submonolayer levels of an insoluble metal dopant can distribute on steps and terraces of a NP surface and modify reactivity. High Ag coverage (0.5 monolayer, ML) on Pt promoted selective hydrogenation of C_2H_2 at $T < 200$ °C; at higher temperatures, both low (0.06 ML) and high (0.5 ML) Ag coverages were seen to increase selective C_2H_4 formation. Ag incorporation onto Pt step and terrace sites, and resultant temperature-dependent desorption behavior, were probed using *in situ* diffuse reflectance infrared Fourier transform spectroscopy (DRIFTS) with CO. At low coverage, Ag appeared to occupy Pt step sites; for higher coverage, Ag occupied both step and terrace sites, which lowered the CO desorption temperature. Highly correlated reactivity and DRIFTS data show the importance of step site blocking and desorption from Pt during selective C_2H_2 hydrogenation. Multiple reaction cycles from 100 to 300 to 100 °C demonstrate how immiscible metal dopants can preferentially modify nanoparticle surface compositions and promote active, selective, and stable catalysts over large temperature operating windows.

3.1. Introduction

Alloying has been a successful approach to improve the reactivity of transition metal heterogeneous nanoparticle (NP) catalysts. For example, the addition of particular "dopant" atoms to the NP surface and interior has been observed to increase turnover,[1] improve selectivity,[2] enhance resistance to deactivation,[3] and promote multi-functionality;[4] these observations have been attributed to changes in surface atom arrangements and electronic structure.[5,6] However, the reactivity of alloyed NP catalysts often evolves during reaction, particularly at higher operating temperatures, where atoms can easily diffuse and alter surface composition and structure.[7] Dynamic rearrangements, coupled with adsorption of strongly bound intermediates, can make “stable” surface compositions which promote high reactivity difficult to achieve over a large range of operating conditions. As such, obtaining insight into improving the activity and selectivity of NP alloy catalysts is a challenging task.

Supported catalysts based on the miscible[8,9] PdAg system (with alkali-metal promoters) have been used industrially for selective hydrogenation of C_2-C_3 alkynes to alkenes at low temperatures (30-150 °C).[10,11,12] *In situ* poisoning of highly-active Pd surface sites with trace levels of CO is also a common trick to increase selectivity.[10] Ag doping of the catalyst is hypothesized to minimize β-hydride formation on Pd and decrease the adsorption energy of C_2H_4 relative to C_2H_2[13] through both ensemble and electronic effects.[5] Unfortunately, at higher temperatures, the surface composition and structure of PdAg can change substantially due to miscibility,[7,14] leading to severely diminished selectivity.

However, an appropriate alloy system can sometimes be chosen such that surface enrichment of a particular component is inherently favored, which provides a systematic way to selectively alloy the NP surface and modify reactivity. For example, it was recently shown[15] that the immiscible[16,17] PtAg system could achieve high selectivity and turnover (at rates comparable to pure Pt) for C_2H_2-to-C_2H_4 hydrogenation with only sub-monolayer (ML) coverage of Ag. Interestingly, increasing activity at the expense of selectivity, which is the common tradeoff encountered for hydrogenation catalysts,[18] did *not* occur for PtAg at temperatures up to 200 ^{o}C. This trend, i.e., simultaneously high activity and selectivity at elevated temperatures, was hypothesized to arise from increased stability of NP surface compositions due to the immiscible nature of Pt and Ag.[15]

In this work, we elucidate how Ag doping affects the reactivity (turnover and selectivity) of Pt NP surfaces with combined catalytic testing and *in situ* IR spectroscopy. Specifically, we show how sub-monolayer Ag affects (1) Pt NP step and terrace site distributions, (2) desorption behavior of CO, and (3) partial hydrogenation of C_2H_2. Automated reactive cycling from 100→300→100 ^{o}C (i.e., >20 hrs on stream) was carried out to examine the stability and temperature-dependent reactivity of Pt NP catalysts with and without Ag. Increasing the Ag coverage from 0.06→0.5 ML resulted in high selectivity and an increase in light-off temperature (50% C_2H_2 conversion), consistent with previously-reported batch measurements.[15] Moreover, the PtAg NP catalysts displayed reproducible activity and selectivity for C_2H_2 hydrogenation over multiple thermal cycles to 300 °C. Continuous-flow *in situ* diffuse reflectance infrared Fourier transform spectroscopy (DRIFTS) was carried out using CO adsorption-desorption (100 → 300 ^{o}C) as a molecular probe of changes in Pt step and terrace site distributions due to Ag coverage in the low (T < 200 °C) and high (T ≥ 200 °C) temperature reaction regimes. It was found that Ag at low coverage preferentially incorporated at step and edge sites on Pt NPs, while higher coverage led to further Ag incorporation into terrace sites that manifested as large shifts in atop (linearly-bound) CO to lower IR frequencies. The relative distribution of step vs. terrace sites and the temperature-dependent frequency shifts of ν(CO) in the low and high-T regimes correlated well with continuous-flow C_2H_2 hydrogenation light-off and selectivities measured for various Pt_xAg_y NP catalysts. The data also suggest that Ag modifies Pt site distributions and the electronic structure of Pt NP surfaces. Ultimately, Ag-doping of Pt steps and terraces, in conjunction with changes in temperature-dependent adsorption/desorption processes, explains how PtAg NP catalysts can be highly active for partial hydrogenation of C_2H_2 at high reaction temperatures.

3.2. Experimental Section

Surface Ag-doped Pt nanoparticles (e.g., 1 mol% Ag on Pt cubes, 7 mol% Ag on Pt cuboctahedra, and 9 mol% Ag on Pt octahedra in the 7-8 nm size range) were synthesized and subsequently characterized, supported, and activated as detailed elsewhere.[15,19] Catalysts were evaluated throughout synthesis, as well as before and after reactivity testing, using x-ray diffraction (XRD), inductively-coupled plasma elemental analysis (ICP), transmission electron microscopy (TEM), and x-ray photoelectron spectroscopy (XPS). XRD and ICP analysis *before and after* calcination and etching revealed that supported NP catalysts were highly crystalline (i.e., Pt (111) peaks were easily visible with no crystalline Ag phases present) and uniform (7-8 nm via Scherrer analysis); additionally, TEM analysis showed that particle sintering did not occur after calcination and repeated, continuous-flow reactivity testing to 300 °C (see TEM images in Figure 3.1).

Supported catalysts were tested for continuous-flow C_2H_2 hydrogenation in a plug flow reactor (1/4” glass tube; 10-25 mg catalyst; 25 mg colloidal SiO_2 before and after the catalyst bed; 20 sccm continuous flow of 1:4 C_2H_2:H_2; space time = 0.8-1 sec) with automated temperature and mass-flow control, as well as online GC analysis of reaction products. 100% excess H_2 for the totally hydrogenated product (C_2H_6) was specifically chosen to assess the inherent chemical selectivity of the catalyst to promote C_2H_2 to C_2H_4. Light-off curves/product distributions were measured using an automated 100→300→100 °C temperature cycle which consisted of three GC analyses at each reaction temperature (e.g., 10-50 °C intervals) to ensure steady-state operation. A dual up-and-down ramping sequence (i.e., total time on stream ~20 hrs) was used to evaluate deactivation and/or hysteresis in the light-off behavior. Mass balance closure on the continuous flow reactor was established through quantitative analysis of the C_2H_2 feed and gaseous products (C_2H_2, C_2H_4, and C_2H_6). Batch reactions were carried out in a recirculating system as detailed elsewhere.[15] NP catalysts with 0.3, 2, and 3 mol% Ag were synthesized by etching the supported 1%, 7%, and 9% Ag catalysts in 8M HNO_3 for 20 min,[20] and a standard incipient wetness Pt-only NP catalyst was synthesized for comparison (e.g., $H_2Pt(OH)_6$ + colloidal SiO_2 with ~2 wt.% Pt loading).

NP catalysts were characterized spectroscopically using *in situ* DRIFTS (Bruker Equinox 55 FTIR) with flowing CO (50 sccm of 1% CO in N_2) in a custom, temperature-controlled flow reactor with ZnSe hemispherical dome based on a Harrick Scientific Praying Mantis. Samples were prepared by pressing pre-ground catalyst (1-2 wt% Pt on SiO_2) into an aluminum sample holder, drying in He, and reducing in H_2 (20 sccm for 20 min) at 120 ^{o}C before measurements. Automated mass-flow and temperature control were used to reproducibly probe temperatures from 100-300 ^{o}C, with synchronized acquisition of interferograms (3 scans x 500 averages/scan over ~20 min) at each temperature. All spectra were ratioed to an He-only background spectrum of each catalyst taken at 100 ^{o}C immediately before CO was introduced. Step and terrace peak positions for atop CO were deconvoluted by fitting DRIFTS spectra with double Lorentzians. Further details regarding *in situ* CO adsorption experiments and are provided in Appendix B.

3.3. Results and Discussion

The influence of surface Ag on the partial hydrogenation selectivity of C_2H_2 was evaluated in a continuous flow reactor using Pt NP catalysts with different Ag-doping levels (1, 7, and 9 mol% Ag, equivalent to coverages of 0.06, 0.47, and 0.51 monolayer, respectively); see the Experimental section for details on synthesis, characterization, and testing. Catalysts consisted of ~7-8 nm Pt_xAg_y NPs supported on colloidal SiO_2 with 1-2 wt.% Pt loading, and morphology was monitored throughout preparation using TEM (Fig. 3.1) and XRD, which showed no signs of sintering or separate Pt or Ag phases.

Catalyst reactivity was analyzed by monitoring the C_2H_2 exit mole fraction (conversion), C_2H_4-to-C_2H_6 selectivity, and mass balance closure trends for temperature ramps from 100-300-100 °C as shown in Figure 3.2. Several general observations can be made from the data: (1) 1% Ag NPs were highly active ($y_{C2H2,exit} = 0$) but not selective ($S = y_{C2H4}/y_{C2H6} < 1$) for $T < 200$ °C (Fig. 3.2c), (2) 9% Ag NPs light off rapidly at ~210 °C and showed preferential C_2H_4 production ($S > 10$) near 200 °C (Fig. 3.2d), (3) both 1% and 9% Ag NPs were highly selective for C_2H_4 production for $T > 200$ °C (Figs. 3.2c,d), (4) etching catalysts in 8M HNO_3 resulted in low selectivity for all temperatures (Figs. 3.2g,h), and (5) catalysts did not show significant light off hysteresis or deactivation throughout the 20 hr up-and-down temperature ramps. From these data, it is clear that Ag influences Pt NP reactivity differently at low ($T <200$ °C) vs. high ($T >200$ °C) temperatures. At low-T, increasing Ag (1%→9%) results in high selectivity (S_{max}~11) with rapid light off at ~180 °C (50% C_2H_2 conversion), followed by a rapid fall off in S at ~200 °C where conversion goes to 100%. The latter trend is due to the sudden availability of surface sites where C_2H_4 can rapidly hydrogenate[21] in excess H_2 (i.e., all of the more strongly bound C_2H_2 has reacted to C_2H_4, freeing up surface sites for C_2H_4 turnover). At high-T, both large and small quantities of Ag provide reasonable selectivity ($S >4$), even at 100% C_2H_2 conversion (Figs. 3.2c,d). These observations echo batch-mode data (Fig. 3.3) where both the site time yield (STY = C_2H_2 molecules reacted /

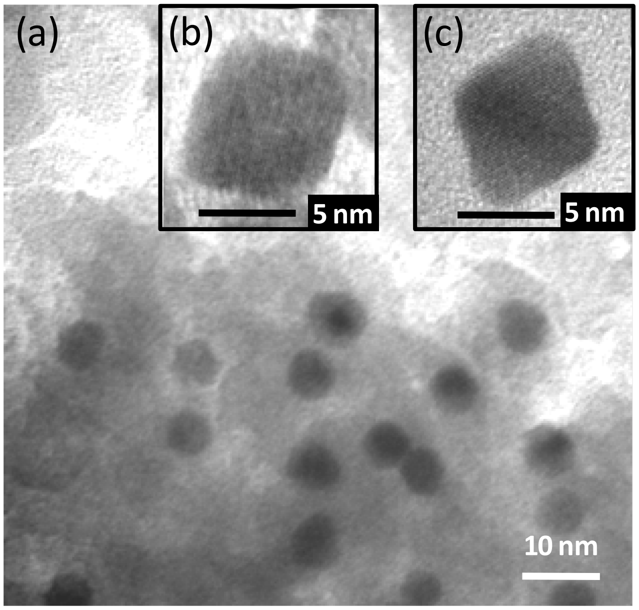

Figure 3.1. TEM images of (a) colloidal SiO_2-supported Pt octahedra with 9 mol% Ag after 300 °C reactivity testing, (b) as-made 1% Ag on Pt cubes, and (c) 9% Ag on Pt octahedra.

surface Pt atom • s) and selectivity increase with T for the 9% Ag catalyst at $T < 200$ °C; in contrast, the 1% Ag and Pt-only catalysts suffer from the common "activity-selectivity tradeoff"[18] where high turnover comes at the expense of total hydrogenation. This latter behavior is similar to acid-etched catalysts (0.3 and 3% Ag via etching of 1 and 9% Ag catalysts, respectively) which were very active and produced mostly C_2H_6.

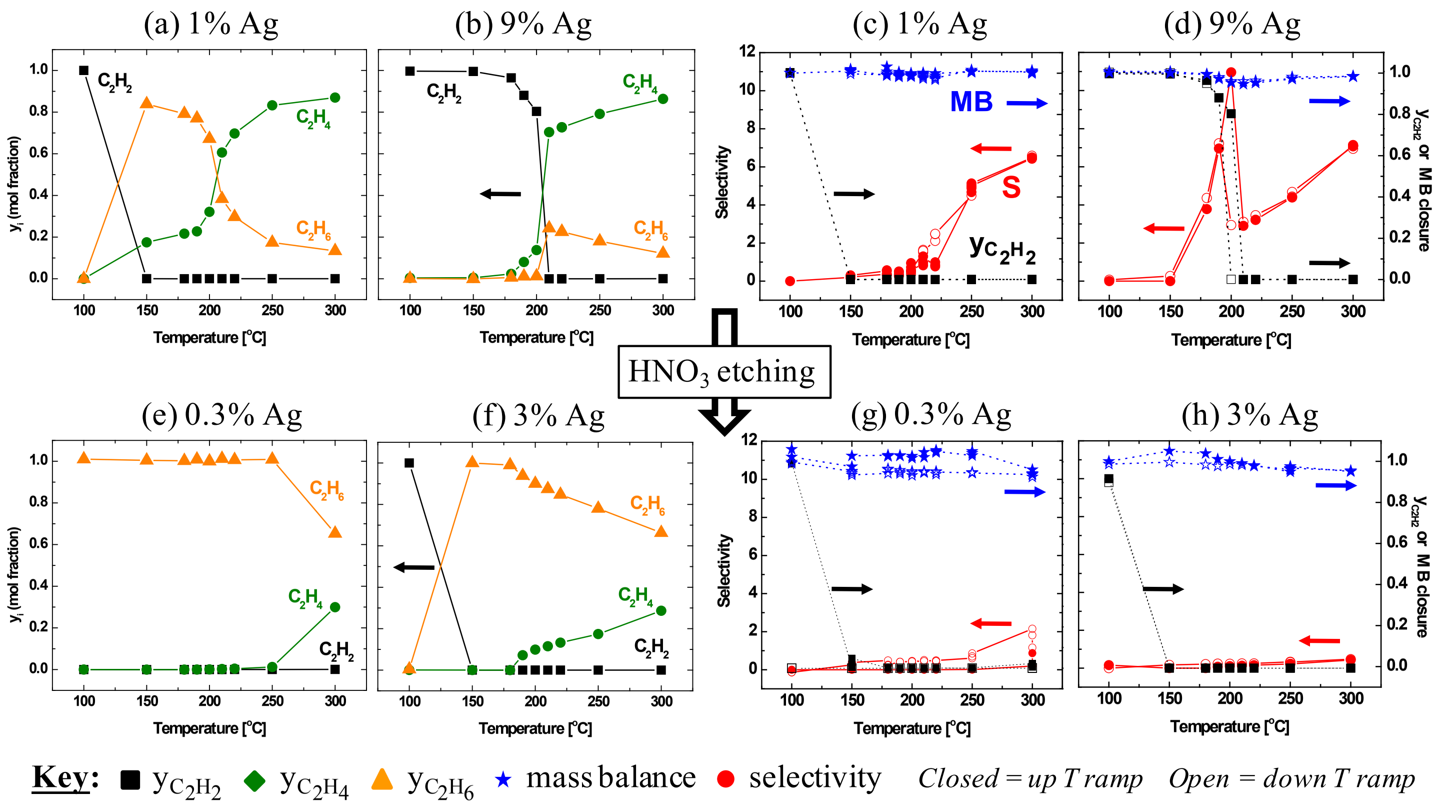

Figure 3.2. Continuous flow reactivity data (product mole fractions), light-off, mass balance closure (MB), and C_2H_4-to-C_2H_6 selectivity (S) for various Pt_xAg_y NP catalysts (a-d) along with their acid-etched (8M HNO_3) analogues (e-h).

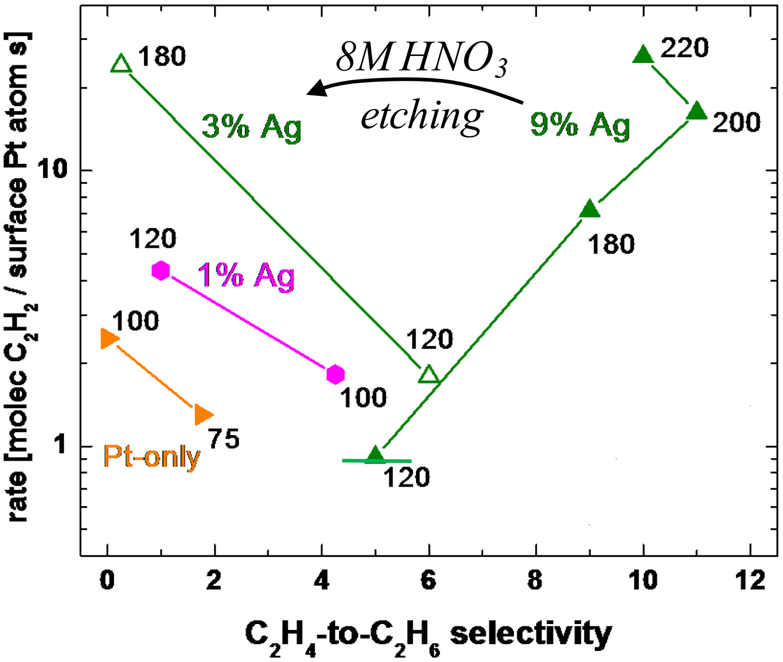

Figure 3.3. Batch mode C_2H_2 hydrogenation rate (site time yield) and selectivity behavior for Pt and Pt_xAg_y catalysts. Reaction temperatures are noted. The error bar on the selectivity axis refers to the average range of selectivity (y_{C2H4}/y_{C2H6}) values for C_2H_2 conversions from ~10-50%.

It is well known that CO adsorption occurs from 0-500 K on Pt[22,23] and from 0-120 K on Ag[24] surfaces. In addition, changes in the atop (linearly-adsorbed) CO vibrational frequency have been used to probe the extent to which Pt surfaces alloy, as well as to titrate different Pt surface sites.[23,25] We use the latter approach here, namely DRIFTS of CO adsorption under dynamic conditions, to investigate the effect of Ag doping on step vs. terrace site populations (Fig. 3.4a) to better understand how Ag modifies Pt reactivity at different temperatures. We specifically note that IR peak intensities of CO adsorption are *not* directly proportional to relative coverage (and therefore site populations) due to dipole-dipole coupling effects.[26] However, the appearance or disappearance of IR peaks does provide information about the presence of different adsorption sites. In addition, we favor the use of vibrational frequency *shifts* instead, which have been shown to be directly proportional to CO coverage.[26] To avoid misinterpretation, all DRIFTS spectra presented here were normalized by the CO peak height. It should also be noted that previous experimental and DFT studies have suggested that CO can promote Ag at Pt step sites to incorporate into Pt terraces (the "CO-induced mixing effect").[27] While displacement of Ag at Pt step sites may initially occur upon adsorption of CO, this would not affect the majority of Ag atoms (at most, 1 in 3 Ag atoms at Pt step sites) at the low CO coverages tested herein. Note that CO desorbs from Ag,[24] Pt terraces,[22,23] and Pt steps[22,23] at 120 K, 350 K, and ~450 K, respectively. Moreover, the steady state distributions of Pt step and terrace sites did not show evidence of Ag redistribution at all temperatures tested (100-300 ^{o}C).

Two distinct atop ν(CO) frequencies at 2077 and 2056 cm^{-1} were observed for 1% Ag on Pt NPs, which are assignable to terrace and step sites, respectively.[23] When this catalyst was etched in 8M HNO_3 (open symbols, 0.3% Ag after etching), the relative intensity of the 2056 cm^{-1} (step) peak increased, which indicates that Ag (previously) incorporated into step sites was removed. When the initial Ag coverage was increased to 7 and 9%, only step sites were observed. However, after etching,

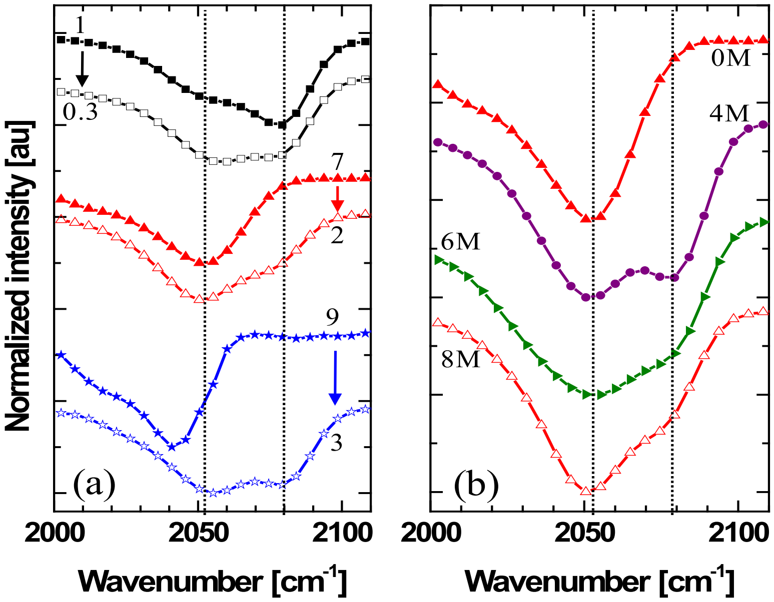

Figure 3.4. (a) *In situ* DRIFTS data of Pt_xAg_y nanoparticle catalysts in flowing CO (1% in N_2) at 100 °C (atop CO region). As-made (closed) and etched (open) catalysts are shown; arrows show spectral evolution due to etching in 8M HNO_3. Notations are mol% Ag in the catalyst. (b) CO adsorption at 60 °C for the 7% Ag catalyst etched in different molarity HNO_3. Lines are only intended to note the general location of ν(CO) for step (low cm^{-1}) and terrace (high cm^{-1}) sites.

both step and terrace sites appeared on these two catalysts, similar to the as-made 1% Ag case.

While it appears that Ag has significantly impacted the Pt terrace site population after the inclusion of 7 and 9 mol% Ag,[28] it is also likely that Ag is incorporated into step sites. Previous STM experiments have shown that Ag migrates to step sites on Pt(111) before being incorporated into terraces over the 400-700 K temperature range;[29] our data echo this finding, i.e., 1% Ag catalysts appear to have more Ag incorporation at steps (see Fig. 3.4a, namely the increase in step-to-terrace ratio after etching). For the 7% Ag case, Ag appears to block both step and terrace sites; in addition, progressive etching of Ag from this catalyst with HNO_3 (Fig. 3.4b) suggests that Ag is first removed from terrace sites (i.e., the terrace peak starts to appear at 4M), followed by Ag removal from steps (i.e., increase in the relative step-to-terrace ratio) at 6 and 8M.

Given this backdrop, a temperature-dependent *in situ* CO adsorption-desorption study was undertaken to probe how Ag modifies (dynamic) surface coverages and electronic structure of Pt. For example, Figure 3.5a (7% Ag) clearly shows that CO coverage is changing with T (i.e., atop CO shifts to lower frequency due to reduced coverage and dipole-dipole coupling[26]). Since low CO coverages are being probed in our experiment (i.e., above CO desorption temperatures, as measured via TPD[23]), coverage-dependent frequency shifts due to dipole-dipole interactions should be similar.[26] Moreover, if the CO-induced mixing effect[27] was significant, the frequency of atop CO on Pt steps would increase (i.e., CO coverage on Pt steps increases if Ag diffuses into the terrace); however, frequency shifts to lower wavenumber were observed. Thus, the difference in temperature-dependent CO frequency shifts with Ag coverage (Fig. 3.5b) suggests that Ag modifies the electronic structure of Pt. The electronic effect of Ag is consistent with the proposed notion that Ag diminishes the Pt 5d electron density,[30] which should decrease the CO adsorption energy on Pt[31] and/or influence activation energies for surface diffusion.[32] For instance, significant

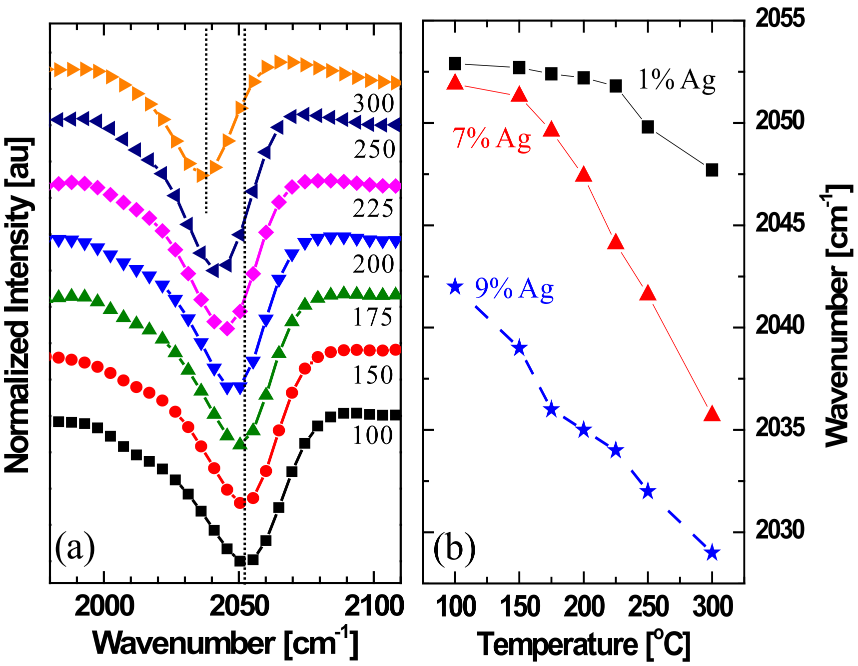

Figure 3.5. (a) Temperature evolution of CO adsorption on Pt nanoparticle catalyst with 7 mol% Ag measured with *in situ* DRIFTS. Dashed lines are only intended to illustrate the ν(CO) shift and temperatures are noted in °C. (b) Temperature shift of the step site ν(CO) frequency for Pt NP catalysts with different levels of Ag doping (1, 7, and 9% Ag).

ν(CO) shifts for the 1% Ag catalyst do not occur until ~225-300 ^{o}C, which is highly correlated to the increase in C_2H_2 hydrogenation selectivity (Fig. 3.2c). In contrast, the ν(CO) shift occurs at much lower temperatures (175-200 ^{o}C) for catalysts with higher Ag coverage (7 and 9%); interestingly, this shift correlates well with partial hydrogenation light-off (Fig. 3.2d) and selectivity jump, especially for the 9% Ag case.

The aforementioned reactivity and CO DRIFTS data suggest that (1) desorption of reactants (H_2, C_2H_2, C_2H_4) initiates low-T conversion of C_2H_2 with high selectivity for the 9% Ag catalyst, (2) the high-T increase in selectivity for 1% to 9% Ag is due to the influence of Ag on step site populations, and (3) etched catalysts are *not* selective and have low light-off temperatures because highly-active step sites are available for reaction. These findings substantiate previously-reported batch-mode reactivity data[15] where it was hypothesized that blocking of highly-active[33] steps, edges, and corners of a Pt NP would decrease turnover and reflect the inherent selectivity of Ag-free, Pt NP terraces (i.e., [100] or [111] facets, similar to the trends observed for the 1% Ag catalyst herein).

The high activity and selectivity for the 9% Ag catalyst at low-T likely occurs because Ag-doping blocks (total hydrogenating) step sites as well as modifies the desorption energetics of terraces. In the high-T case, the combination of step site blocking by Ag, enhanced reactant (H_2, C_2H_2, or C_2H_4) desorption, and (potential) coke/oligomer formation[34] on terrace sites appears responsible for the enhanced selectivity of all catalysts. With regard to the latter, mass balance closures, coupled with the lack of deactivation over the 20 hr reaction cycle to 300 °C, indicate that coking and/or oligiomer formation on the catalyst are not significant contributors to changes in reactivity. Notwithstanding, there is a clear and strong link between Ag's influence on step vs. terrace populations and reactivity. Overall, the DRIFTS data and reactivity trends suggest that Ag-doping of Pt, which likely reduces Pt ensembles required for hydrogenation,[7] in combination with the electronic influence of Ag on Pt (lower temperature desorption), promote partial hydrogenation of C_2H_2.

3.4. Conclusions

In summary, we have shown that bimetallic NPs composed of immiscible atomic species (e.g., PtAg) allows one to realize temperature-stable surface compositions that promote high selectivity and high activity simultaneously. It was seen that sub-monolayer levels of Ag on Pt can promote C_2H_2-to-C_2H_4 hydrogenation under excess H_2 at reaction temperatures from 100-300 °C in a continuous flow setting for multiple reaction cycles with little hysteresis in activity and selectivity. Analysis of gas compositions at each temperature suggested there were two distinct reactivity regimes: (1) from 100-200 °C, where high ($0.5 \leq \theta_{Ag} < 1$ ML) Ag coverage promotes high C_2H_4 selectivity (S >4), and (2) from 200-300 °C, where even small amounts of Ag ($\theta_{Ag} > 0.06$ ML) preferentially produce C_2H_4 as temperature increases. These regimes were further investigated using *in-situ* DRIFTS with CO to probe the influence of Ag on step and terrace site distributions and energetics. At small doping levels (~0.06 ML), Ag preferentially occupied highly-active Pt step sites. For higher doping levels (~0.5 ML), Ag occupied both step and terrace sites. Moreover, increased amounts of Ag caused CO desorption to occur at lower temperatures, which provided evidence for the electronic influence of Ag on Pt. These observations suggest that Ag incorporates first into step and edge sites of a Pt NP, and then further into terrace sites, consistent with previous UHV studies of Ag deposited on Pt(111) surfaces. Based on C_2H_2 hydrogenation and CO adsorption-desorption results, high selectivity at low-T was attributed to step site blocking by Ag. Overall, it was demonstrated how the immiscibility of Pt and Ag can inherently promote sub-monolayer amounts of Ag to incorporate into Pt NP surfaces, which produced stable, active, and selective catalysts for C_2H_2 partial hydrogenation.

3.5. Acknowledgments

This research work was supported by the National Science Foundation CAREER Program (CHE-0953441) and utilized facilities supported by the MRSEC Program of the National Science Foundation under Award No. DMR-1121053. The authors also thank the NSF-IOSE-PIRE Program (0968399) and the NSF ConvEne IGERT Program (NSF-DGE 0801627) for fellowship support.

3.6. References

(1) Stephens, I. E. L.; Bondarenko, A. S.; Perez-Alonso, F. J.; Calle-Vallejo, F.; Bech, L.; Johansson, T. P.; Jepsen, A. K.; Frydendal, R.; Knudsen, B. P.; Rossmeisl, J. et al. *J. Am. Chem. Soc.* **2011**, *133*, 5485-5491.

(2) Fu, Q.; Li, W.; Yao, Y.; Liu, H.; Su, H.; Ma, D.; Gu, X.; Chen, L.; Wang, Z.; Zhang, H. et al. *Science* **2010**, *328*, 1141-1144.

(3) Iglesias-Juez, A.; Beale, A.; Maaijen, K.; Weng, T.; Glatzel, P. *J. Catal.* **2010**, *276*, 268-279.

(4) Yamada, Y.; Tsung, C.-K.; Huang, W.; Huo, Z.; Habas, S. E.; Soejima, T.; Aliaga, C. E.; Somorjai, G. A.; Yang, P. *Nature Chemistry* **2011**, *3*, 372-376.

(5) Sheth, P.; Neurock, M.; Smith, C. *J. Phys. Chem. B* **2005**, *109*, 12449-12466.

(6) Nørskov, J.; Bligaard, T.; Rossmeisl, J.; Christensen, C. *Nature Chemistry* **2009**, *1*, 37-46.

(7) Khan, N. A.; Uhl, A.; Shaikhutdinov, S.; Freund, H.-J. *Surf. Sci.* **2006**, *600*, 1849-1853.

(8) Müller, S.; Zunger, A. *Phys. Rev. Lett.* **2001**, *87*, 165502-1-4.

(9) Kim, D. H.; Kim, H. Y.; Ryu, J. H.; Lee, H. M. *Phys. Chem. Chem. Phys.* **2009**, *11*, 5079-5085.

(10) Bos, A.; Westerterp, K. *Chem. Eng. Proc.* **1993**, *32*, 1-7.

(11) Cheung, T.-T.; Johnson, M.; Brown, S.; Zisman, S.; Kimble, J. US Patent 5,510,550, **1996**.

(12) Blankenship, S.; Voight, R.; Perkins, J.; Fried Jr., J. US Patent 6,509,292 B1, **2003**.

(13) Studt, F.; Abild-Pedersen, F.; Bligaard, T.; Sorensen, R.; Christensen, C.; Nørskov, J. *Angew. Chem. Int. Ed.* **2008**, *47*, 9299-9302.

(14) Jin, Y.; Datye, A.; Rightor, E.; Gulotty, R.; Waterman, W.; Smith, M.; Holbrook, M.; Maj, J.; Blackson, J. *J. Catal.* **2001**, *203*, 292-306.

(15) Jones, L. C.; Buras, Z.; Gordon, M. J. *J. Phys. Chem. C* **2012**, *116*, 12982-12988.

(16) Durussel, P.; Feschotte, P. *J. Alloy. Comp.* **1996**, *239*, 226-230.

(17) Calvo, F.; Cottancin, E.; Broyer, M. *Phys. Rev. B* **2008**, *77*, 121406-1-4.

(18) Studt, F.; Abild-Pdersen, F.; Bligaard, T.; Sørensen, R. Z.; Christensen, C. H.; Nørskov, J. K. *Science* **2008**, *320*, 1320-1322.

(19) Song, H.; Rioux, R. M.; Hoefelmeyer, J. D.; Komor, R.; Niesz, K.; Grass, M.; Yang, P.; Somorjai, G. A. *J. Am. Chem. Soc.* **2006**, *128*, 3027-3037.

(20) Grass, M.; Yue, Y.; Habas, S.; Rioux, R.; Teall, C.; Yang, P.; Somorjai, G. A. *J. Phys. Chem. C* **2008**, *112*, 4797-4804.

(21) Bond, G. C.; Wells, P. B. *J. Catal.* **1965**, *4*, 211-219.

(22) Tang, D. C.; Hwang, K. S.; Salmeron, M.; Somorjai, G. A. *J. Phys. Chem. B* **2004**, *108*, 13300-13306.

(23) Lundwall, M. J.; McClure, S. M.; Goodman, D. W. *J. Phys. Chem. C* **2010**, *114*, 7904-7912.

(24) Rodriguez, J. A.; Truong, C. M.; Goodman, D. W. *Surf. Sci.* **1992**, *271*, L331-L337.

(25) Toolenaar, F. J. C. M.; Stoop, F.; Ponec, V. *J. Catal.* **1983**, *82*, 1-12.

(26) Shigeishi, R. A.; King, D. A. *Surf. Sci.* **1976**, *58*, 379-396.

(27) Streber, R.; Trankenschuh, B.; Schock, J.; Papp, C.; Steinruck, H.-P.; McEwen, J.-S.; Gaspard, P.; Denecke, R. *J. Chem. Phys*. **2009**, *131*, 064702-1-9.

(28) Schaal, M. T.; Pickerell, A. C.; Williams, C. T.; Monnier, J. R. *J. Catal.* **2008**, *254*, 131-143.

(29) Röder, H.; Schuster, R.; Brune, H.; Kern, K. *Phys. Rev. Lett.* **1993**, *71*, 2086-2089.

(30) Rodriguez, J. A.; Kuhn, M. *J. Phys. Chem.* **1994**, *98*, 11251-11255.

(31) Schaal, M. T.; Hyman, M. P.; Rangan, M.; Ma, S.; Williams, C. T.; Monnier, J. R.; Medlin, J. W. *Surf. Sci.* **2009**, *603*, 690-696.

(32) Naumovets, A. G.; Vedula, Y. S. *Surf. Sci. Rep.* **1985**, *4*, 365-434.

(33) Tao, F.; Dag, S.; Wang, L.-W.; Liu, Z.; Butcher, D.; Bluhm, H.; Salmeron, M.; Somorjai, G. *Science* **2010**, *327*, 850-853.

(34) Bond, G. C.; Metal-catalysed reactions of hydrocarbons: metals and alloys, New York: Springer Science **2005**.

Chapter 4

Local compositions and structures of a heterogeneous analogue to Periana's homogeneous Pt catalyst

---

Adapted from Nature Materials submission:

Mario Soorholtz,[a] Louis C. Jones,[c] Dominik Samuelis,[b] Claudia Weidenthaler,[a] Robin J. White,[d] Maria-Magdalena Titirici,[d] Dave Cullen,[e] Tobias Zimmermann,[a] Markus Antonietti,[d] Joachim Maier,[b] Regina Palkovits,[a,f] Bradley F. Chmelka,[c] and Ferdi Schüth[a]

[a] *Max-Plank-Institut für Kohlenforschung, Mülheim an der Ruhr, D-45470, Germany*

[b] *Max Planck Institute for Solid State Research, Stuttgart, D-70569, Germany*

[c] *University of California, Santa Barbara, California 93106-5080, USA*

[d] *Max Planck Institute of Colloids and Interfaces, Postdam, D-14476, Germany*

[e] *Oak Ridge National Laboratory, Oak Ridge, Tennessee 37831, USA*

[f] *RWTH Aachen University, Aachen, D-52074, Germany*

Abstract

The local compositions, structures, and uniformity of active Pt species within a carbon-based covalent triazine framework functionalized with molecular $PtCl_2$ species (Pt-CTF) were characterized in detail using several advanced techniques to obtain deeper insight into the Pt environment and its interaction with the organic support material. The material of interest mimics Periana's catalyst ($Pt(bpym)Cl_2$), which is a well-known and highly active catalyst for the selective oxidation of methane *via* C-H activation. The results provide unprecedented insights into the nature of molecular Pt sites in a heterogeneous catalyst, specifically, a solid-state analogue of Periana's catalyst that promotes stable activity for the partial oxidation of methane.

4.1. Introduction

Heterogeneous solids functionalized with molecular complexes have the potential to bridge the gap between homogeneous and heterogeneous catalysis by combining the advantages of both facile catalyst separation and recycling with a relatively uniform distribution of well-defined active sites.[1-3] In contrast, commonly used solid catalysts, such as supported metal particles or metal oxides, typically exhibit a heterogeneous distribution of active sites with diverse energetics and reactivity.[4] By comparison, systematic modification of well-defined active sites by grafting transition metal complexes can facilitate understanding of complex structure-activity relationships and, in conjunction with computational methods, analyses of catalytic mechanisms. Moreover, the catalytic performance can be further optimized by chemically modifying molecular catalysts, which in turn can inspire the synthesis of a solid counterpart. However, the clear advantages of well-defined molecular complexes are always accompanied by the challenge of identifying and characterizing, on the atomic scale, the catalytically active sites and their environments within the solid scaffold. Thomas *et al.* identified various characterization techniques for solids that are suitable for acquiring valuable information on an atomic scale,[5, 6] although subtle changes in the interactions between active centers and different support materials have been difficult to distinguish.

Over the past decades, a number of synthesis strategies have been developed for molecular catalysts on solid supports, and crucial intermediate steps of reactivity have been characterized. Maschmeyer *et al.*[7], Jarupatrakorn *et al.*[8], Thomas *et al.*[6] and Corma[9] reported a synthesis that selectively modified the surface of ordered silica materials with single transition metal atoms in a defined environment. Isomorphous substitution of four-coordinate Si^{IV} in zeolite frameworks (*e.g.*, in ZSM-5) with Ti^{IV} results in a microporous open-structure with isolated Ti centers.[10] This material, known as TS-1, is an exceptionally active solid oxidation catalyst that has recently entered industrial application, emphasizing the high technological importance. In contrast to inorganic supports, porous organic polymers and carbons have received relatively little attention in the literature. Corma *et al.*[11] and McNamara *et al.*[12] reviewed several approaches to heterogenize molecular complexes within polymeric scaffolds. However, characterization methods used to probe functionalized carbon-based frameworks are often insufficient to establish the presence of defined, stable, and homogeneous single active sites.

Here, we establish the local compositions, structures, and uniformity of active Pt species within a carbon-based solid molecular catalyst. The material of interest mimicks the dichloro-2,2'-bipyrimidine-platinum(II) molecular catalyst ($Pt(bpym)Cl_2$, Periana's catalyst[13,14]), which is a well-known and highly active catalyst for the selective oxidation of methane *via* C-H activation. The solid catalyst is synthesized via coordination of a Pt^{II} species to an amorphous, nitrogen-rich carbon scaffold, referred to as a Covalent Triazine Framework (CTF), the building units of which resemble the 2,2'-bipyrimidine ligand of its molecular counterpart (Fig. 4.1). Microporous CTF has previously been reported by Kuhn *et al.*, who used the trimerization of an aromatic dinitrile under ionothermal conditions at temperatures of up to 600 °C.[15, 16] For the synthesis of the supported molecular catalyst, Pt is grafted to the CTF via a simple coordination approach in water at room temperature using K_2PtCl_4 as metal precursor. Applicability and durability in the selective oxidation of methane under extremely harsh reaction conditions (215 °C, 90 bar CH_4, oleum (20 wt% SO_3)) were demonstrated in a previous communication.[17] In particular, measured turnover numbers (TONs) were stable for at least six subsequent runs, and no leaching of Pt species was observed. In a subsequent study, reaction rates of Pt-CTF proved to be somewhat less active (TOF = $174\ h^{-1}$) than its molecular counterpart $Pt(bpym)Cl_2$ (TOF = $912\ h^{-1}$)[18], a commonly observed tradeoff for the added benefits of heterogenized catalysts. While the catalytic performance of the solid Pt-CTF was found to be very promising, the nature of the platinum sites and their correspondence with the homogeneous (molecular) Periana catalyst have remained unclear.

Herein, we characterize the Pt-CTF catalyst in detail using several advanced techniques to obtain deeper insight into the Pt environment and its interaction with the organic support material. Aberration-corrected transmission electron microscopy (TEM), solid-state ^{195}Pt nuclear magnetic resonance (NMR), X-ray photoelectron spectroscopy (XPS), and X-ray absorption spectroscopy (XAS) with structural modeling yield detailed information regarding the local environments of atomic Pt species in Pt-CTF. The results provide unprecedented insights into the nature of molecular Pt sites in a heterogeneous catalyst, specifically a solid-state analogue of Periana's catalyst that promotes activity for the partial oxidation of methane.

4.2. Experimental Section

Structural similarities and differences between Pt-CTF and Pt(bpym)Cl_2 catalysts were established by measuring and analyzing directly their respective Pt environments by solid-state ^{195}Pt NMR. Specifically, solid-state ^{195}Pt WURST-CPMG NMR spectra were acquired at 7.06 T on a Bruker AVANCE NMR spectrometer operating at 300.07 and 64.49 MHz for ^{1}H and ^{195}Pt, respectively, with parameters optimized according to previous work.[28,29] WURST-CPMG pulses of 50 μs (~2 MHz) were applied at center frequencies of 64.72 and 64.28 MHz using

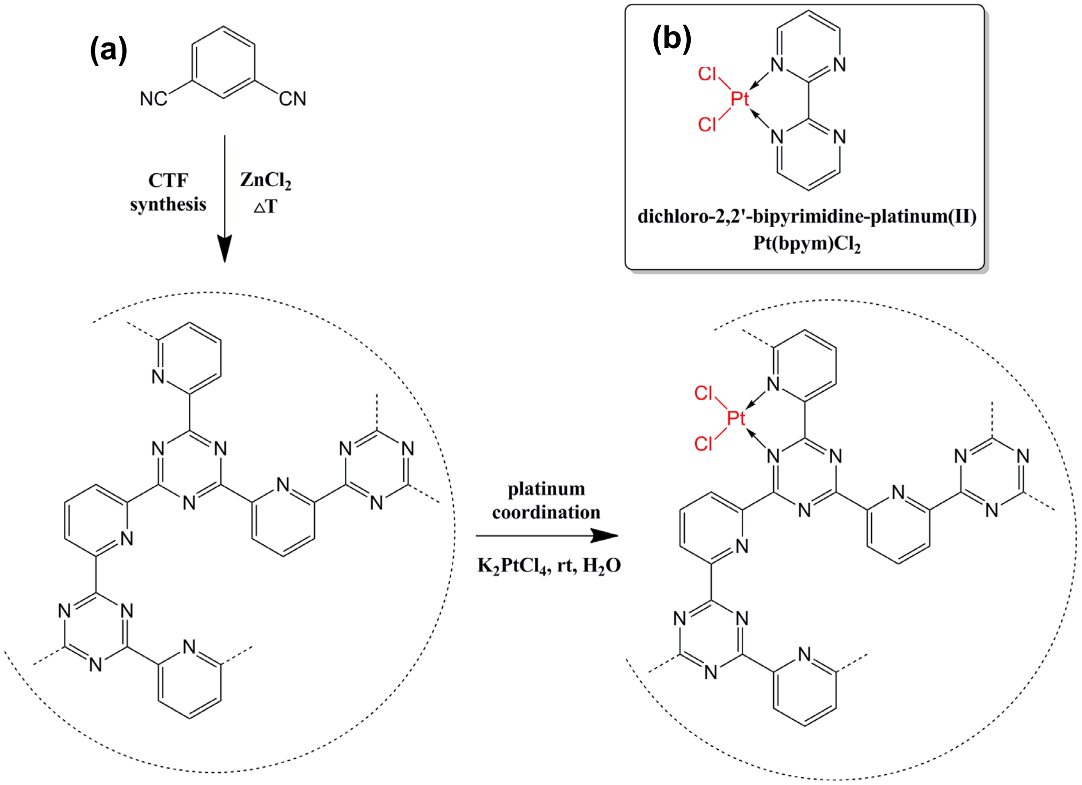

Figure 4.1. (a) Schematic synthesis procedure for Pt-CTF**.** An aromatic dinitrile (2,6-dicyanopyridine) is converted via ionothermal polymerization in molten $ZnCl_2$ (step 1: 400 °C, 40 h; step 2: 600 °C, 40 h) into an extended nitrogen-rich carbon scaffold (covalent triazine framework). The illustrated structure of CTF is idealized since the high polymerization temperatures lead to a disordered arrangement of the carbon scaffold. Periana's molecular catalyst ($Pt(bpym)Cl_2$) is shown in (b).

forward and reverse frequency sweeps to compensate for transverse relaxation of ^{195}Pt magnetization during the sweeps. An acquisition time of 80 μs was used to measure the free induction decays of each subsequent CPMG loop (12 total) with recycle delays of 0.5 to 2 s, which were chosen to maximize signal sensitivity. The absolute value of the Fourier transformed spectra for the two center frequencies were co-added to produce the observed ^{195}Pt spikelet patterns with a span of >1 MHz. Lineshape analyses were performed using the program "*dmfit*" based on interpolated skyline projections of each characteristic CPMG spikelet pattern.[30]

EXAFS, XANES, XPS, and electron microscopy results were provided by Dr. M. Soorholtz and Professor Ferdi Schüth. (MPI-Muelheim, Germany).

4.3. Results and Discussion

4.3.1. Direct characterization of molecular Pt environments

Direct measurements of molecular similarities and differences between Pt sites in Pt-CTF and Pt(bpym)Cl$_2$ were clearly established using advanced solid-state ^{195}Pt NMR spectroscopy, which is sensitive to changes in local Pt valence and conduction electron environments.[22, 23] Insights into the molecular environments of ^{195}Pt moieties in Pt-CTF can be made by analyzing the static solid-state ^{195}Pt WURST-CPMG NMR spikelet spectrum shown in Figure 4.2, which yields direct molecular level insights on the types, relative populations, and distributions of ^{195}Pt atoms in the materials. The ultrabroad linewidths (~10,000 ppm) of ^{195}Pt NMR signals render line-narrowing methods (e.g., magic-angle spinning) ineffective, and instead, require specialized frequency-sweep techniques to effectively excite the entire ^{195}Pt NMR spectra.[24] A series of signal echoes is obtained, which is Fourier-transformed and squared to produce a series of spikelets, with an intensity manifold that reflects the overall lineshape of a static ^{195}Pt NMR spectrum.

Although lacking long-range crystallinity, the Pt-CTF catalyst exhibits clear evidence of local structural order that is analogous to the Pt(bpym)Cl_2 catalyst. The ^{195}Pt NMR spectra of Pt-CTF in Figure 4.2a can be fit (Fig. 4.2b) with contributions from two types of ^{195}Pt sites, one relatively ordered and another that is disordered. The broad asymmetric lineshape (blue) is characteristic of a chemical shift anisotropy (CSA)[24] powder pattern associated with diamagnetic ^{195}Pt species.[25] The axial symmetry of the ^{195}Pt CSA lineshape provides information on local bonding at the ^{195}Pt site, as characterized by the principal axes components of the ^{195}Pt chemical shift tensor (δ_{xx}, δ_{yy}, δ_{zz}), the isotropic ^{195}Pt chemical shift ($\delta_{iso}=(\delta_{xx}+\delta_{yy}+\delta_{zz})/3$), and anisotropy parameter ($\eta=(\delta_{yy}-\delta_{xx})/(\delta_{zz}-\delta_{iso})$). The respective fits include an axially symmetric ($\eta=0.06$) lineshape (inset site I) from a relatively uniform and predominant (ca. 85%) type of ^{195}Pt site with CSA parameters (Table 4.1) that reflect approximately square-planar C_{2v} symmetry of a Pt-N_xCl_y complex, similar to that of Pt(bpym)Cl_2. Both the asymmetry parameter ($\eta=0.06$) and the δ_{xx} (-4900 ppm) and δ_{yy} (-4500 ppm) values of the ^{195}Pt chemical shift tensor are comparable to the CSA parameters ($\eta = 0.04$, δ_{xx}= -4800 ppm, δ_{yy}= -4600 ppm) for one of the two distinct sites within crystalline Pt(bpym)Cl_2 (Fig. 4.3, Table 4.2).[26] This site corresponds to one of two square-planar stacking motifs in a molecularly ordered Pt(bpym)Cl_2 solid (Fig. 4.3b, site 1), whereby π-π stacking of bipyrimidine rings promote undistorted square-planar Pt complexes. As ^{195}Pt is known to have an extremely broad chemical shift range, such similar tensor values indicate that the locally ordered ^{195}Pt environments in Pt-CTF are similar to those of crystalline Pt(bpym)Cl_2, albeit

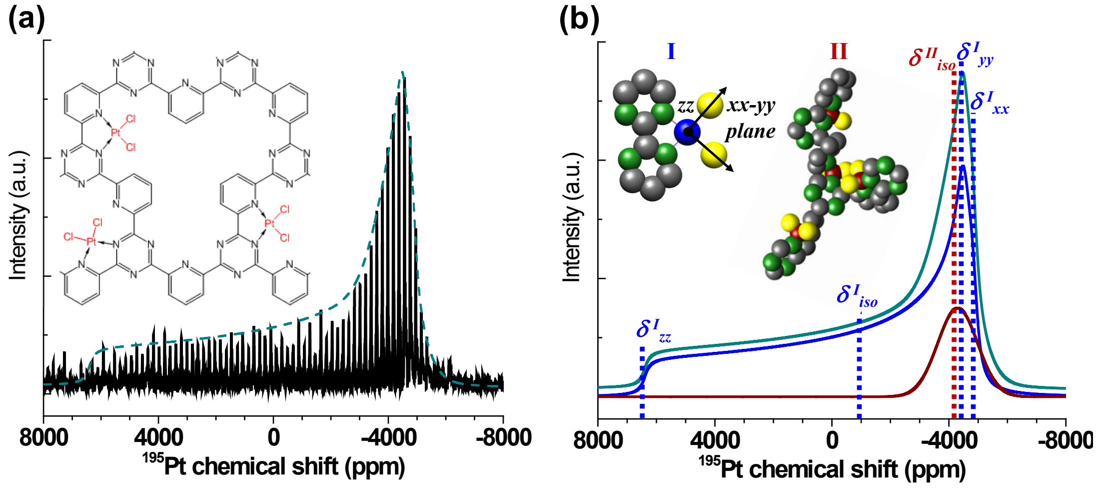

Figure 4.2 (a) Static solid-state ^{195}Pt WURST-CPMG NMR spectrum (black) of the Pt-CTF (covalent triazine framework) catalyst. A summed lineshape fit is shown (dashed green), comprised of (b) spectral components from two types of ^{195}Pt sites: a locally ordered axially symmetric ^{195}Pt site (85%) and relatively disordered ^{195}Pt moieties (15%). Proposed local structures of the two types of ^{195}Pt sites (I, red; II, blue) are shown as insets above each spectrum, with nitrogen atoms (green), carbon atoms (grey), and chlorine atoms (yellow). Chemical shift parameters (δ_{xx}, δ_{yy}, δ_{zz}, and δ_{iso}) are orientation-specific descriptors of the local ^{195}Pt bonding environments and are indicated for each lineshape in (b), with values tabulated in Supporting Information (Table 4.1). Axes shown for site I indicate the directions of the principal components (δ_{xx}, δ_{yy}, δ_{zz}) of the chemical shift tensor.

Table 4.1. Chemical Shift Parameters for (CTF)PtCl$_2$

Chemical Shift Tensor Parameters [ppm]				**Chemical Shift Anisotropy Parameters**			
Component	δ_{xx}	δ_{yy}	δ_{zz}	δ_{iso} [ppm]	$\Delta\sigma/\Delta\delta$ [ppm]	η	% Area
I	-4900	-4500	6400	-1000	7400	0.06	85.0
II	NA	NA	NA	-4300	1600	NA	15.0

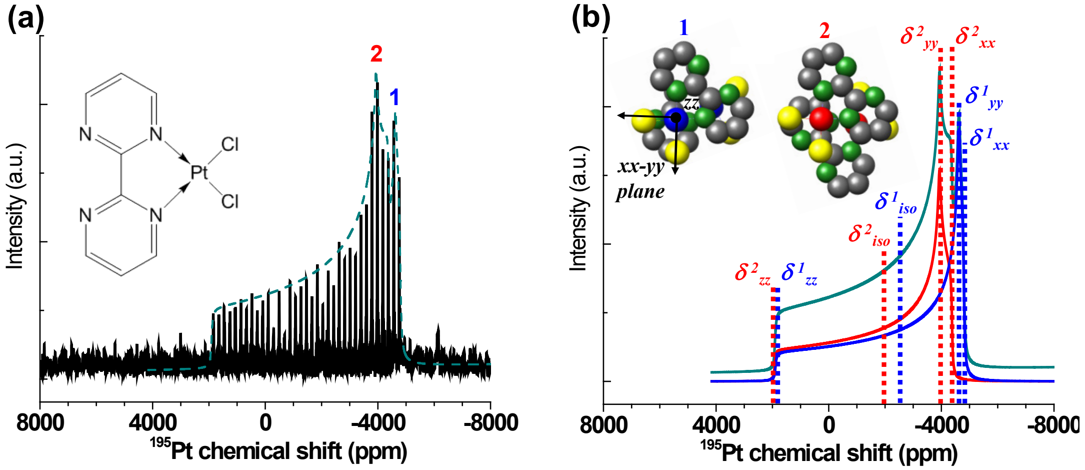

Figure 4.3. (a) Static solid-state ^{195}Pt WURST-CPMG NMR spectrum (black) of the Pt(bpym)Cl$_2$ catalyst. A summed lineshape fit is shown (dashed green), comprised of (b) spectral components from two types of ^{195}Pt sites: a locally ordered π–π stacked axially symmetric ^{195}Pt site (site 1, 50%) and another locally ordered ^{195}Pt site (site 2, 50%) that is not π–π stacked. Proposed local structures of the two types of ^{195}Pt sites (1, blue; 2, red) are shown as insets above each spectrum, with nitrogen atoms (green), carbon atoms (grey), and chlorine atoms (yellow). Chemical shift parameters (δ_{xx}, δ_{yy}, δ_{zz}, and δ_{iso}) are orientation-specific descriptors of the local ^{195}Pt bonding environments and are indicated for each lineshape in (b), with values tabulated in Supporting Information (Table S1). Axes shown for site 1 indicate the directions of the principal components (δ_{xx}, δ_{yy}, δ_{zz}) of the chemical shift tensor.

Table 4.2. Chemical Shift Parameters for (bpym)PtCl$_2$

Chemical Shift Tensor Parameters [ppm]				**Chemical Shift Anisotropy Parameters**			
Component	δ_{xx}	δ_{yy}	δ_{zz}	δ_{iso} [ppm]	$\Delta\sigma$ [ppm]	η	% Area
1	-4400	-3900	1900	-2100	4100	0.11	49.9
2	-4800	-4600	1900	-2500	4400	0.04	50.1

dispersed within the CTF network. Consequently, the solid-state ^{195}Pt WURST-CPMG NMR results above indicate similar coordination geometries and local environments around Pt in both Pt-CTF and one site in Pt(bpym)Cl_2.

Nevertheless, there are also differences between the ^{195}Pt NMR spectra of the solid Pt-CTF catalyst and the crystalline Pt(bpym)Cl_2 solid. In particular, the z-components of their chemical shift tensors (δ_{zz}) are significantly different, 6400 ppm versus 1900 ppm, respectively (Tables 4.1 and 4.2). The δ_{zz} component, which is sensitive to interactions normal to the square-plane of the ^{195}Pt complexes, is displaced to higher frequency (larger ppm), likely due to ring currents in the extended π–electron networks of the CTF. Additionally, there is evidence of a modest fraction of locally disordered ^{195}Pt species that are accounted for by a Gaussian distribution of ^{195}Pt signal intensity centered at -4500 ppm (Fig. 4.2b, inset site II). Such intensity is consistent with a minority of Pt sites (ca. 15%) that possess a distribution of local ^{195}Pt structures that are distorted from square-planarity within the branched and disordered covalent triazine framework that produces a distribution of nitrogenous coordination sites. Furthermore, both types of ^{195}Pt sites in the solid catalyst exhibit significantly shorter ^{195}Pt spin-lattice (T_1) relaxation times (order of 0.1 s) than those for bulk crystalline Pt(bpym)Cl_2 (order of 1 s). The shorter T_1 values are consistent with the lack of long-range molecular order in the CTF material, as established by the absence of wide-angle scattering reflections in the XRD pattern of the solid Pt-CTF catalyst. It is reasonable to link these subtle spectroscopic details, which suggest an alteration of Pt atom accessibility and deviations from ideal square-planarity, to differences in the inherent reactivity of the square-planar Pt complexes in the covalent triazine framework as compared to Pt(bpym)Cl_2.

4.3.2. Structure of Pt sites

Using a square-planar geometry model, which was established for Pt complexes in Pt-CTF and Pt(bpym)Cl_2 using solid-state ^{195}Pt NMR, the coordination and bond lengths for Pt species in Pt-CTF and Pt(bpym)Cl_2 were established to have a high degree of molecular similarity using EXAFS and XANES. EXAFS provides reliable data on average short-range structure of the Pt-CTF networks allowing the determination of possible Pt coordination motifs within the amorphous carbon scaffold. Based upon solid-state Pt NMR results, the ordered square-planar Pt moiety accounting for ~85% of the total signal is expected to be the site to which EXAFS will be most sensitive. By comparison, XANES yields information on average Pt concentration and on the average electron density for different Pt sites (Table 4.3). The interpretation of the EXAFS region was supported by fitting with a theoretical structural model of Pt(bpym)Cl_2, the postulated molecular counterpart of Pt-CTF (Fig. 4.1). Due to the short-range sensitivity, ~3-4 coordination shells around the Pt atoms, good agreement between measured EXAFS spectra and theory would be expected for Pt-CTF structures that have the basic coordination motifs of the Pt(bpym)Cl_2 catalyst, especially for a first-coordination shell comprising 2 Cl- and 2 N-ligands.

The structural model for Pt(bpym)Cl_2 (Fig. 4.4a) exhibits similar atomic distances for Pt-N1, Pt-C4, Pt-C1, and Pt-Cl, which render a complex first-coordination shell around the transition metal atom (Fig. 4.4b, blue curve). Accordingly, the Fourier transformed $\chi(k)$ function of the measured Pt-CTF shows a broad overlapping signal for the first coordination shell (Fig. 4.4b, red curve). EXAFS fits of the as-made Pt-CTF samples with a structural model based on Pt(bpym)Cl_2 illustrates that all characteristics of the measured spectrum can be reproduced, an indication that the mean local environment(s) of Pt is similar in both cases. All interatomic distances agree well with the Pt(bpym)Cl_2 reference, with consistently ~3-4% shorter distances than for the model structure. Within the detection limits of 5-10%, no evidence for other ordered Pt coordination motifs could be found within Pt-CTF. Large variances (Debye-Waller factors σ^2), especially for higher coordination shells, suggest that CTF exhibits a non-ordered structure with varying Pt coordination, geometries, and distances between Pt sites and next-nearest neighbor carbon atoms within CTF, consistent with a minority of locally disordered Pt sites (~15%) found using solid-state ^{195}Pt NMR. Stronger attenuation of multiple scattering paths, compared to the Pt(bpym)Cl_2 molecular model, indicates a deviation from a fully planar structure. However, it should be noted that the Pt-Cl (and within error margins, the Pt-N1) bonds exhibit relatively small variances that can be explained by thermal motion, which suggests structural disorder is limited to the CTF network. In fact, the first-coordination shell closely resembles the model Pt(bpym)Cl_2 coordination motif. The non-ordered structure of

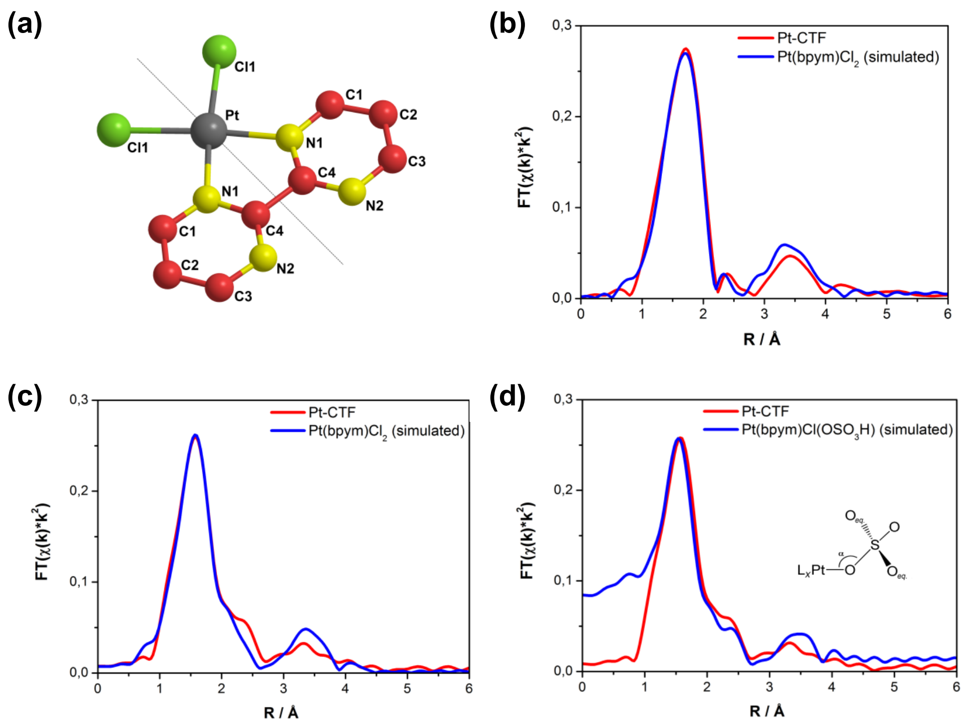

Figure 4.4. Extended X-ray absorption fine structure analysis. (a) Structural model of Pt(bpym)Cl$_2$ taken as a reference, using Cartesian coordinates from Xu *et al.*[19]; (b) Fourier transformed χ(*k*) functions of as-made Pt-CTF and the fitted theoretical Pt(bpym)Cl$_2$ model. Details on fit parameters are given in the Supporting Information; (c) Fourier transformed χ(*k*) functions of Pt-CTF after catalyst use under reaction conditions (2.5 h, 215°C, oleum (20 wt.% SO_3), 90 bar CH_4) and the Pt(bpym)Cl$_2$ model structure; (d) Fourier transformed χ(*k*) functions of Pt-CTF after catalyst use under reaction conditions (2.5 h, 215 °C, oleum (20 wt% SO_3), 90 bar CH_4) and Pt(bpym)Cl(OSO$_3$H) model structure (inset). Results courtesy of Dr. M. Soorholtz, MPI-Muelheim, Germany.

CTF was also established by the solid-state ^{195}Pt NMR results, as well as supplemental XRD results. Verification of bidentate Pt coordination required additional measurements of Pt-CTF samples with various Pt contents, which showed that all spectra exhibit identical features, indicating macroscopically homogeneous Pt coordination within CTF at higher Pt contents.

Structural changes during methane oxidation in hot sulfuric acid were established by *ex-situ* EXAFS characterization of a Pt-CTF catalyst that had been exposed to reaction conditions (2.5 h, 215°C, oleum (20 wt.% SO_3), 90 bar CH_4)**.** A clearly visible shoulder at ~2.3 Å (Fig. 4.4c,d, red curve) is not accounted for by the Pt(bpym)Cl_2 structural model. Additionally, EXAFS fit parameters give much higher S02 values >0.92, which are not typical for carbon framework samples, indicating that the mean Pt coordination environment was altered by the reaction conditions. Moreover, the σ^2 values are an order of magnitude higher than for the previous fits, an additional indication that the local environment(s) of Pt atoms were altered during catalytic reaction. For the homogeneous catalyst, Kua *et al.*[21] postulated that Pt(bpym)Cl_2 undergoes ligand exchange in sulfuric acid, where one chlorine ligand is substituted with bisulfate, accompanied by release of hydrochloric acid. Accordingly, we modified our structural model by replacing a chlorine atom with a bisulfate group to test this hypothesis for the solid analogue Pt-CTF. An overlay of Fourier-transformed $\chi(k)$ functions for the Pt(bpym)Cl(OSO_3H) model and for Pt-CTF (Fig. 4.4d, blue and red curves, respectively) shows that the signal at ~2.3 Å can be accounted for by this modified structural model. A refinement of first-coordination-shell atoms consistently yields a ratio of N:Cl:O of approximately 2:1:1 (+/- 0.5) for a set of four Pt-CTF catalysts evaluated after exposure to identical reaction conditions. Thus, the EXAFS data suggest that ligand exchange occurs at the transition metal center within Pt-CTF, analogous to its molecular counterpart Pt(bpym)Cl_2.

Changes in mean electron density and oxidation state at the Pt sites was investigated before and after catalysis using XANES. As-made and reacted samples of Pt-CTF were compared with respect to their white line positions in the XANES region of the X-ray absorption spectra (Table 4.3). The white line of Pt-CTF shifted by 0.58 eV to higher binding energies after the catalyst had been tested under reaction conditions, an indication of a decrease in the electron density at the Pt atom that is consistent with ligand substitution by bisulfate anions, which are more electronegative than chlorine anions. The X-ray absorption spectroscopy analysis indicates a high degree of similarity between Pt environments in Pt-CTF and the coordination motif of Pt(bpym)Cl_2. Additionally, Pt-CTF undergoes structural changes during use in catalysis that correlate with intermediates postulated for its molecular counterpart. While these indications are strong, corroborations by other techniques that are more sensitive to changes in electronic structure would provide further insight into differences in reactivity.

Table 4.3. White line positions in XANES region for Pt-CTF before and after use in catalysis and corresponding references[a]

description		*white-line-position [eV]*	*white-line-position after use in catalysis [eV]*	*difference [eV]*
reference	K_2PtCl_4	11565.46	-	-
reference	$Pt(bpym)Cl_2$	11566.47	-	-
reference	$PtCl_4$	11567.45	-	-
	Pt-CTF	11566.64	11567.22	0.58

[a] Energies of the white line center in the XANES spectra were determined by peak-fitting a Gaussian curve for the white line on top of an arctan curve representing the absorption edge. Just as for the XANES edge shift, chemical shift rules also apply to the white line. Due to screening effects caused by the change in electron density, the center of the white line is expected to shift to higher energy with increasing effective oxidation state of the Pt atom. Results courtesy of Dr. M. Soorholtz, MPI-Muelheim, Germany.

4.3.3. Surface Pt species in Pt-CTF and $Pt(bpym)Cl_2$

Platinum interactions with surface pyridine species of the CTF support were established by XPS analyses of the N 1s core level electrons. Coordinative modification of CTF or the molecular 2,2'-biyrimidine ligand with a Pt^{II} species significantly change the electron density at the pyridinic nitrogen sites, as well as their corresponding binding energies. Figures 4.5a,b show the XPS N 1s spectra for

Pt-modified and unmodified bpym ligands. For 2,2'-bipyrimidine, a single peak at a binding energy of 398.1 eV is observed, indicating the presence of pyridinic nitrogen species. In contrast, two peaks at 398.0 eV and 399.1 eV are observed for Pt(bpym)Cl_2 with nearly identical intensities. The shift to higher binding energies is a consequence of interactions between valence electrons of the coordinating nitrogen atoms and $(PtCl_2)^{2+}$, and thus, an indication for interactions with pyridinic nitrogen species. For the CTF, more complex behavior is observed (Fig. 4.5c), associated with the disordered polymer structure. Deconvolution of XPS N 1s spectra indicates the presence of three different nitrogen species with different binding energies: pyridine (398.1 eV), pyrrole/pyridone (399.7 eV) and quaternary (401.0 eV) nitrogen species. At the high polymerization temperature used (600 °C), some carbonization also occurs, leading to the formation of additional nitrogen species with higher binding energies, in contrast to the exclusive presence of pyridinic nitrogen moieties in the idealized structure. This behavior is commonly observed and well-known for thermally treated nitrogen-containing carbons.[27] As the EXAFS data also suggest, the presence of 2,2'-bipyridine-like coordination sites in CTF can be considered to be intermediate between polymer and carbonized networks that possess the combined chemical properties/structures of both types of materials. Analogous to Pt(bpym)Cl_2, modification of CTF with Pt^{II} results in an increase of nitrogen species at 399.3 eV, which arises due to a peak shift from 397.9 eV caused by electron donation to $PtCl_2^{2+}$ species. These features indicate an interaction of $(PtCl_2)^{2+}$ with the pyridine sites of CTF, similar to its molecular counterpart Pt(bpym)Cl_2.

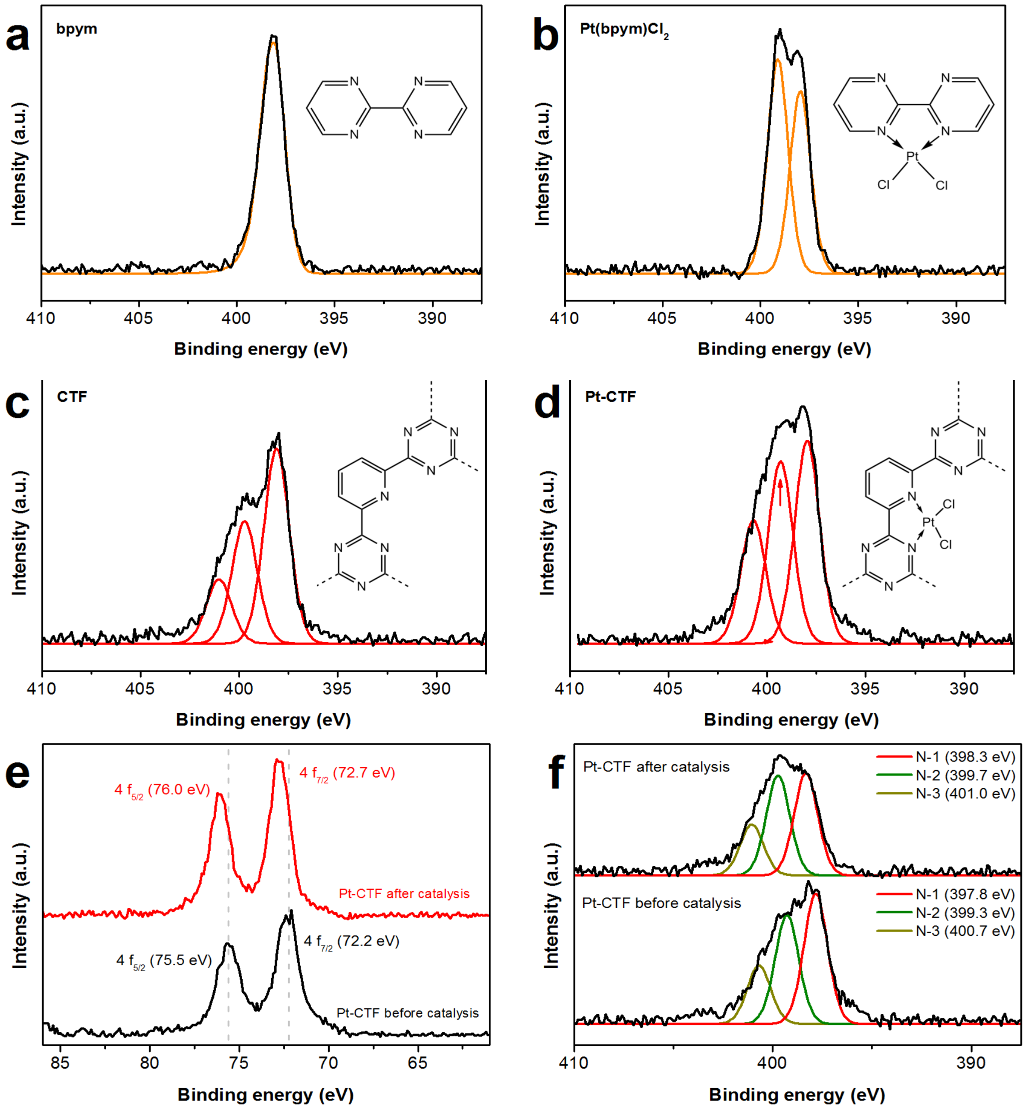

Figure 4.5. N 1s and Pt 4f XPS investigations of Pt interaction with CTF surface species and Pt-CTF properties before and after catalysis. (a,c) N 1s XPS spectra of unmodified and (b,d) Pt-modified 2,2'-byprimidine ligand and CTF, respectively. Comparison between XPS (e) Pt 4f and (f) N 1s spectra for Pt-CTF before and after exposure to reaction conditions for the partial oxidation of methane (2.5 h, 215 °C, oleum (20 wt% SO_3), 90 bar CH_4). Results courtesy of Dr. M. Soorholtz, MPI-Muelheim, Germany.

Moreover, measured binding energies of the Pt 4f core level give clear evidence for the presence of Pt^{II} species within the CTF material (Fig. 4.5e, bottom).

Comparison of XPS Pt 4f spectra for Pt-CTF materials before and after (Fig. 4.5f, top) exposure to reaction conditions provides valuable information about changes in the environment of the active Pt site. It can be observed that the Pt stays in the same oxidation state as before reaction, although a slight shift in the peak position is noted. In detail, the Pt $4f_{7/2}$ peak after reaction is shifted by 0.5 eV to higher binding energies, which is consistent with the observed white-line shift in XANES spectra. Moreover, minor changes in CTF properties can be observed for Pt-CTF after catalysis in the XPS N1s spectra (Fig. 4.5f). In comparison to Pt-CTF before exposure to reaction conditions, slight increases of the population of the N-2 and N-3 species are detected, indicating the presence of a higher fraction of nitrogen species with less electron density. This behavior is attributed to electron-withdrawing surface modifications, promoted by oxidation and/or protonation *via* sulfuric acid under the harsh reaction conditions.

4.3.4. Distribution of Pt atoms within CTF

Besides the insights on the local environments of species in Pt-CTF catalysts, there is a substantial interest in the distribution of Pt species within the covalent triazine framework. Pt atom distributions can be effectively established using high-resolution transmission electron microscopy combined with energy dispersive X-ray (EDX) and z-contrast imaging with high angle annular dark field scanning

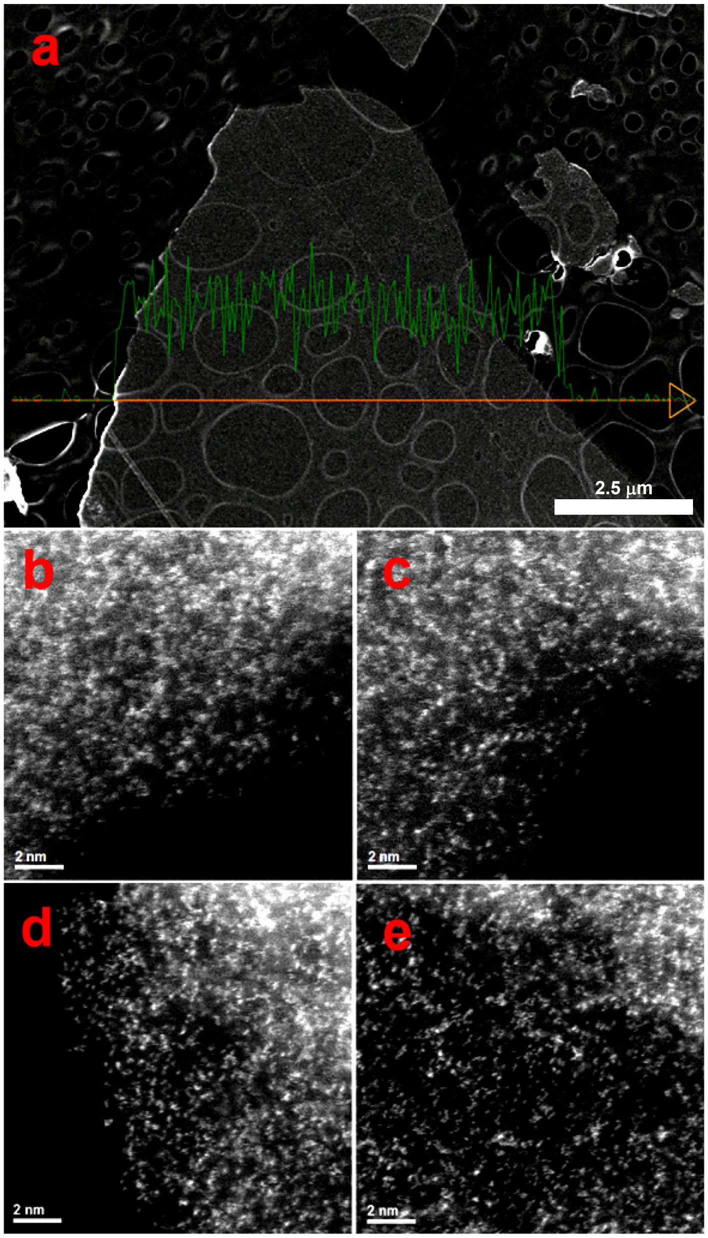

Figure 4.6. Electron microscopy images of 15 wt% Pt-CTF. (a) EDX line-scan of a catalyst cross-section; (b-e), AC-STEM-HAADF images of catalysts (b,c) before (as-made) and (d,e) after exposure to reaction conditions (2.5 h, 215 °C, oleum (20 wt% SO_3), 90 bar CH_4). Results courtesy of Dr. M. Soorholtz, MPI-Muelheim, Germany.

transmission electron microscopy (HAADF-STEM). Figure 4.6a shows an EDX image with a cross-section through a Pt-modified CTF particle, which reveals a homogeneous distribution of Pt across the particle exists. Figure 4.6b show the 15 wt% Pt-CTF material with atomic dispersions of Pt (atomic radius ~ 0.280 nm) within the covalent triazine framework, which is highly unusual for such a catalyst with high contents of noble metal. Moreover, the atomically dispersed Pt sites remain after several catalytic runs under the harsh conditions for the partial oxidation of methane (10 h, 215 °C, 90 bar CH_4, oleum (20 wt% SO_3)). The HAADF-STEM images shown in Figure 4.6c clearly demonstrate that the material maintains the homogeneous distribution of atomic Pt within the cross-linked triazine framework, manifesting the outstanding stability of the heterogeneous Pt-CTF catalyst. Overall, Pt-CTF is established to maintain a high degree of atomic Pt dispersion throughout the material before and after the partial oxidation of methane, suggestive that a molecular Pt active site is responsible for the reactivity of the supported catalyst.

4.4. Conclusions

The work presented here provides deep insight into the material properties of a new heterogeneous carbon-based polymer functionalized with a molecular Pt complex, and specifically, into the interactions between the transition metal and amorphous organic support. Our findings clearly show that Pt^{II} coordinates to pyridine nitrogen sites of the CTF support in a similar local molecular configuration as compared to $Pt(bpym)Cl_2$. Thus, Pt-CTF can be considered as the solid counterpart to the molecular Pt(bpym)Cl_2 catalyst. Investigations of Pt-CTF after reaction suggest similar changes on the molecular level in comparison to Pt(bpym)Cl_2, underlining the successful heterogenization of this catalyst and providing a new and general strategy for synthesizing stable heterogeneous solid catalysts with defined molecular active sites. Extending the presented synthesis approach to transition metals other than Pt that favor coordination to nitrogenous ligands emphasizes the high potential for these carbon based solid catalysts functionalized with molecular complexes.

4.5. Acknowledgements

Solid-state ^{195}Pt NMR experiments were conducted in the Central Facilities of the UCSB Materials Research Laboratory MRSEC Program of the NSF under Award No. DMR-1121053; a member of the NSF-funded Materials Research Facilities Network(www.mrfn.org). Use of the Central Facilities was supported by the U.S. National Science Foundation under Grant No. CHE-1059108. L.C.J thanks the NSF-IOSE-PIRE Program (0968399) and the NSF ConvEne IGERT Program (NSF-DGE 0801627) for fellowship support.

4.6. References

(1) Thomas J.M.; Raja R.; Lewis D.W. *Angewandte Chemie International Edition* **2005**, *44*, 6456.

(2) Copéret C.; Chabanas M.; Petroff Saint-Arroman R.; Basset J.-M. *Angewandte Chemie-International Edition* **2003**, *42*, 156.

(3) Anwander R. Immobilization of Molecular Catalysts. In: Ertl G., Knözinger, H., Schüth, F., Weitkamp, J. (ed). *Handbook of Heterogeneous Catalysis*. Wiley-VCH Verlag GmbH & Co. KGaA: Weinheim, **2008**.

(4) Thomas J. M.; Raja R.; Gai P. L.; Grönbeck H.; Hernández-Garrido J. C. *ChemCatChem* **2010**, *2*, 402.

(5) Thomas J. M. *Microporous and Mesoporous Materials* **2011**, *146*, 3.

(6) Thomas J. M.; Raja R. *Journal of Organometallic Chemistry* **2004**, *689*, 4110.

(7) Maschmeyer T.; Rey F.; Sankar G.; Thomas J. M. *Nature* **1995**, *378*, 159.

(8) Jarupatrakorn J.; Tilley T. D. *Journal of the American Chemical Society* **2002**, *124*, 8380.

(9) Corma A. *Catalysis Reviews: Science & Engineering* **2004**, *46*, 369.

(10) Thomas J. M.; Raja R. *Catalysis Today* **2006**, *117*, 22.

(11) Corma A.; Garcia H. *Topics in Catalysis* **2008**, *48*, 8.

(12) McNamara C.A.; Dixon M. J.; Bradley M. *Chemical Reviews* **2002**, *102*, 3275.

(13) Periana R.A.; Taube D.J.; Gamble S.; Taube H.; Satoh T.; Fujii H. *Science* **1998**, *280*, 560.

(14) Conley B. L.; Tenn W. J.; Young K. J. H.; Ganesh S.; Meier S.; Ziatdinov V. *et al. Methane Functionalization*. Wiley-VCH Verlag GmbH & Co. KGaA, **2006**.

(15) Kuhn P.; Thomas A.; Antonietti M. *Macromolecules* **2009**, *42*, 319.

(16) Kuhn P.; Antonietti M.; Thomas A. *Angewandte Chemie-International Edition* **2008**, *47*, 3450.

(17) Palkovits R.; Antonietti M.; Kuhn P.; Thomas A.; Schüth F. *Angew. Chem. Int. Ed.* **2009**, *48*, 6909.

(18) Soorholtz M.; White R. J.; Zimmermann T.; Titirici M.-M.; Antonietti M.; Palkovits R. *et al. Chemical Communications* **2013**, *49*, 240.

(19) Xu X.; Kua J.; Periana R. A.; Goddard W. A. *Organometallics* **2003**, *22*, 2057.

(20) Ravel B.; Newville M.; ATHENA; ARTEMIS; HEPHAESTUS: data analysis for X-ray absorption spectroscopy using IFEFFIT. *Journal of Synchrotron Radiation* **2005**, *12*, 537.

(21) Kua J.; Xu X.; Periana R. A.; Goddard W. A. *Organometallics* **2001**, *21*, 511.

(22) O’Dell L. A.; Schurko R. W. *Chemical Physics Letters* **2008**, *464*, 97.

(23) MacGregor A. W.; O'Dell L. A.; Schurko R. W. *Journal of Magnetic Resonance* **2011**, *208*, 103.

(24) Lucier, B. E. G.; Reidel, A. R.; Schurko, R. W. *Canadian Journal of Chemistry* **2011**, *89*, 919.

(25) W. Veeman. *Progress in Nuclear Magnetic Resonance Spectroscopy* **1984**, *16*, 193.

(26) Kaim W.; Dogan A.; Wanner M.; Klein A.; Tiritiris I.; Schleid T. *et al. Inorganic Chemistry* **2002**, *41*, 4139.

(27) Arrigo R.; Havecker M.; Schlogl R.; Su D. S. *Chemical Communications* **2008**, *40*, 4891.

(28) O’Dell, L.; Rossini, J. A.; Schurko, R. W. *Chem. Phys. Lett.* **2009**, *468*, 330.

(29) A. MacGregor; O’Dell, L.; Schurko, R. W. *J. Magn. Reson.* **2011**, *208*, 103.

(30) Massiot, D.; Fayon, F.; Capron, M.; King, I.; Le Calve, S.; Alonso, B.; Durand, J. O.; Bujoli, B.; Gan, Z.; Hoatson, G. *Magn. Res. Chem.* **2002**, *40*, 70.

Chapter 5

Measuring distinct surface molecular environments of surface platinum species in bulk and supported Pt oxides and sulfides

---

Adapted from Journal of the American Chemical Society submission:

Louis C. Jones,[a] Michael J. Gordon,[a] Stacey I. Zones,[b] Cong-Yan Chen,[b] Robert J. Saxton,[b] and Bradley F. Chmelka[a]

[a] *Department of Chemical Engineering, University of California, Santa Barbara, Santa Barbara, California 93106-5080, USA*

[b] *Chevron Research and Technology Company, Richmond, California 94802-0627, USA*

Abstract

Using recently advanced solid-state ^{195}Pt NMR resonance methods, unique molecular environments of surface Pt species in Pt-black and supported Pt nanoparticles were established as a function of surface chemistry (i.e., oxide vs. sulfide), nanoparticle size (i.e., 1 um - 0.X nm), and zeolite support interactions (i.e., NaY vs. B-SSZ-33) with Pt loadings as low as 0.5 wt%. Signals indicative of Pt oxides, sulfides, Pt^{2+}, and cluster-support interactions were readily distinguishable and provided clear evidence of differences in local Pt valence electron environments. Sulfidation of supported Pt nanoparticles was shown to selectively diminish interactions between Pt oxide clusters and 12-ring cage interactions in zeolite NaY and B-SSZ-33, while 10-ring cage support interactions remained intact for B-SSZ-33. These newly resolved spectral details provide molecular indications for sulfur tolerance, in addition to the local order and coverage of sulfur on the Pt nanoparticles. With the enhanced bandwidth and sensitivity offered by newly advanced solid-state ^{195}Pt NMR methods, these subtle and previously unresolved molecular features can now be readily correlated with differences in Pt catalytic reactivity.

5.1. Introduction

Measuring distributions of Pt environments in supported nanoparticle systems relies on probing surface Pt species with techniques that are sensitive to changes in local molecular bonding. From a vast array of characterization techniques, it has been well established that Pt surface chemistry,[1] particle size,[2] and particle-support interaction[3] play determining roles in the modification of local bonding environments. However, there are limitations in the ability to distinguish differences in local molecular Pt properties, either due to an inability to probe appropriate length-scales or being insensitive measures of local Pt bonding environments. For example, diffraction methods (XRD) can provide information regarding atom-atom distances of regularly ordered materials, but density functional theory methods are necessary to approximate Pt electronic structure, which is the determining property for molecular bonding.[4] Direct measurements of electronic structure can be made using surface sensitive photoelectron spectroscopy methods (XPS), but only core electrons can be elementally resolved, unlike the valence band structure, which has contributions from all elements within the macroscopic sample volume due to similar and overlapping energies.[5] Pt specific techniques that are more sensitive to local changes in valence and conduction electron structure can overcome experimental limitations by providing the element specificity and energy resolution to observe molecular signatures of local Pt environments.

Advanced solid-state ^{195}Pt nuclear magnetic resonance (NMR) methods have both the element specificity and sensitivity to changes in local bonding environments to be highly informative about the unique molecular environments present within heterogeneous Pt catalysts. The high chemical resolution of NMR is attributed to its sensitivity towards subtle changes in nuclear spin interactions with local valence and conduction electrons, which enables intermolecular and intramolecular moieties to be distinguished from each other.[6] However, while magnetic resonance methods (e.g., multinuclear[7] and imaging[8]) have seen substantial technological advancement and widespread use in the all fields of science, applications to supported Pt nanoparticles have remained limited. Compared to the frequency spread of more ubiquitous ^{1}H and ^{13}C nuclei (~kHz), solid-state ^{195}Pt NMR spectra can span very large radiofrequency bandwidths (~MHz),[6] which provides higher resolution information on the molecular environments of Pt species, but have been impractical to excite and detect with conventional techniques. Previous work has demonstrated that surface Pt environments can be readily distinguished from the bulk interior,[9] but limited excitation of ^{195}Pt NMR frequencies resulted in low resolution data that lacked fine structure details in surface regions of the spectra. Recent methodological advancements (e.g., WURST-CPMG[10]) now allow large frequency bandwidths to be managed, enabling detailed characterization of local ^{195}Pt molecular environments that have been infeasible to characterize.[11] Solid-state WURST-CPMG NMR has been used to characterize ^{195}Pt environments in ordered molecular solids, but have yet to be applied to heterogeneous Pt materials.

Herein, the synthesis, treatments, and characterization of bulk Pt (i.e., Pt-black) and supported Pt nanoparticles (i.e., Pt-NaY, Pt-B-SSZ-33) were carried out to establish distributions of local molecular Pt environments in these materials using solid-state ^{195}Pt WURST-CPMG NMR. The enhanced sensitivity and resolution offered by ^{195}Pt WURST-CPMG NMR enabled novel assignments of spectral details to electronically distinct surface ^{195}Pt environments. The influence of unique surface chemistry (i.e., oxide vs. sulfide), nanoparticle size (i.e., 25 nm - 0.5 nm), and zeolite support interactions (i.e., NaY vs. B-SSZ-33) with Pt loadings as low as 0.5 wt% were readily distinguished. With knowledge of where specific ^{195}Pt environments appear in the NMR spectra, signal deconvolutions were made possible and provided the relative distributions of Pt environments in these materials. Comparisons between oxidized and sulfidized Pt nanoparticles supported on zeolite NaY and B-SSZ-33 revealed that 12-ring cage interactions were diminished upon sulfidization, while 10-ring cage interactions in B-SSZ-33 remained intact. The work provides a general framework with which to investigate local molecular ^{195}Pt environments in a variety of Pt-containing materials, and in particular, for supported Pt nanoparticle catalysts.

5.2. Experimental Section

Oxidized samples of Pt-black (Sigma Aldrich) were treated with O_2 at 120 ^{o}C, while sulfidized samples were treated with H_2 at 120 ^{o}C for 30 min and S_8 at 120 ^{o}C for 1 h. Pt NaY samples were prepared by ion-exchanging $Pt(NH_3)_4Cl_2$ with zeolite NaY at 60 ^{o}C. The resulting powder was washed with NaOH and H_2O several times before drying overnight. Oxidized samples were prepared by flowing O_2 while heating to 400 ^{o}C over a 5 h period. In a separate reactor, sulfidized samples were prepared by first oxidizing, followed by cooling to 298 K, then flowing H_2 while heating to 400 ^{o}C over a 5 h period, and finally exposing S_8 at 120 ^{o}C for 1 h.

Oxidized and sulfidized Pt-SSZ-33 were provided by Dr. Stacey Zones and Dr. CY Chen (Chevron, Richmond, California).

Solid-state ^{195}Pt WURST-CPMG NMR spectra were acquired at 7.06 T on a Bruker AVANCE NMR spectrometer operating at 300.07 and 64.49 MHz for ^{1}H and ^{195}Pt, respectively, with parameters optimized according to previous work.[10,11] WURST-CPMG pulses of 50 μs (~2 MHz) were applied at center frequencies of 64.72 and 64.28 MHz using forward and reverse frequency sweeps to compensate for transverse relaxation of ^{195}Pt magnetization during the sweeps.. An acquisition time of 80 μs was used to measure the free induction decays of each subsequent CPMG loop (12 total) with recycle delays of 0.5 s. Fourier transformed spectra for the two center frequencies were co-added after a magnitude calculation to produce the observed ^{195}Pt spikelet patterns with a span of >1 MHz. Lineshapes were constructed from interpolated skyline projections (spikelet integration) of each CPMG spikelet pattern.

X-ray photoelectron spectra (XPS) were measured using a Kratos Axis Ultra system with a monochromated Al K_{α} source (1486.6 eV, 225 W). An electron flood gun was used for charge neutralization to compensate for the non-conducting samples. All samples were referenced to surface carbonaceous species (284.7 eV).

X-ray diffraction (XRD) patterns were measured using a Philips X'Pert MPD with a 3kW Cu K_{α} (1.5405 Å) X-ray source.

5.3. Results and Discussion

5.3.1. Surface Chemistry of Pt-black

The influence of surface chemistry on local molecular ^{195}Pt environments was investigated by probing oxidized and sulfidized Pt-black surfaces. It is well established that oxidized[12-15] and sulfidized[16-20] Pt surfaces have distinct reactivity towards H_2, O_2, CO, and various hydrocarbons. However, molecular origins of unique Pt reactivity are difficult to establish using methods that are insensitive to changes in local Pt valence electron environments. The relatively high surface-area of a bulk Pt compound such as Pt-black (21 m^2/g) provides adequate sensitivity to probe surface ^{195}Pt environments without the influence of a support. An XRD comparison for surface oxidized and sulfidized Pt-black (Fig. 5.1a,d) show similar patterns of FCC metallic Pt, with line narrowing upon sulfidation that is consistent with increased crystallite size due to sintering during treatment. Pt 4*f* XPS spectra (Fig. 5.1b,e) show nearly identical lineshapes that are composed of overlapping contributions from Pt^0 and Pt^{2+} species, which indicate the presence of $PtO_{1.3}$ and $PtS_{0.5}$ upon deconvolution and integration of XPS survey spectra. While changes in both stoichiometry and particle size can be observed, there are no indications of differences in surface Pt electronic environments using XRD and XPS. In stark contrast, a solid-state ^{195}Pt WURST-CPMG NMR comparison between surface oxides and sulfides on Pt-black show a large difference in chemical shift position (Δ~5800 ppm, 375 kHz), a clear indication that their local ^{195}Pt valence electron environments are distinct, consistent with their large differences in chemical

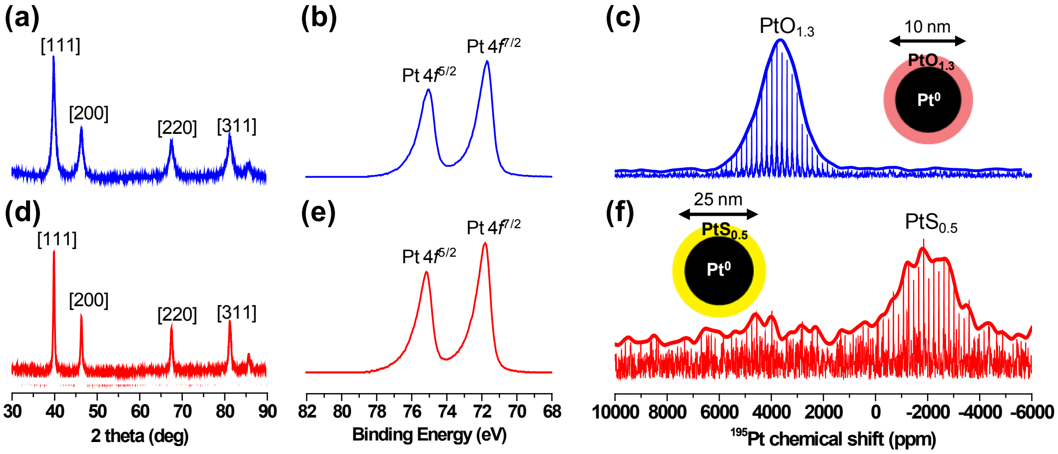

Figure 5.1. (a,d) XRD patterns, (b,e) Pt 4*f* XPS spectra, and (c,f) solid-state ^{195}Pt WURST-CPMG NMR spectra for (a)-(c) oxidized Pt-black and (d)-(f) sulfidized Pt-black. Interpolated and smoothed lineshapes are overlaid above each ^{195}Pt NMR spectrum. Proposed structures with relative length scales are depicted above each ^{195}Pt NMR spectrum. $PtO_{1.3}$ and $PtS_{0.5}$ stoichiometries were estimated from XPS spectra.

reactivity. The chemical shift (i.e., ppm) is a relative frequency scale that reflects the degree of nuclear spin magnetic shielding by valence and conduction electron distributions.[21] Integration and interpolation of individual spikelets of the spikelet pattern provides the actual spectral lineshape composed of a distribution of ^{195}Pt environments. The lineshape of surface oxides on Pt-black (Fig. 5.1c) is centered at 3,800 ppm and resembles a Gaussian distribution, consistent with non-uniform Pt oxide bond lengths and angles similar to a disordered glass.[22] Surface sulfides on Pt-black produce a unique and clearly resolved resonance that appears at -1,900 ppm

(Figure 5.1f). Negative ppm values suggest ^{195}Pt spins are more magnetically shielded by S compared to O electrons, which indicates that sulfidized Pt molecular orbitals are more occupied and unavailable for bonding. The lineshape for sulfidized Pt-black maintains an analogous Gaussian distribution with a smaller signal-to-noise ratio, which indicate similar degrees of local disorder for $PtO_{1.3}$ and $PtS_{0.5}$ and a smaller Pt surface area after treatment caused by particle sintering (consistent with XRD). The interior of bulk metallic Pt is known to have a characteristic signal observed near -40,000 ppm that is extremely well resolved from surface Pt oxides and sulfides, an advantage provided by conduction electrons coupling to ^{195}Pt spins through hyperfine (i.e., Knight shift) interactions.[6] These resolved ^{195}Pt NMR spectral details provide direct experimental evidence of differences in surface Pt electronic structure due to surface chemistry and can be correlated to known differences in reactivity. Moreover, the analysis of surface oxidized and sulfidized Pt-black provides a baseline for comparison with supported Pt nanoparticles that are additionally influenced by cluster size and support interactions.

5.3.2. Size effects of supported Pt nanoparticles

The effect of Pt nanoparticle size on Pt_xO_y environments was investigated by comparing surface oxides on Pt-black to oxidized Pt nanoparticles (Fig. 5.2a-c). Pt nanoparticle size and film thickness are known to strongly influence surface oxide stoichiometry and the resulting reactivity of Pt surfaces.[23-28] However, unique

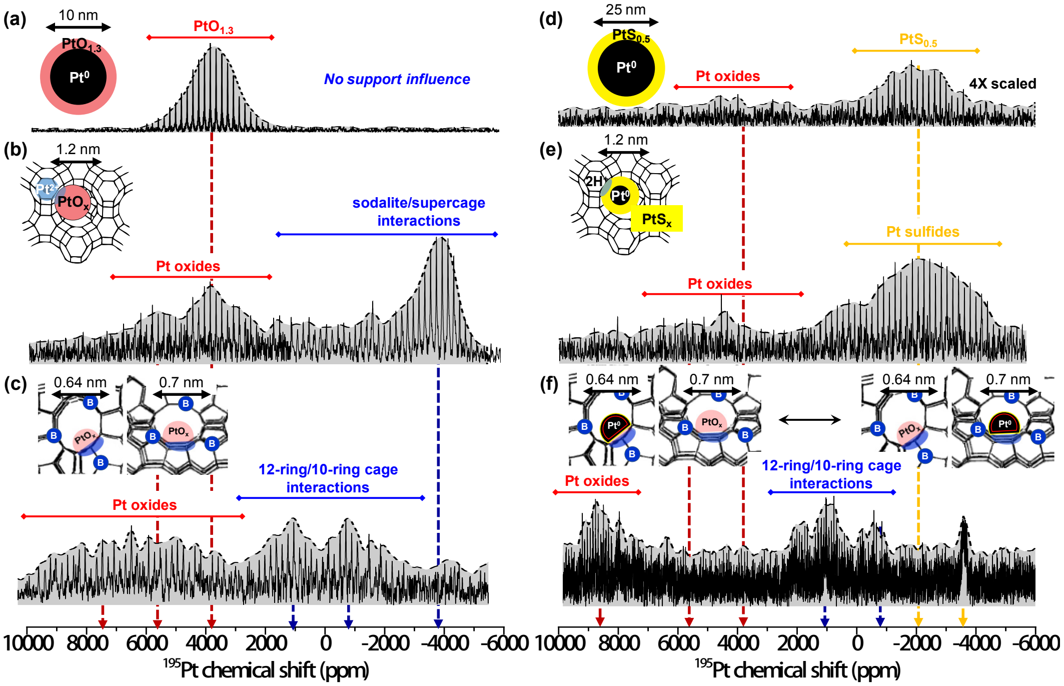

Figure 5.2. Solid-state ^{195}Pt WURST-CPMG NMR spikelet spectra (with smooth interpolated lineshapes) of (a-c) oxidized (~10 nm) and (d-f) sulfidized (~23 nm) (a,d) Pt-black surfaces and Pt nanoparticles supported on (b,e) zeolite NaY (15 wt%, 1-3 nm) and (c,f) B-SSZ-33 (0.5 wt%, 1 nm). Proposed local structures with relative length scales are depicted above each spectrum, with red, blue, and yellow-orange shaded regions indicating PtO$_x$ distributions, zeolite support interactions, and PtS$_x$ distributions.

electronic environments of surface Pt oxides, which are also precursors for reduced Pt catalysts, are difficult to assess for nanoparticles on oxide supports. The limited ability to deconvolute influences from size and support, as well as the low Pt loadings in practical heterogeneous catalysts, creates a challenging scenario for detecting molecular signatures of distinct Pt electronic environments in surface oxides. By comparing local molecular environments of supported respectively. This color code is also used to designate the width and position of unique ^{195}Pt environments, depicted as horizontal lines above each spectrum and vertical dashed arrows pointing towards the chemical shift axis, respectively.

By comparing local molecular environments of supported Pt oxide nanoparticles to oxidized surfaces of Pt-black, changes in Pt_xO_y distributions were distinguished from support interactions for Pt loadings down to 0.5 wt%. The solid-state ^{195}Pt NMR comparisons between surface oxides on Pt-black crystallites of ~10-25 nm (Fig. 5.2a) and Pt nanoparticles of 2 nm (Fig. 5.2b, 15 wt% on zeolite NaY), and 1 nm (Fig. 5.2c, 0.5 wt% on B-SSZ-33) show broader distributions of Pt_xO_y environments (red lines, 2,000-10,000 ppm) that appear at higher ppm values as particle size decreases. There appears to be one unique Pt oxide environment for Pt-black, two unique environments for 2 nm Pt nanoparticles, and a third emerging environment for 1 nm Pt nanoparticles (dashed red vertical lines). Broadened distributions and appearance of additional Pt_xO_y environments at higher ppm values suggest an increase in sub-oxide Pt moieties, which has been previously observed for Pt nanoparticle surfaces.[27,29] A predominance of step, edge, and defect sites emerge when particle size is decreased,[30] which can lead to a higher degree of unsaturated surface Pt atoms that promote sub-oxide surface environments. In contrast, highly overlapped distributions of Pt 4*f* XPS signals (PtO_x, PtS_x, Pt-support, Pt^0, Fig. 5.3)

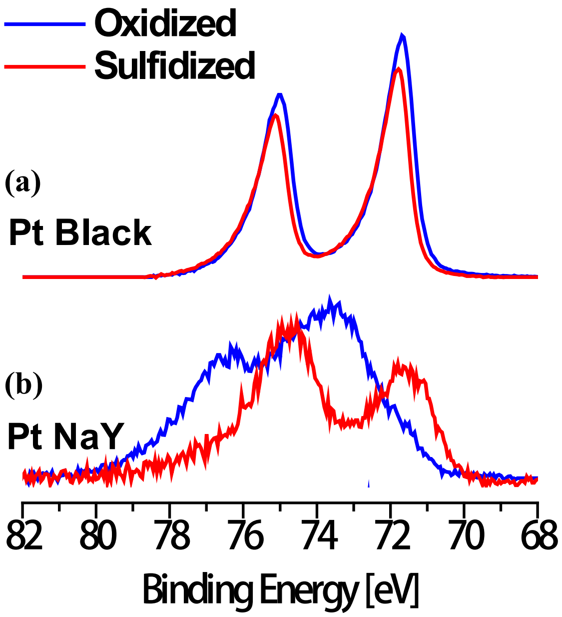

Figure 5.3. Pt 4*f* XPS spectra for oxidized (blue lines) and sulfidized (red lines) Pt catalysts.

prevent confident lineshape deconvolution. Owing to the sensitivity of ^{195}Pt NMR to molecular bonding, Pt_xO_y is clearly distinguished from PtS_x, Pt-support, and Pt^0 environments.

5.3.3. Zeolite interactions with supported Pt nanoparticles

Unique support interaction effects on local Pt environments were investigated by comparing oxidized Pt-black to Pt nanoparticles supported on zeolites NaY and B-SSZ-33. The influences of supports have been postulated to promote Pt nanoparticle stability,[31] reactant spillover,[3,32] and bifunctionality[33] during heterogeneous catalysis. However, the impacts of supports are also affected by nanoparticle size and surface composition, which convolutes their influences on local molecular Pt environments. Nevertheless, with knowledge of where surface Pt oxides appear in ^{195}Pt NMR spectra (Fig 5.2., red lines, 2,000 - 10,000 ppm), a simple comparison between oxidized Pt nanoparticles on distinct supports (Fig. 5.2a-c) readily enables identification of influences due to support interactions (blue lines, -5,000-3000 ppm). For oxidized Pt nanoparticles on zeolite NaY (Fig. 5.2b), there is a dominant spectral feature at -4,000 ppm that extends towards 2,000 ppm and is clearly resolved (electronically distinct) from Pt oxides near 4,000 ppm. The overall lineshape resembles a broadened asymmetric powder pattern with chemical shift anisotropy[21] (CSA) instead of a Gaussian distribution, which indicates a higher degree of molecular order and symmetry for these Pt environments (i.e., compared to disordered Pt oxides) within the crystalline zeolite NaY structure. The origins of ordered and symmetric Pt environments in zeolite structures arises from defined cage environments that contain individual Pt atoms. Previously, oxidation treatment conditions were shown to have a strong influence on nanoparticle dispersion within zeolite NaY, suggesting a preference for Pt^{2+} ion migration into the smaller sodalite cages at higher temperatures (600 °C) and formation of Pt oxide clusters within larger supercages at lower temperatures (400 °C, used in the present study).[34] The presence of locally disordered Pt oxide environments and molecularly ordered interactions within zeolite NaY signifies a distribution of Pt within the two cages, with a large fraction as Pt^{2+} ions in highly symmetric sodalite cages. By comparison, interactions between Pt and zeolite B-SSZ-33 (Fig. 5.2c) produce two Gaussian signals centered at -750 and 1,100 ppm, distinct from both Pt oxide environments and zeolite NaY interactions with Pt. Analogous to zeolite NaY, these support interactions likely arise from Pt within distinct cage environments of the zeolite framework, namely, 10 and 12 ring cages for zeolite SSZ-33.[35] However, instead of asymmetric powder patterns, the appearance of Gaussian distributions indicate interactions with Pt clusters, rather than individual Pt atoms. An ordered distribution of B in the SSZ-33 framework, which improves Pt nanoparticle dispersion and stability, is evidenced by relatively narrow spectral distributions that indicate locally ordered interactions between B-SSZ-33 and Pt oxide nanoparticles.

5.3.4. Sulfidation of supported Pt nanoparticles

The impact of sulfidation on Pt nanoparticle support interactions was investigated for Pt-NaY (Fig. 5.2e) and Pt-B-SSZ-33 (Fig. 5.2f). While it is well known that sulfur can strongly impact the activity and selectivity of Pt catalysts, depending on the nature of Pt-support interactions, supported Pt nanoparticle catalysts can have varying degrees of sulfur tolerance.[36-39] Pt-support interactions have been observed to influence support acidity and alkalinity,[40,41] but molecular signatures of these interactions and influences upon sulfidization are difficult to establish. As shown above, sulfidized Pt-black surfaces (Fig. 5.2d) produce unique ^{195}Pt environments that appear near -2,000 ppm. A comparison between solid-state ^{195}Pt NMR spectra for oxidized (Fig. 5.2b) and sulfidized (Fig. 5.2e) Pt nanoparticles supported in zeolite NaY (a sulfur intolerant catalyst) indicates complete disruption of support interactions (Fig. 5.2b, -4,000 ppm) and Pt oxide resonances (Fig. 5.2c, 2,500 - 10,000 ppm), accompanied by an increase in Pt sulfide resonances (Fig. 5.2d,e, -2,000 ppm). An analogous comparison between oxidized (Fig. 5.2c) and sulfidized (Fig. 5.2f) Pt nanoparticles supported in zeolite B-SSZ-33 indicates that only one of two support interactions (Fig. 5.2c, more negative ppm) is diminished after sulfur treatment, suggesting that the remaining cage interaction (Fig. 5.2c, more positive ppm) promotes higher Pt sulfur tolerance in B-SSZ-33. While a further study is necessary to more fully elaborate on the origins of Pt sulfur tolerance in zeolites, there are clear indications from the molecular level details of solid-state ^{195}Pt WURST-CPMG NMR that both Pt oxide environments and Pt-support interactions are being affected by sulfur treatments.

5.3.5. Lineshape Analyses

Lineshape analyses and comparisons between oxidized and sulfidized Pt-black, Pt-NaY, and Pt-B-SSZ-33 enabled relative contributions of ^{195}Pt environments and their chemical shift parameters (i.e., position = δ^{i}_{iso}, width = $\Delta\sigma$) to be established and tabulated (Fig. 5.4, Table 1). Gaussian distributions were used for disordered surface oxides, sulfides, and cluster-support interactions within zeolite B-SSZ-33, while a CSA distribution was used for ordered Pt^{2+} interactions within sodalite cages of zeolite NaY. Spectra of oxidized and sulfidized surfaces of Pt-black (Fig. 5.4a,d) were used as initial lineshape references for the deconvolution of additional oxide, sulfide, and support interaction contributions in the spectra for Pt-NaY (Fig. 5.4b,e)

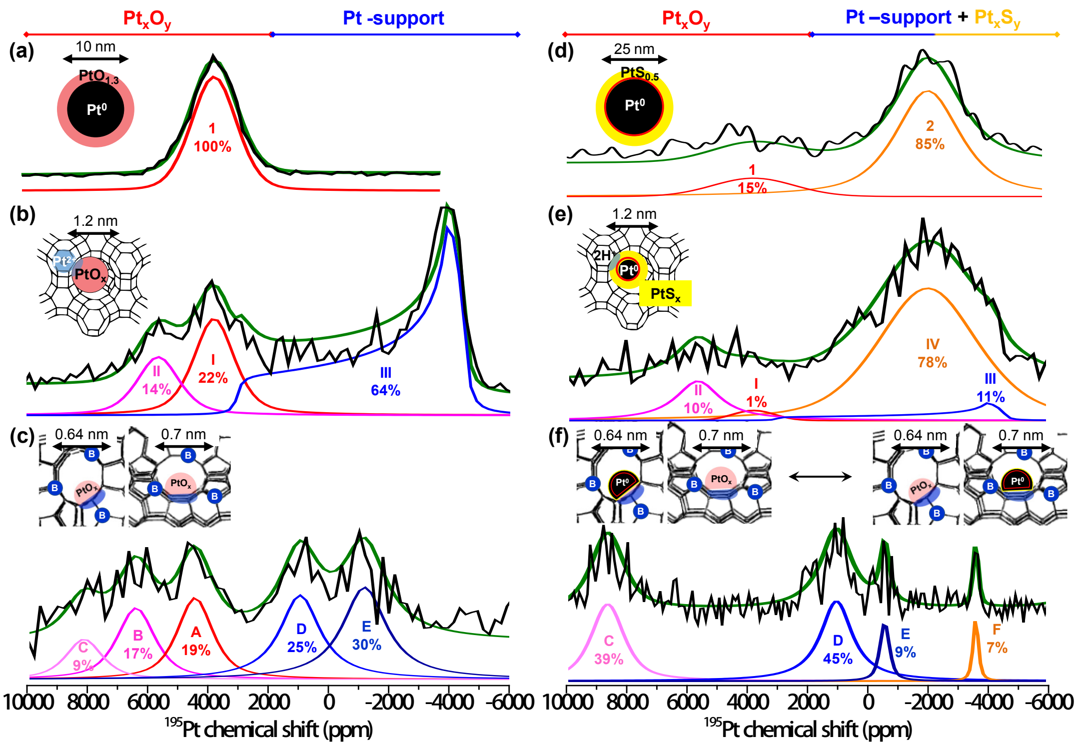

Figure 5.4. Lineshape deconvolutions of solid-state ^{195}Pt WURST-CPMG NMR spikelet spectra in Figure 5.2 of (a-c) oxidized and (d-f) sulfidized (a,d) Pt-black surfaces and Pt nanoparticles supported on (b,e) zeolite NaY (15 wt%, 1-3 nm) and (c,f) B-SSZ-33 (0.5 wt%, 0.X nm). Proposed local structures with relative length scales are depicted above each spectrum, with red, blue, and yellow/orange shaded regions indicating PtO$_x$ distributions, zeolite support interactions, and PtS$_x$ distributions, respectively. This color code is also used to designate lineshape components that reflect distinct ^{195}Pt environments.

Table 5.1. Chemical Shift Parameters of lineshape components for oxidized and sulfidized samples in Figure 5.4.

^{195}Pt Environments		Oxidized Samples			Sulfidized Samples		
Samples	Component "*i*"	δ^i_{iso} [ppm]	$\Delta\sigma$ [ppm]	% Area	δ^i_{iso} [ppm]	$\Delta\sigma$ [ppm]	% Area
Pt Black	1	3,800	1,800	100	3,800	3,200	15
	2				-2,000	2,600	85
Pt-NaY	I	3,800	1,600	22	3,800	1,600	1
	II	5,700	1,700	14	5,700	1,700	10
	III	-1,800	4,900	64	-1,800	4,900	11
	IV				-2,000	3,900	78
Pt-B-SSZ-33	A	4,400	1,400	19			
	B	6,400	1,500	17			
	C	8,100	1,400	9	8,600	1,300	39
	D	900	1,600	25	1,000	1,300	45
	E	-1,200	1,800	30	-600	400	9
	F				-3,600	200	7

and Pt-B-SSZ-33 (Fig. 5.4c,f). Although percent contributions of unique ^{195}Pt distributions are not precisely quantitative (i.e., due to slight differences in signal relaxation), the values provide reasonable estimates of their relative populations. Additionally, while assignments for these spectral features cannot be fully established without multi-dimensional NMR methods, conclusions regarding the physical significance of spectral components can still be deduced.

Comparisons between oxidized and sulfidized Pt-NaY and Pt-B-SSZ-33 readily enabled sulfur tolerant ^{195}Pt environments in Pt-B-SSZ-33 to be identified. In zeolite NaY, there are 6-ring and 12-ring cages, while in zeolite SSZ-33, there are 10-ring and 12-ring cages. As previously mentioned, sulfidation disrupts support interactions in Pt-NaY, which is correlated with its well known sulfur intolerance.[42] However, for Pt-B-SSZ-33 (Fig. 5.4c,f), only the more negative (-1,200) ppm signal is diminished, while the more positive (940) ppm signal is maintained. Given the commonality of 12-ring cages present within Pt-NaY and Pt-B-SSZ-33, it is deduced that the unique sulfur tolerant environments within Pt-B-SSZ-33 are within 10-ring cages. These suggestions are further corroborated by comparing the Pt_xO_y environments of Pt-NaY (Fig. 5.4b,e) and Pt-SSZ-33 (Fig. 5.4c,f), which shows that only the distinct and higher (8,600) ppm signal in Pt-B-SSZ-33 can be readily maintained after sulfidation. The relatively small quantity of Pt_xS_y signal indicates that the sulfur coverage is very low and likely below a full monolayer. Moreover, the sulfidation treatment of Pt-B-SSZ-33 produced a Pt_xS_y environment (-3,600 ppm) with a very narrow distribution, suggesting the presence of a highly uniform surface Pt sulfide environment that may also be a molecular indication for Pt nanoparticle sulfur tolerance.

5.4. Conclusions

The influence of surface composition, nanoparticle size, and support interactions were established for bulk Pt (i.e., Pt-black) and supported (i.e., zeolite NaY, SiO_2, zeolite B-SSZ-33) Pt nanoparticles using recently advanced solid-state ^{195}Pt WURST-CPMG NMR. Contrary to XRD and XPS, ^{195}Pt NMR is able to distinguish large differences between Pt oxide and sulfide environments, indicative of large differences in valence electron structure. Identification of surface ^{195}Pt oxide and sulfide environments enabled influences from particle size effects and support interactions to be readily identified. Smaller Pt oxide and sulfide nanoparticles produced broader (more disordered) distributions of sub-oxide and sub-sulfide Pt environments, and Pt environments within distinct cages of zeolites NaY and B-SSZ-33 were established. Locally ordered interactions between the zeolite frameworks and supported Pt^{2+} ions and Pt oxide nanoparticles were indicated. Sulfur treatments selectively diminished specific support interactions, which enabled identification of the 10-ring cages as the sulfur tolerant environments in zeolite Pt-B-SSZ-33. Furthermore, local molecular ^{195}Pt environments could be distinguished for Pt nanoparticle loadings down to 0.5 wt%, a practical metal loading used in industrial heterogeneous catalysis. It is readily apparent that the advanced solid-state ^{195}Pt WURST-CPMG methodology provides the necessary excitation bandwidth and sensitivity to be highly informative on the local molecular Pt environments in supported nanoparticle catalysts. By understanding the subtle differences and similarities between local ^{195}Pt molecular environments of supported Pt nanoparticles, molecular insights can be obtained and correlated with particle dispersion, stability, and reactivity, topics for further studies.

5.5. Acknowledgements

Experiments were conducted in the Central Facilities of the UCSB Materials Research Laboratory MRSEC Program of the NSF under Award No. DMR-1121053; a member of the NSF-funded Materials Research Facilities Network(www.mrfn.org). Use of the Central Facilities was supported by the U.S. National Science Foundation under Grant No. CHE-1059108. L.C.J thanks the NSF-

IOSE-PIRE Program (0968399) and the NSF ConvEne IGERT Program (NSF-DGE 0801627) for fellowship support.

5.6. References

(1) Somorjai, G. A.; Park, J. Y. *Chem. Soc. Rev.* **2008**, *37*, 2155.

(2) Henry, C. Adsorption and Reaction at Supported Model Catalysts. In Catalysis and Electrocatalysis at Nanoparticle Surfaces; Wieckowski, A., Savinova, E. R., Vayenas, C. G., Eds.; *Marcel-Dekker, Inc.*: New York, **2009**.

(3) Happel, M.; Mysliveček, J.; Johánek, V.; Dvořák, F.; Stetsovych, O.; Lykhach, Y.; Matolín, V.; Libuda, *J. Catal.* **2012**, *289*, 118.

(4) Nørskov, J.; Bligaard, T.; Rossmeisl, J.; Christensen, C. *Nat. Chem.* **2009**, *1*, 37.

(5) Kubička, D.; Kumar, N.; Venäläinen, T.; Karhu, H.; Kubičková, I.; Österholm, H.; Murzin, D. Y. J. *Phys. Chem. B* **2006**, *110*, 4937.

(6) Rhodes, H. E.; Wang, P.-K.; Stokes, H. T.; Slichter, C. P.; Sinfelt, J. H. *Phys. Rev. B* **1982**, *26*, 3559.

(7) Pelupessy, P. *J. Am. Chem. Soc.* **2003**, *125*, 12345.

(8) Patz, S.; Hersman, F. W.; Muradian, I.; Hrovat, M. I.; Ruset, I. C.; Ketel, S.; Jacobson, F.; Topulos, G. P.; Hatabu, H.; Butler, J. P. *Euro. J. Rad.* **2007**, *64*, 335.

(9) Tan, F.; Du, B.; Danberry, A. L.; Park, I.-S.; Sung, Y.-E.; Tong, Y. *Faraday Discuss.* **2008**, *140*, 139.

(10) MacGregor, A. W.; O'Dell, L. A.; Schurko, R. W. *J. Magn. Reson.* **2011**, *208*, 103.

(11) Lucier, B. E. G.; Reidel, A. R.; Schurko, R. W. *Can. J. Chem.* **2011**, *89*, 919.

(12) Adams, R.; Shriner, R. L. *J. Am. Chem. Soc.* **1923**, *45*, 2171.

(13) McCabe, R. W.; Schmidt, L. D. *Surf. Sci.* **1976**, *60*, 85.

(14) Salmerón, M.; Brewer, L.; Somorjai, G. A. *Surf. Sci.* **1981**, *112*, 207.

(15) Ackermann M.; Pedersen, T.; Hendriksen, B.; Robach, O.; Bobaru, S.; Popa, I.; Quiros, C.; Kim, H.; Hammer, B.; Ferrer, S.; Frenken, J. *Phys. Rev. Lett.* **2005**, *95*, 255505.

(16) Somorjai, G. *J. Catal.* **1972**, *27*, 453.

(17) Leclercq, G.; Boudart, M. *J. Catal.* **1981**, *71*, 127.

(18) Rodriguez, J. A.; Kuhn, M.; Hrbek, J. *Chem. Phys. Lett.* **1996**, *251*, 13.

(19) Páal, Z.; Matusek, K.; Muhler, M. *Appl. Catal. A Gen.* **1997**, *149*, 113.

(20) Baldyga, L. M.; Blavo, S. O.; Kuo, C.-H.; Tsung, C.-K.; Kuhn, J. N. *ACS Catal.* **2012**, *2*, 2626.

(21) Widdifield, C. M.; Schurko, R. W. *Concept. Magnetic Res. A* **2009**, *34A*, 91.

(22) Fayon, F.; Bessada, C.; Massiot, D.; Farnan, I.; Coutures, J. P. *J. Non-Cryst. Solids* **1998**, *232-234*, 403.

(23) Mayell, J. S.; Longer, S. H. *J. Electrochem. Soc.* **1964**, *111*, 438.

(24) Mayell, J. S. *J. Electrochem. Soc.* **1966**, *113*, 385.

(25) McCabe, R. W.; Wong, C.; Woo, H. S. *J. Catal.* **1988**, *114*, 354.

(26) McBride, J.; Graham, G.; Peters, C.; Weber, W. *J. Appl. Phys.* **1991**, *69*, 1596.

(27) Hwang, C.-P.; Yeh, C.-T. *J. Catal.* **1999**, *182*, 48.

(28) Olsson, L.; Fridell, E. *J. Catal.* **2002**, *210*, 340.

(29) Hwang, C.-P.; Yeh, C.-T. *J. Mol. Catal. A: Chem.* **1996**, *112*, 295.

(30) Lundwall, M.; McClure, S.; Goodman, D. *J. Phys. Chem. C* **2010**, *114*, 7904.

(31) Lin, W.; Herzing, A.; Kiely, C.; Wachs, I. *J. Phys. Chem. C* **2008**, *112*, 5942.

(32) Gorodetskii, V. V.; Sametova, A. A.; Matveev, A. V.; Tapilin, V. M. *Catal. Today* **2009**, *144*, 219.

(33)Yamada, Y.; Tsung, C.-K.; Huang, W.; Huo, Z.; Habas, S. E.; Soejima, T.; Aliaga, C. E.; Somorjai, G. A.; Yang, P. *Nature Chemistry* **2011**, *3*, 372.

(34) (a) Chmelka, B. F.; Ryoo, R.; Liu, S.-B.; de Menorval, L. C.; Radke, C. J.; Petersen, E. E.; Pines, A. *J. Am. Chem. Soc.* **1988**, *110*, 4465. (b) Chmelka, B. F.; Went, G. T.; Csencsits, R.; Bell, A. T.; Petersen, E. E.; Radke, C. J. *J. Catal.* **1993**, *144*, 506.

(35) Gil, B.; Zones, S. I.; Hwang, S. J.; Bejblová, M.; Čejka, J. *J. Phys. Chem. C* **2008**, *112*, 2997.

(36) Guenin, M.; Breysse, M.; Frety, R.; Tifouti, K.; Marecot, P.; Barbier, J. *J. Catal.* **1987**, *105*, 104.

(37) Kim, C.; Somorjai, G. A. *J. Catal.* **1992**, *134*, 179.

(38) Fukunaga, T.; Ponec, V. *J. Catal.* **1995**, *157*, 550.

(39) Navarro, R.; Pawelec, B.; Trejo, J.; Mariscal, R.; Fierro, J. *J. Catal.* **2000**, *189*, 184.

(40) Coq, B.; Walter, C.; Brown, R.; McDougall, G.; Figuéras, F. *Catal. Lett.* **1996**, *39*, 197.

(41) Chang, J.-R.; Chang, S.-L.; Lin, T.-B. *J. Catal.* **1997**, *169*, 338.

(42) Miller, J. T.; Koningsberger, D. C. *J. Catal.* **1996**, *162*, 209.

Chapter 6

Distinguishing interior and surface Pt environments in bulk and supported Pt oxides and sulfides.

Adapted from Inorganic Chemistry submission:

Louis C. Jones,[a] Michael J. Gordon, [a] Fabio Ribeiro,[b] Nicholas Delgass,[b] Jefferey Miller,[c] and Bradley F. Chmelka.[a]

[a] *University of California, Santa Barbara, California 93106-5080, USA*

[b] *Purdue University, West Lafayette, Indiana 47907, USA*

[c] *Argonne National Laboratory, Lemont, Illinois 60439, USA*

Abstract

Unique molecular environments of interior and surface ^{195}Pt atoms in bulk and supported Pt oxides and sulfides (PtO_2, PtS_2, oxidized/sulfidized Pt-black and Pt-SiO_2) were established to investigate similarities and differences between local Pt electronic environments. Using a recently advanced, broadband and sensitivity enhanced solid-state ^{195}Pt NMR method (i.e., WURST-CPMG), in combination with structural and compositional properties from XRD and XPS, the influences of oxidation, sulfidation, and SiO_2 support on the local distributions of ^{195}Pt molecular environments were made readily apparent. It is shown that the similarities and differences between the distributions of ^{195}Pt environments can be correlated with their unique catalytic properties. Overall, the study demonstrates how local molecular ^{195}Pt structure, composition, (dis)order, and unique electronic environments can be distinguished in a variety of catalytically relevant, heterogeneous Pt materials.

6.1. Introduction

Degrees of local molecular order and disorder within heterogeneous Pt-containing materials have substantial effects on catalytic reactivity and stability. For example, the unique molecular configurations of disordered surface Pt atoms in oxidized[1-3] and sulfidized[4-7] environments lead to vast differences in surface reactivity for Pt (nano)particles and clusters. For bulk Pt oxides and sulfides, crystalline domains are typically accompanied by disordered environments producing a semi-crystalline structure.[8,9] The chemical nature of these disordered environments is difficult to establish for ensembles of disordered surface atoms and semi-crystalline materials. Atomic-scale features create a challenging scenario for the characterization of relevant properties that indicate unique distributions of Pt electronic environments, the determining factor for catalytic reactivity.[10-12] Characterization methods such as X-ray diffraction (XRD) and X-ray photoelectron spectroscopy (XPS) provide information regarding ordered structures and surface stoichiometries, but signals from unique surface Pt environments are oftentimes undetectable or overlapping with bulk signals. Development of complementary techniques that are more sensitive to local valence and conduction electron environments can enable understanding of the molecular-level characteristics that are indicators of unique catalytic reactivity and stability.

Nuclear magnetic resonance (NMR) spectroscopy is a sensitive probe of local electronic environments within solid-state materials, including those containing heavy elements, such as ^{199}Hg,[13] ^{207}Pb,[14] ^{235}U,[15] and ^{209}Bi.[16] However, despite the technological importance of Pt-containing compounds and catalysts, the implementation of solid-state ^{195}Pt NMR has remained a significant challenge. This is because of the hardware limitations presented by the enormous (>50,000 ppm) shift range over which ^{195}Pt NMR signals can be distributed.[17] By comparison, ^{1}H and ^{13}C exhibit shift ranges of 20 ppm and 1,000 ppm, respectively. The significantly larger ^{195}Pt shift range reflects the intrinsic sensitivity of ^{195}Pt nuclei to their local electronic environments, and in principle, can be exploited to obtain detailed compositional and structural information.[18]

Very recent advancements in the excitation and detection of NMR spectra with ultra-broad signals have opened new opportunities to acquire solid-state ^{195}Pt NMR spectra of Pt-containing compounds and materials that have previously lacked the molecular resolution and practicality to warrant widespread use. Using advanced frequency-swept NMR pulses, broad ^{195}Pt NMR spectra can be acquired by adiabatically exciting very large frequency ranges (~10,000 ppm) with much higher efficiency and resolution compared to conventional solid-state NMR techniques.[19] Schurko and coworkers have recently demonstrated the use of the *w*ideband, *u*niform *r*ate, *s*mooth *t*runcation (WURST[20]) technique in conjunction with a Carr-Purcell-Meiboom-Gill (CPMG[21]) train of radio frequency pulses to excite quadrupolar[22] and spin-1/2 (including ^{195}Pt)[23] nuclei. This new approach (referred to as WURST-CPMG) is a highly versatile method that allows ultra-broad ^{195}Pt NMR spectra to be acquired with improved sensitivity and resolution in far less time than previously possible. While WURST-CPMG has been used to characterize ^{195}Pt environments in ordered molecular solids, the technique has yet to be applied to heterogeneous Pt materials with varying degrees of local order and disorder.

Herein, locally ordered and disordered molecular environments of interior and surface ^{195}Pt atoms in bulk and supported Pt oxides and sulfides (PtO_2, PtS_2, oxidized/sulfidized Pt-black and Pt-SiO_2) were established using solid-state ^{195}Pt WURST-CPMG NMR, in combination with XRD and XPS. The enhanced sensitivity and resolution offered by ^{195}Pt WURST-CPMG NMR enabled novel assignments of spectral details to electronically distinct surface ^{195}Pt environments. By characterizing ^{195}Pt environments in a variety of bulk and nanoparticle counterparts, the influences of surface chemistry, ensemble size, and support interactions on local ^{195}Pt electronic environments are readily assessable. Moreover, spectral similarities and differences between ^{195}Pt distributions were paralleled with known and measured catalytic reactivity. The methods provide a general framework with which to establish distributions of ^{195}Pt molecular environments in a wide variety of solid-state Pt-containing materials.

6.2. Experimental Section

α-PtO_2 and PtS_2 samples were measured as received (Sigma Aldrich). Oxidized samples of Pt-black (Sigma Aldrich) were treated with O_2 at 120 ^{o}C, while sulfidized samples were treated with H_2 at 120 ^{o}C for 30 min and S_2 at 120 ^{o}C for 1 hr. Pt-SiO_2 samples were prepared provided by Dr. Jeffrey Miller (Argonne National Laboratory). Oxidized samples were treated with O_2 to 200 ^{o}C over a 5 hour period, while sulfidized samples were first oxidized then treated with H_2 to 250 ^{o}C over a 5 hour period and S_2 at 120 ^{o}C for 1 hr.

Structural similarities and differences between bulk PtO_2 and PtS_2, and oxidized/sulfidized surfaces of Pt-black were established by measuring and directly analyzing their respective Pt environments by solid-state ^{195}Pt NMR. Specifically, solid-state ^{195}Pt WURST-CPMG NMR spectra were acquired at 7.06 T on a Bruker

AVANCE NMR spectrometer operating at 300.07 and 64.49 MHz for ^{1}H and ^{195}Pt, respectively, with parameters optimized according to references.[22,23] WURST-CPMG pulses of 50 ms (~2 MHz) were applied at center frequencies of 64.72 and 64.28 MHz using forward and reverse frequency sweeps to compensate for transverse relaxation of ^{195}Pt magnetization during the sweeps. An acquisition time of 80 ms was used to measure the free induction decays of each subsequent CPMG loop (12 total) with a recycle delay of 0.5. Magnitude calculations were performed on Fourier transformed spectra to produce the observed ^{195}Pt spikelet patterns with a span of >500 kHz. Qualitative lineshape analyses were performed using the program DMFIT[24] after integration of each characteristic CPMG spikelet in the spectra.

X-ray photoelectron spectra (XPS) were measured using a Kratos Axis Ultra system with a monochromated Al Ka source (1486.6 eV, 225 W). An electron flood gun was used for charge neutralization to compensate for the non-conducting samples. All samples were referenced to surface carbonaceous species (284.7 eV).

X-ray diffraction (XRD) patterns were measured using a Philips X'Pert MPD with a 3kW Cu K_α (1.5405 Å) X-ray source.

6.3. Results and Discussion

6.3.1. Bulk and surface ^{195}Pt oxides and sulfides

Distinctions between bulk and surface molecular ^{195}Pt environments in PtO_2, PtS_2, oxidized, and sulfidized Pt-black surface were readily apparent from their

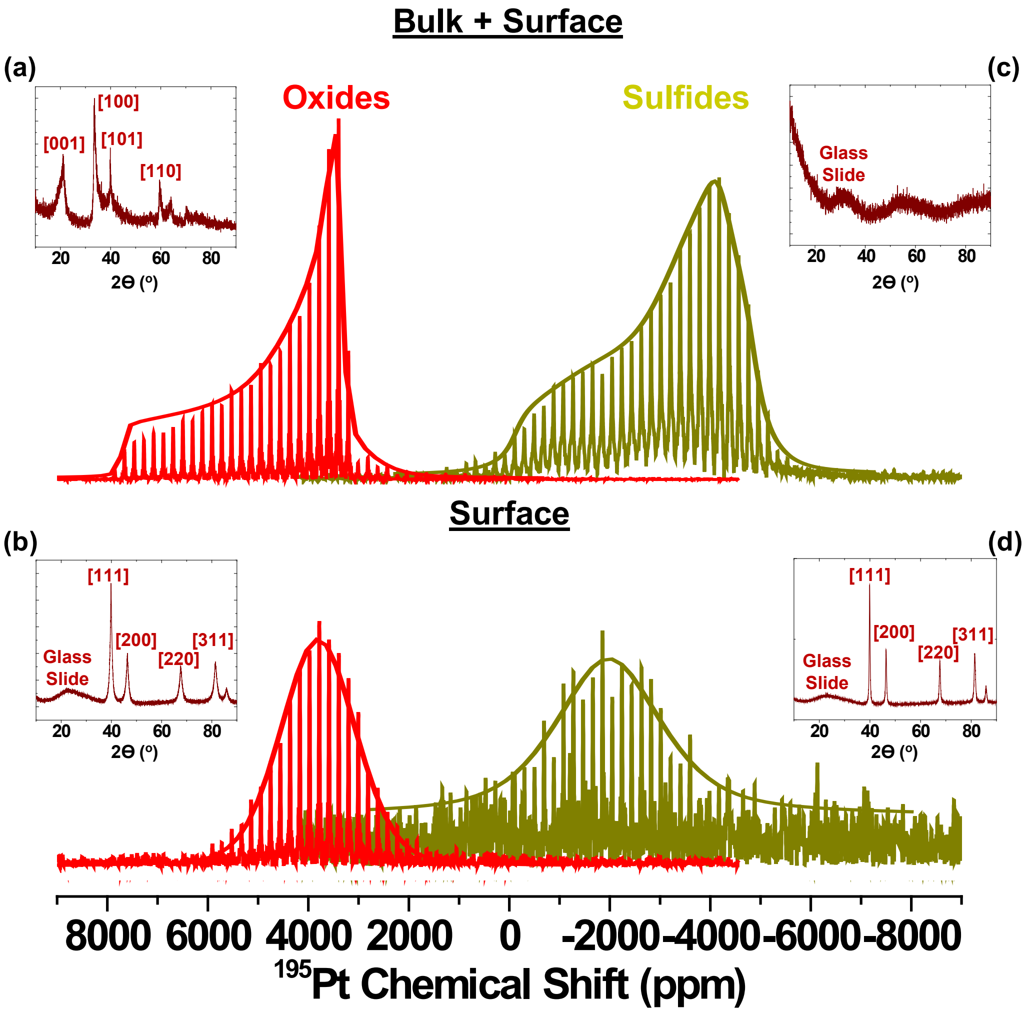

Figure 6.1. Static solid-state ^{195}Pt WURST-CPMG NMR spectra and lineshapes of bulk + surface species, (a) α-PtO_2 and (c) PtS_2, and surface species, (b) oxidized and (d) sulfidized Pt-black surfaces. The X-ray diffraction patterns for each material are shown as insets.

solid-state ^{195}Pt WURST-CPMG NMR spectra (Figure 6.1). The ^{195}Pt NMR spectrum of α-PtO_2 (Figure 6.1a) shows a broad lineshape that is characteristic of a crystalline powder with a chemically distinct Pt site possessing anisotropic chemical shift interactions (i.e., chemical shift anisotropy, CSA).[25] The D_{3d} bonding symmetry of Pt in a CdI_2 structure is axially symmetric, as manifested by an asymmetric spectral distribution with high intensities near 3,500 ppm, and lower intensities that span towards 8,000 ppm. The XRD pattern of α-PtO_2 (Figure 6.1a, inset) is consistent with the previously observed CdI_2 hexagonal unit cell that consists of stacked Pt planes sandwiched between O atoms.[8] However, semi-crystallinity is clearly observed, evidenced by *c*-axis (001) line broadening in the diffraction pattern. Upon closer inspection of the α-PtO_2 ^{195}Pt NMR signal (3,000-1,000 ppm), additional intensity is observed to extend beyond what is typical for an axially symmetric CSA lineshape.[25] This additional intensity is consistent with a broad distribution of disordered Pt oxide environments (similar to a glass[26]), which may be attributed to variations in *c*-axis stacking and/or surface oxides that exhibit heterogeneity in bond lengths and angles.

^{195}Pt surface oxides were identified by probing oxidized Pt-black surfaces (Fig. 6.1b), which indicated a broad distribution of ^{195}Pt oxide environments that lacked local order. The structure of surface oxides on Pt often exhibits significant heterogeneity and has been observed to vary between PtO and PtO_2 morphologies.[27,28] The XRD pattern (Figure 6.1b, inset) only reveals the FCC structure of metallic Pt-black, without indications of Pt oxides. However, the location of the ^{195}Pt NMR lineshape for oxidized Pt-black surfaces resonates near ~3,800 ppm and is very near the highest intensity for α-PtO_2, but with a Gaussian distribution (i.e., not CSA) of oxide bond lengths and angles that reflect locally disordered environments. Overlap near the highest intensities of α-PtO_2 suggest that surface oxides on Pt-black are PtO_2-like. Moreover, this distribution of resonances extends to lower frequencies (3000-1000 ppm), similar to the low frequency resonances of α-PtO_2 (Figure 6.1a), features that suggest similar Pt oxide environments surround ordered Pt-black and α-PtO_2 crystallites.

PtS_2, which is known to have the analogous CdI_2 structure of α-PtO_2,[29] provides an ideal comparison for understanding electronic influences on local ^{195}Pt environments. Given the structural similarity of PtS_2 and α-PtO_2, changes in the local density of states at the Fermi energy level when Pt is bonded to S compared to O will cause changes in ^{195}Pt chemical shift distributions.[30] The ^{195}Pt NMR spectrum of PtS_2 (Fig. 6.1c) has significantly lower ppm values (-6,000 to 0 ppm) as compared to α -PtO_2 (0 to 8000 ppm), emphasizing their very distinct electronic environments. Nonetheless, the solid-state ^{195}Pt NMR spectrum reveals intensity that resembles a highly broadened, yet axially symmetric CSA powder pattern, which indicates the presence of ordered CdI_2 grains with a small amount of more disordered sites. The X-ray diffraction pattern for PtS_2 (Fig 6.1c, inset) shows that there is little to no long-range periodic order, highlighting the sensitivity of solid-state ^{195}Pt NMR to locally ordered and disordered environments. In similar fashion to overlapping sites in the ^{195}Pt NMR spectrum of α-PtO_2, the underlying resonances in PtS_2 are composed of overlapping interior and surface ^{195}Pt distributions.

^{195}Pt surface sulfides were identified by probing sulfidized Pt-black surfaces (Fig. 6.1d), which shows a spectrum that exhibits locally disordered bonding environments. The spectral lineshape resembles a Gaussian distribution of Pt sites, which reflects large heterogeneity in sulfide bond lengths and angles. The X-ray diffraction pattern (Fig. 6.1d, inset) shows the expected FCC structure of metallic Pt-black, with no indication of Pt sulfides. The ^{195}Pt NMR spectral position for surface sulfides on Pt-black is located at -2000 ppm, overlapping with signals for PtS_2 and within error (+/- 200 ppm) of previously measured values for single crystals of PtS (-1850 ppm[31]). However, unlike surface Pt oxides in α-PtO_2, surface Pt sulfides overlap with the less intense side of the asymmetric PtS_2 spectrum. These observations strongly suggest that surface Pt sulfides on Pt-black are PtS-like.

6.3.2. Deconvolution of ordered and disordered ^{195}Pt environments

Using the ^{195}Pt NMR distributions for surface oxides on Pt-black, the spectrum of bulk α-PtO_2 can be deconvoluted into contributions from ordered interior and disordered surface ^{195}Pt oxide environments. As a representation of locally ordered environments, CSA lineshape fits can be used to extract principal components of the chemical shift tensor (δ_{xx}, δ_{yy}, and δ_{zz}).[25] These chemical shift tensor values reflect the relative resonant frequency of a nuclear spin, shielded by electrons, when oriented with respect to its principle components in an applied magnetic field. The coordinate system for the orthogonal principle component vectors of the chemical shift tensor can be inferred by inspection for crystal structures with axial symmetry, whereby two of the directions are chemically similar (i.e., possess symmetry). For α-PtO_2, the *xx* and *yy* directions are in the plane of the Pt atom layers in the CdI_2 structure (Figure 6.2a, inset sites 1), while the *zz* direction is orthogonal to this plane and points towards Pt-O bonds that are in a trigonal bipyramidal arrangement. The precise direction of in-plane tensor components (*xx* and *yy*) is ambiguous for materials other than single crystals, but their relative orientations have been previously linked to molecular symmetry axes of the chemical compound.[32] Nonetheless, it stands to reason that δ_{xx} and δ_{yy} will have similar chemical shift values if their orientations are in the plane of Pt atom layers within the CdI_2 crystal structure. δ_{xx}, δ_{yy}, and δ_{zz} can be averaged to obtain the commonly measured isotropic chemical shift ($\delta_{iso} = [\delta_{xx} + \delta_{yy} + \delta_{zz}]/3$), and can also be re-expressed with a CSA axiality ($\Delta\sigma = \delta_{zz} - \delta_{iso}$) and asymmetry parameter ($\eta = [\delta_{yy} - \delta_{xx}]/[\delta_{zz} - \delta_{iso}]$), which reflect the spread of chemical shift values and the molecular symmetry of the local environments, respectively. As a representation of locally disordered environments, Gaussian distributions can be used to model the ^{195}Pt NMR spectra, with peak position as δ_{iso} and the width as $\Delta\sigma$. These chemical shift parameters associated with ^{195}Pt lineshape components from α-PtO_2 and oxidized Pt-black surfaces are indicated in Figure 6.2a,b and tabulated in Table 6.1. A small value of η ~0.08 (i.e., $\delta^{1}_{xx} \sim \delta^{1}_{yy}$) for site 1 is consistent with the D_{3d} molecular symmetry of Pt

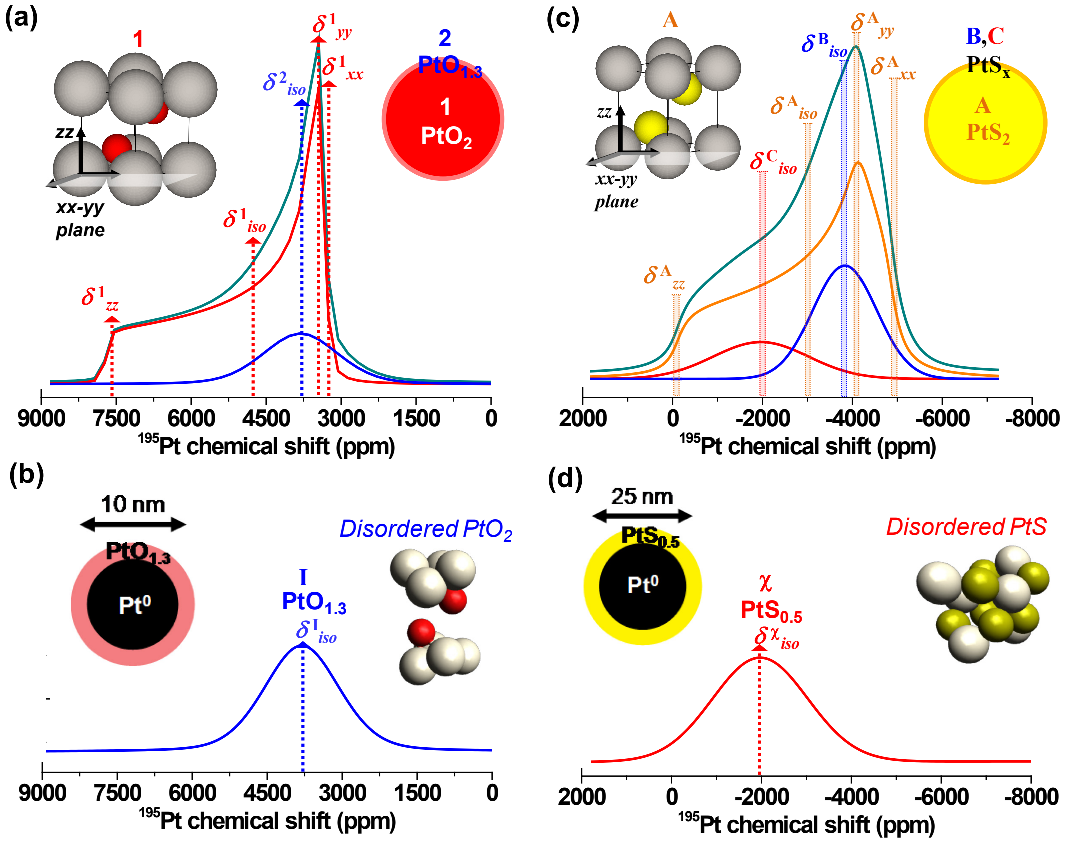

Figure 6.2. Representative fits of the experimental solid-state ^{195}Pt WURST-CPMG NMR spectra in Figure 1 for (a) α-PtO_2, (b) surface-oxidized Pt-black, (c) PtS_2, and (d) surface-sulfidized Pt-black. Schematics diagrams depicting the distinct ^{195}Pt atom environments in the materials accompany each spectrum (Pt atom sites are shown as grey/beige, oxygen atoms as red, sulfur atoms as yellow, PtO_x shaded red, and PtS_x shaded yellow). ^{195}Pt chemical shift parameters δ^{i}_{xx}, δ^{i}_{yy}, δ^{i}_{zz}, and δ_{iso} are descriptors of local ^{195}Pt bonding environments and indicated in the spectra, as well as tabulated in Tables 6.1 and 6.2. The principal axes system (*xx-yy-zz*) of the ^{195}Pt chemical shift tensor (δ^{i}_{xx}, δ^{i}_{yy}, and δ^{i}_{zz}) are shown in (a) and (c).

Table 6.1. ^{195}Pt chemical shift parameters and XPS analyses for α-PtO_2 and oxidized Pt-black surfaces.

Chemical Shift Tensor Parameters [ppm]				**Chemical Shift Anisotropy Parameters**				**XPS**	
Component "*i*"	δ^i_{xx}	δ^i_{yy}	δ^i_{zz}	δ^i_{iso} [ppm]	$\Delta\sigma$ [ppm]	η	% Area	Pt : O	% Pt
1	3300	3500	7700	4800	2900	0.08	82	1 : 2	73
2	NA	NA	NA	3800	1800	NA	18	1 : 1.3	27
I	NA	NA	NA	3800	1800	NA	100	1 : 1.3	37

in α-PtO_2. The disordered Pt oxide environment within α-PtO_2 (Figure 6.2a, inset sites 2), which has been represented using a Gaussian distribution with δ_{iso} found for surface oxides on Pt-black, is shifted to lower frequency (~3,800 ppm) as compared to δ_{iso} for α-PtO_2 (~ 4,800 ppm). A shift to lower ppm implies that the ^{195}Pt nuclei of disordered Pt oxide environments experience a smaller local magnetic field compared to ordered α-PtO_2 environments, an effect that is related to the stoichiometry, bond length, and electronic influence of O on Pt. Deconvoluted Pt:O stoichiometries and % contributions for each component measured by XPS and ^{195}Pt NMR are also tabulated in Table 1, which show that disordered α-PtO_2 environments and oxidized Pt-black surfaces have $PtO_{1.3}$ stoichiometry. A reduced PtO_2-like environment with fewer electron withdrawing O atoms nearby is consistent with the lower ^{195}Pt NMR frequencies of disordered Pt oxide environments. A disordered PtO_2-like hexagonal structure (Figure 6.2b) is consistent with previous observations[33] and also agrees with the XPS stoichiometry results.

A lineshape comparison between sulfidized Pt-black surfaces and PtS_2 (Fig. 6.2, Table 6.2) was used to deconvolute contributions from locally ordered and

Table 6.2. ^{195}Pt Chemical shift parameters for PtS_2 and sulfidized Pt-black surfaces

Chemical Shift Tensor Parameters [ppm]				**Chemical Shift Anisotropy Parameters**			
Component "i"	δ^i_{xx}	δ^i_{yy}	δ^i_{zz}	δ^i_{iso} [ppm]	$\Delta\sigma$ [ppm]	η	% Area
A	-4900	-4100	-100	-3000	2900	0.26	67
B	NA	NA	NA	-3800	1700	NA	22
C	NA	NA	NA	-2000	2500	NA	11
χ	NA	NA	NA	-2000	2500	NA	100

disordered ^{195}Pt sites in the solid-state NMR spectrum. With the inclusion of surface Pt sulfide resonances (Fig. 6.2d, sites χ) within the spectrum of PtS_2, the resulting lineshape (Fig. 6.2c) consists of an ordered component (A) with two underlying disordered components (B, C). The locally ordered component with axial symmetry (A) arises from the CdI_2 structure for PtS_2, similar to α-PtO_2, but with significantly more lattice defects as evidenced by additional broadening and larger η value (0.26 versus 0.08). The two disordered components (B and C) reflect the presence of locally disordered Pt sulfide environments, consistent with the lack of diffraction pattern for PtS_2. These disordered environments can be related to the structure of PtS_2 with respect to the ppm value of the chemical shift tensor components. As in the case of oxidized Pt-black surfaces, B sites in PtS_2 correspond to the highest intensities of locally ordered A sites, which indicate disordered PtS_2-like environments. However, unlike in the case for oxidized Pt-black surfaces, sulfidized Pt-black surfaces (Fig. 6.2d, χ sites) resonate closer to the out-of-plane δ^A_{zz} principle component (rather than in-plane δ^A_{xx} and δ^A_{yy}) of the chemical shift tensor for PtS_2 (Fig. 6.2c, sites A), which indicates the presence of disordered PtS-like environments

(C sites). Both the ppm position and correlation with the chemical shift tensor are consistent with a disordered PtS-like structure (Figure 6.2d).

6.3.3. Effect of oxidation on ^{195}Pt environments in Pt-SiO$_2$

With an understanding of how to distinguish between bulk and surface ^{195}Pt oxide and sulfide environments, ^{195}Pt distributions in Pt-SiO$_2$ revealed influences of nanoparticle size and support on local Pt electronic environments. The ^{195}Pt spectrum of oxidized Pt-SiO$_2$ (Fig. 6.3a) displays an extremely broad distribution (-6,000-10,000 ppm) of overlapping signals that reflect a combination of Pt oxide and support interaction environments. On the more positive ppm side of the spectrum, where bulk and surface ^{195}Pt oxides resonate, a distinct but very broadened signal can be observed for Pt-SiO$_2$. In fact, there appears to be a distribution of Pt oxide environments that consist of PtO$_2$-like and other surface Pt oxide environments, such as PtO-like and/or distributions of sub-oxide moieties. However, on the more negative ppm side of the spectrum, where bulk and surface ^{195}Pt sulfides resonate, a predominant and broadened signal is observed even without sulfidation of Pt-SiO$_2$. Given the lack of ^{195}Pt sulfides in the sample, the only explanation for the presence of these environments is SiO$_2$ interactions with Pt oxide nanoparticles. Recently, it was established that small Pt oxide nanoparticles interact strongly with colloidal SiO$_2$ surfaces that

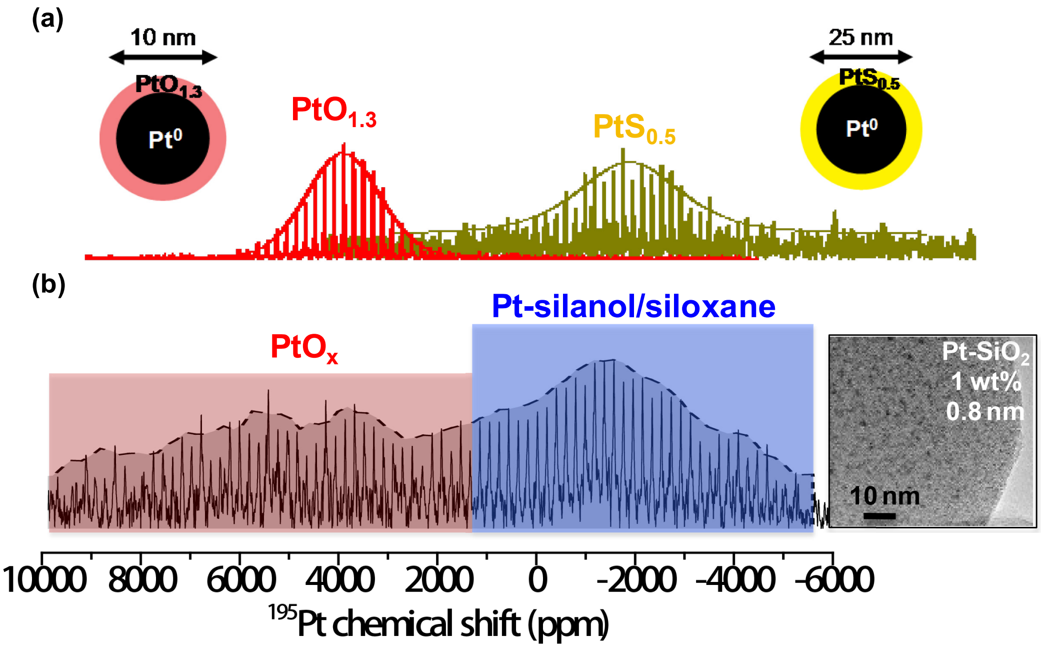

Figure 6.3. Solid-state ^{195}Pt WURST-CPMG NMR spectra of (a) oxidized and sulfidized Pt-black and (b) oxidized 0.8 nm Pt nanoparticles supported on SiO_2 (~1 wt% Pt). Red, yellow, and blue are used as color codes for Pt oxide, sulfide, and support environments, respectively. A TEM of $Pt-SiO_2$ is shown as an inset.

consisted of disordered silanol and siloxane moieties.[34] Similarly, highly disordered SiO_2 surfaces interacting with very small (~0.8 nm) Pt oxide nanoparticles resulted in a very broad (i.e., disordered) distribution of Pt-support interactions, as established from the ^{195}Pt NMR spectrum. Interestingly, while the similarity between $Pt-SiO_2$ and Pt sulfide environments is not initially obvious, trends in catalytic reactivity for these environments are also similar.[5,6,35,36] These paralleled similarities suggest that the sensitivity of ^{195}Pt NMR can enable molecular identification of local bonding environments that are influential during catalysis.

6.4. Conclusions

A recently advanced ^{195}Pt NMR method (WURST-CPMG), in combination with XRD and XPS, was implemented on bulk, surface, and supported Pt compounds (α-PtO_2, PtS_2, oxidized/sulfidized Pt-black and Pt-SiO_2) to establish the distributions of ^{195}Pt environments in these materials. While the highly ordered, CdI_2 layered structure was observed for α-PtO_2, the presence of locally disordered ^{195}Pt environments was also indicated. The locally disordered ^{195}Pt environments corresponded well with surface Pt oxides (~$PtO_{1.3}$) on Pt-black, a likely cause for c-axis (001) broadening in α-PtO_2. A comparison with PtS_2, a structural analogue of PtO_2, enabled electronic influences of S versus O on ^{195}Pt to be discerned. Although PtS_2 showed a much larger degree of local and long-range disorder, the ^{195}Pt environments were readily distinguishable and appeared very similar to a highly distorted CdI_2 environment and surface sulfides (~$PtS_{0.5}$) on Pt-black. With an understanding of how to distinguish bulk and surface ^{195}Pt oxides and sulfides, supported Pt on SiO_2 revealed influences of particle size and support effects on ^{195}Pt distributions. Smaller sized Pt nanoparticles resulted in broader distributions of ^{195}Pt oxide environments and predominant interactions with SiO_2 surfaces. Upon sulfidation, ^{195}Pt oxide and support interaction environments decrease while ^{195}Pt sulfide resonances increase. Clearly, solid-state ^{195}Pt NMR provides molecular level details that can distinguish differences and similarities between ^{195}Pt environments in heterogeneous Pt-containing materials, including supported nanoparticle catalysts.

These advancements in sensitivity and resolution of ^{195}Pt NMR spectra have enabled novel molecular signatures of unique Pt environments to be readily identified.

6.5. Acknowledgments

The work was conducted in the Central Facilities of the UCSB Materials Research Laboratory MRSEC Program of the NSF under Award No. DMR-1121053; a member of the NSF-funded Materials Research Facilities Network(www.mrfn.org). Use of the Central Facilities was supported by the U.S. National Science Foundation under Grant No. CHE-1059108. L.C.J thanks the NSF-IOSE-PIRE Program (0968399) and the NSF ConvEne IGERT Program (NSF-DGE 0801627) for fellowship support.

6.6. References

(1) Kweskin, S. J.; Rioux, R. M.; Habas, S. E.; Komvopoulos, K.; Yang, P.; Somorjai, G. A. *J. Phys. Chem. B* **2006**, *110*, 15920.

(2) Zhensheng, J. *Journal of Molecular Catalysis. A, Chemical* **2003**,*191*, 61.

(3) Olsson, L. *Journal of Catalysis* **2002**, *210*, 340.

(4) Sabourault, N.; Mignani, G.; Wagner, A.; Mioskowski, C. *Organic letters* **2002**, *4*, 2117.

(5) Thomas, V. D.; Schwank, J. W.; Gland, J. L. *Surface Science* **2000**, *464*, 153.

(6) Paál, Z.; Muhler, M.; Matusek, K. *Journal of Catalysis* **1998**, *175*, 245.

(7) Baldyga, L. M.; Blavo, S. O.; Kuo, C.-H.; Tsung, C.-K.; Kuhn, J. N. *ACS Catalysis* **2012**, 2626.

(8) McBride, J.; Graham, G.; Peters, C.; Weber, W. *Journal of Applied Physics* **1991**, *69*, 1596.

(9) Graham, G.; Weber, W.; McBride, J.; Peters, C. *Journal of Raman Spectroscopy* **1991**, *22*, 1.

(10) Xin, H.; Nikolla, E.; Miller, J.; Linic, S. *Topics in Catalysis* **2010**, *53*, 348.

(11) Ropo, M.; Kokko, K.; Vitos, L. *Physical Review B* **2005**, *71*, 045411.

(12) Abe, M.; Mori, S.; Nakajima, T. *Chemical Physics* **2005**, *311*, 129.

(13) Bowmaker, G.; Harris, R.; Assadollahzadeh, B.; Apperley, D.; Hodgkinson, P.; Amornsakchai, P. *Magnetic Resonance in Chemistry* **2004**, *42*, 819.

(14) Dmitrenko, O.; Bai, S.; Beckmann, P. A.; van Bramer, S.; Vega, A. J.; Dybowski, C. *The Journal of Physical Chemistry A* **2008**, *112*, 3046.

(15) Schreckenbach, G. *Inorganic chemistry* **2002**, *41*, 6560.

(16) Bush, A. A.; Gippius, A. A.; Zalesskii, A. V.; Morozova, E. N. *Journal of Experimental and Theoretical Physics Letters* **2003**, *78*, 389.

(17) Rhodes, H.; Wang, P.; Stokes, H.; Slichter, C.; Sinfelt, J. *Physical Review B* **1982**, *26*, 3559–3568.

(18) Still, B.; Kumar, P.; Aldrich-Wright, J.; Price, W. *Chemical Society Reviews* **2007**, *36*, 665.

(19) Garwood, M.; Delabarre, L. *Journal of Magnetic Resonance* **2001**, *153*, 155.

(20) Kupče, Ē.; Freeman, R. *Journal of Magnetic Resonance* **1995**, *117*, 246.

(21) Siegel, R.; Nakashima, T. T.; Wasylishen, R. E. *Concepts in Magnetic Resonance Part A* **2005**, *26*, 62.

(22) O'dell, L. A.; Rossini, A. J.; Schurko, R. W. *Chemical Physics Letters* **2009**, *468*, 330.

(23) MacGregor, A.; O'dell, L. A.; Schurko, R. W. *J. Magn. Reson*. **2011** *208*, 103.

(24) Massiot, D.; Fayon, F.; Capron, M.; King, I.; Le Calvé, S.; Alonso, B.; Durand, J.-O.; Bujoli, B., Gan, Z.; Hoatson, G. *Magnetic Resonance in Chemistry* **2002**, *40*, 70.

(25) Widdifield, C. M.; Schurko, R. W. *Concepts in Magnetic Resonance Part A* **2009**, *34*, 91.

(26) Fayon, F.; Bessada, C.; Massiot, D.; Farnan, I.; Coutures, J. P. *Journal of Non-Crystalline Solids* **1998**, *232,* 408.

(27) Mayell, J. S.; Longer, S. H. *Journal Of The Electrochemical Society* **1964**, *111*, 438.

(28) Hwang, C.-P.; Yeh, C.-T. *Journal of Molecular Catalysis. A* **1996***, 112*, 295.

(29) Finley, A.; Schleich, D.; Ackerman, J.; Soled, S. *Materials Research Bulletin* **1974**, *9*, 1655.

(30) Bucher, J. P.; Buttet, J.; Van Der Klink, J. J.; Graetzel, M.; Newson, E.; Truong, T. B. *Colloids and surfaces* **1989**, *36*, 155.

(31) Rozhdestvina, V. I.; Ivanov, A. V.; Zaremba, M. A.; Antsutkin, O. N.; Forsling, W. *Crystallography Reports* **2008**, *53*, 391.

(32) Tang, J. A.; Kogut, E.; Norton, D.; Lough, A. J.; McGarvey, B. R.; Fekl, U.; Schurko, R. W. *Journal Of Physical Chemistry B* **2009**, *113*, 3298.

(33) Salmeron, M.; Brewer, L.; Somorjai, G. A. *Surface Science* **1981**, *112*, 207.

(34) Giovanetti, L. J.; Ramallo López, J. M.; Foxe, M.; Jones, L. C.; Koebel, M. M.; Somorjai, G. A.; Craievich, A. F.; Salmeron, M. B.; Requejo, F. G. *Small* **2012**, *8*, 468.

(35) Rioux, R. M.; Hsu, B. B.; Grass, M. E.; Song, H.; & Somorjai, G. A. *Catalysis Letters* **2008**, *126*, 10.

(36) Rioux, R.; Hoefelmeyer, J.; Grass, M.; Song, H.; Niesz, K.; Yang, P.; Somorjai, G. A. *Langmuir* **2008**, *24*, 198.

Chapter 7

Bulk and surface ^{195}Pt environments in reduced Pt catalysts

---

Adapted from Journal of Physical Chemistry submission:

Louis C. Jones, Michael J. Gordon, and Bradley F. Chmelka

Abstract

Distributions of reduced ^{195}Pt environments in Pt-black and Pt nanoparticles supported on zeolite NaY (Pt-NaY) were probed using novel broadband NMR methodology. In combination with a homebuilt NMR probehead for operation at cryogenic temperatures, interior and surface ^{195}Pt site distributions were readily established for Pt-black and Pt-NaY. The enhanced resolution and sensitivity provide indications of unique electronic environments of Pt that may be influencing overall catalytic reactivity. Using ^{13}CO as a probe molecule, dynamic ^{195}Pt and ^{13}C NMR distributions revealed how surface diffusion evolves with temperature. These direct molecular level observations provide indications for altered catalytic properties.

7.1. Introduction

While much is known regarding properties that appear to influence the catalytic reactivity of supported Pt nanoparticle (NP) catalysts, origins of unique surface chemistry remain difficult to establish. This is due to the inherent heterogeneity of Pt environments in NP catalysts (e.g., terraces and steps,[1,2] kinks and defects,[3,4] and metal-support interactions[5,6]). Moreover, dynamic rearrangements can occur during reaction conditions, whereby adsorbate interactions cause surface reconstruction[7] and spill-over.[8] This complex scenario at molecular length-scales results in a convoluted picture of what governs catalytic properties. Surface-sensitive characterization techniques, capable of distinguishing differences between local molecular electronic environments, are necessary to decipher the molecular details that are responsible for overall reactivity.

Nuclear magnetic resonance (NMR) spectroscopy, a sensitive probe of the local molecular environments and structures of solid-state materials, has great potential for deconvoluting local molecular influences on Pt catalytic reactivity. However, despite the technological relevance of Pt-containing compounds and catalysts, the utilization of solid-state ^{195}Pt NMR on metallic remains a significant challenge. These challenges are presented by the enormous (>50,000 ppm) frequency range over which metallic ^{195}Pt NMR signals can be distributed (compared to ^{1}H (~20 ppm) and ^{13}C (~1,000 ppm)).[9] The vastness of the ^{195}Pt shift range reflects intrinsic sensitivity to local valence and conduction electron environments, which can be exploited to obtain detailed molecular information. However, there have been significant hardware limitations associated with exciting and detecting NMR signals over such broad spectral widths. Pioneering efforts by Slichter, Sinfelt, and coworkers in the 1980's used variable-magnetic-field measurements at 77 K and 4 K to investigate reduced Pt-alumina catalysts, acquiring quasi-continuous-wave ^{195}Pt NMR spectra point-by-point for linewidths that approached 3 MHz.[9-11] The low resolution of the resulting ^{195}Pt spectra and long measurement times have presented severe limitations for the use of ^{195}Pt NMR to characterize solid-state materials, in particular for heterogeneous nanoscale Pt catalysts.

Recent advancements have been made in the excitation of NMR spectra containing ultra-broad signals and have opened up new opportunities for investigations of ^{195}Pt environments in supported Pt catalysts and precursor species. Advanced radiofrequency (RF) swept NMR pulses can be applied to acquire broad ^{195}Pt NMR spectra adiabatically by exciting very large frequency ranges (~MHz) with lower power requirements than conventional solid-state NMR techniques.[12] Schurko and coworkers have recently demonstrated the use of these advanced methods to excite and acquire ^{195}Pt NMR spectra of crystalline materials with linewidths of ca. MHz.[13-15] This new and versatile approach is highly efficient for acquiring ultra-broad NMR spectra in far less time than previously possible and with improved sensitivity and resolution. However, these methods have yet to be applied to reduced Pt catalysts, in particular at cryogenic temperatures that are needed to observe fast relaxing metallic ^{195}Pt environments.

Herein, bulk and surface ^{195}Pt environments of metallic Pt catalysts were established using solid-state ^{195}Pt NMR at 77 K and 4 K. Implementation at cryogenic temperatures was achieved by constructing a transmission-line NMR probehead tuned to ^{195}Pt (~61-65 MHz at 7 T), which was continuously cooled with liquid N_2 and He in a vacuum-insulated dewar within the NMR magnet. Using these advanced methods, distinct ^{195}Pt distributions were readily established in Pt-black and Pt NPs supported on zeolite NaY (Pt-NaY). Introduction of CO and CO_2 as probe molecules enabled discrete signals from surface ^{195}Pt ensembles to be readily distinguished and monitored as a function of temperature. Changes in CO and CO_2 adsorption with particle size and temperature were additionally corroborated using solid-state ^{13}C NMR. It can be shown that ^{195}Pt distributions are correlated with previously measured catalytic reactivity, highlighting the sensitivity of solid-state ^{195}Pt NMR towards differences in local valence and conduction electron environments.

7.2. Experimental Section

Oxidized samples of Pt-black (Sigma Aldrich) were treated with O_2 at 120 ^{o}C, while in a separate reactor, sulfidized samples were treated with H_2 at 120 ^{o}C for 30 min and S_8 at 120 ^{o}C for 1 h. Pt NaY samples were prepared by ion-exchanging $Pt(NH_3)_4Cl_2$ with zeolite NaY at 60 ^{o}C. The resulting powder was washed with NaOH and H_2O several times before drying overnight. Oxidized samples were prepared by flowing O_2 while heating to 400 ^{o}C over a 5 h period. In a separate reactor, sulfidized samples were prepared by first oxidizing, followed by cooling to 298 K, then flowing H_2 while heating to 400 ^{o}C over a 5 h period, and finally exposing S_8 at 120 ^{o}C for 1 h.

CO/CO_2 adsorptions were performed by first calcining and reducing Pt-black and Pt-NaY, followed by evacuation (~5 mTorr) at 100 ^{o}C and then exposure to ^{13}CO and $^{13}CO_2$ with subsequent cooling to 298 K. Remaining gas-phase and physisorbed CO/CO_2 were desorbed by evacuation at 298 K. Samples were transferred into a dry glovebox, packed into a 7mm rotor, and sealed with a viton o-ring cap.

Solid-state ^{195}Pt WURST-CPMG NMR spectra were acquired at 7.06 T on a Bruker AVANCE NMR spectrometer operating at 300.07 and 64.49 MHz for ^{1}H and

^{195}Pt, respectively, with parameters optimized according to previous work.[13-15] WURST-CPMG pulses of 50 μs (~2 MHz) were applied at center frequencies of 64.72 and 64.28 MHz using forward and reverse frequency sweeps to compensate for transverse relaxation of ^{195}Pt magnetization during the sweeps.. An acquisition time of 80 μs was used to measure the free induction decays of each subsequent CPMG loop (12 total) with recycle delays of 0.5 s. Fourier transformed spectra for the two center frequencies were co-added after a magnitude calculation to produce the observed ^{195}Pt spikelet patterns with a span of >1 MHz. Lineshapes were constructed from interpolated skyline projections (spikelet integration) of each CPMG spikelet pattern.

X-ray photoelectron spectra (XPS) were measured using a Kratos Axis Ultra system with a monochromated Al K_α source (1486.6 eV, 225 W). An electron flood gun was used for charge neutralization to compensate for the non-conducting samples. All samples were referenced to surface carbonaceous species (284.7 eV).

X-ray diffraction (XRD) patterns were measured using a Philips X'Pert MPD with a 3kW Cu K_α (1.5405 Å) X-ray source.

7.3. Solid-state ^{195}Pt NMR Methodology

7.3.1. Wideband adiabatic excitation

The use of wideband adiabatic excitation methods can alleviate the difficulties of acquiring 50,000 ppm wide ^{195}Pt NP line-shapes. High power, non-adiabatic (i.e., constant frequency) conventional RF pulses that are required to excite such large ppm ranges can easily damage NMR hardware components, limiting the excitation bandwidth of conventional RF excitation to only 1,000-2,000 ppm, as depicted in Figure 7.1a. Recent advancements in NMR hardware and software now permit precise manipulation of RF pulses, a necessary component for the implementation of adiabatically (slowly) swept pulses (i.e., variable frequency) that can uniformly excite nuclei over large ppm ranges with low peak powers.[12] Figure 7.1b shows the range and profile of a specific type of adiabatic pulse called WURST (*w*ide-band *u*niform-*r*ate *s*moothed *t*runcation), which sweeps a 15,000 ppm range with uniform excitation profiles to allow facile co-addition of sub-spectra over the entire 50,000 ppm ^{195}Pt NMR line-shapes. This type of RF pulse can be generally applied to a variety of nuclei with large NMR shift ranges, the theory of which is detailed below.

The adiabatic rapid passage theorem states that the nuclear magnetization will follow the effective field as long as the condition $\gamma B_{eff} >> d\alpha/dt$ holds, where γB_{eff} is the effective frequency and $d\alpha/dt$ is the angular velocity at which the B_{eff} field rotates.[16] This can be visualized and proven classically utilizing a rotating-frame coordinate system (Fig. 7.2). For an arbitrary function, $F(t) = F_x(t)\hat{i} + F_y(t)\hat{j} + F_z(t)\hat{k}$, in a coordinate system rotating with angular velocity Ω, the time derivative of the normal coordinates $r = \{\hat{i}, \hat{j}, \hat{k}\}$ and $F(t)$ are given by:

$$\frac{dr}{dt} = \Omega \times r \qquad (1),$$

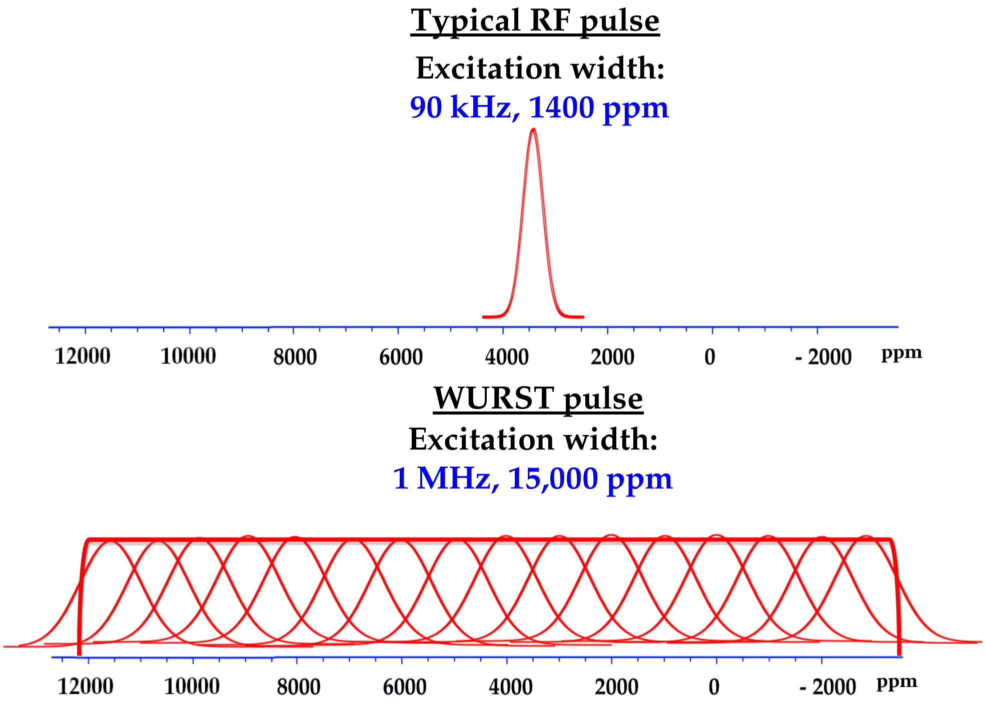

Figure 7.1. A comparison between the excitation bandwidth of (a) typical RF pulses and (b) adiabatically swept WURST pulses that shows an order of magnitude increase in excitation range.

$$\frac{dF}{dt}=\frac{dF_x}{dt}\hat{i}+F_x\frac{d\hat{i}}{dt}+\frac{dF_y}{dt}\hat{j}+F_y\frac{d\hat{j}}{dt}+\frac{dF_z}{dt}\hat{k}+F_z\frac{d\hat{k}}{dt}$$

$$=\frac{dF_x}{dt}\hat{i}+\frac{dF_y}{dt}\hat{j}+\frac{dF_z}{dt}\hat{k}+\Omega\times(F_x\hat{i}+F_y\hat{j}+F_z\hat{k})$$

$$=\frac{\delta F}{\delta t}+\Omega\times(F) \qquad (2).$$

The corresponding equations of motion describing a magnetic moment, μ, with angular momentum, J, in an applied magnetic field, B_0, rotating in a coordinate system with angular velocity, Ω, is shown by:

$$\frac{dJ}{dt} = \mu \times B_0 \qquad (3),$$

$$\mu = \gamma J \qquad (4),$$

$$\frac{d\mu}{dt} = \mu \times \gamma B_0 \qquad (5),$$

$$\frac{\delta\mu}{\delta t} + \Omega \times \mu = \mu \times \gamma B_0 \qquad (6),$$

$$\frac{\delta\mu}{\delta t} = \mu \times (\gamma B_0 + \Omega) \qquad (7).$$

As seen in by the final expression, in the rotating-frame of reference shown in Figure 7.2, μ experiences an effective field $B_{eff} = B_0 + \Omega/\gamma$. If one allows Ω to be $-B_0\gamma$, B_{eff} becomes zero and $\delta\mu/\delta$t is invariant with respect to the rotating frame.

Application of a conventional RF pulse, $B_1(t) = B_1(\mathrm{Cos}(\omega_z t)\ \hat{i} + \mathrm{Sin}(\omega_z t)\ \hat{j})$, in the rotating-frame results in the following expressions for μ:

$$\frac{\delta\mu}{\delta t} = \mu \times [(\omega_z + \gamma B_0)\hat{k} + \gamma B_1 \hat{i}] \qquad (8),$$

$$\frac{\delta\mu}{\delta t} = \mu \times \gamma[(B_0 - \omega_z / \gamma)\hat{k} + B_1 \hat{i}] \qquad (9).$$

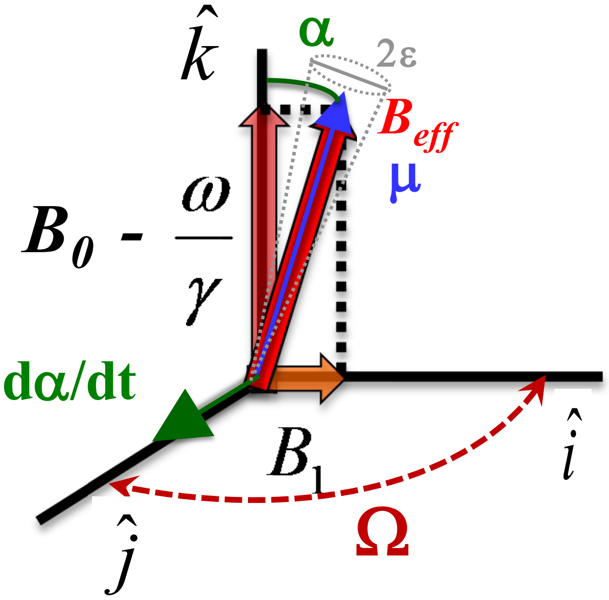

Figure 7.2. A generalized NMR coordinate system rotating with angular frequency, Ω, showing net sample magnetization, μ, precessing with angle 2ε, along an applied magnetic field, $B_{eff} = (B_0 - \omega/\gamma)\hat{k} + B_1\hat{i}$, that is being varied at a rate of dα/dt. In typical NMR experiments, $\omega = \gamma B_0$ is constant. In adiabatic NMR experiments, $\omega(t) = \gamma B(t)$ and varies in time.

When the frequency of the RF pulse and the rotating frame approach the Larmor frequency, γB_0, the effective field becomes $B_1\hat{i}$ and μ rotates from the $\hat{k}$-direction to the $\hat{i}$ - $\hat{j}$ plane. Once the RF pulse is turned off, the magnetization precesses about B_0 producing an induced voltage signal in the magnetic coil, which can be Fourier transformed to obtain frequencies of absorption, expressed in units of ppm. This is the typical scenario of most NMR experiments, with the inclusion of additional pulses for more complex manipulation of the magnetization, allowing selective filtering of desired molecular interactions.

The alternative to a conventional RF pulse would be to vary the amplitude and frequency of the pulse as a function of time. This can be visualized using Figure 7.2, showing how $B_{eff}(t)=(B_0-\omega(t)/\gamma)\hat{k}+B_1(t)\hat{i}$ can be made time-dependent. The adiabatic condition may be understood by entering the B_{eff} frame. As the B_{eff} field rotates about angle, α, an additional magnetic field, $d\alpha/dt$, is produced in the $\hat{j}$ direction. The magnetization, μ, will precess about B_{eff}, making a cone of angle 2ε as rotation to the $\hat{i}$ - $\hat{j}$ plane occurs. This angle and condition for adiabatic inversion is given by:

$$\tan(\varepsilon)=\frac{[(d\alpha/dt)/\gamma]}{B_{eff}(t)} \qquad (10),$$

$$\tan(\varepsilon)=\frac{[(d\alpha/dt)/\gamma]}{B_{eff}(t)}<<1 \qquad (11),$$

$$d\alpha/dt<<\gamma B_{eff}(t) \qquad (12).$$

As seen, the adiabatic condition can be satisfied so long as the rate of change of B_{eff} is much slower than the instantaneous Larmor frequency, γB_{eff}. This condition is the basis by which amplitude- and frequency-modulated pulses can be developed and optimized. These equations allow one to develop and optimize modulation functions (i.e., shaped pulses) for $\omega(t)$ and $B_1(t)$, thereby maintaining an equivalently satisfied adiabatic condition throughout the entirety of the frequency sweep, known as offset-independent adiabaticity. For practical purposes, it is desirable to have a constant frequency sweep rate and RF amplitude over a large portion of the sweep width, with a deviation only towards the beginning and end of the sweep. Under these conditions, all spins within the central sweep region will experience an equivalent trajectory of magnetization.[17] A promising candidate for this type of inversion is the *wideband*, *uniform rate, smooth truncation* (WURST) amplitude profile, given by:

$$\omega_1(t) = \omega_{1\max}\{1 - |\sin(\beta t)|^n\} \qquad (13).$$

This name corresponds to the stretched amplitude profile shown in Figure 7.1b, which can be contrasted to the Gaussian profile shown in Figure 7.1a. So long as offset-independent adiabadicity is satisfied, n, β, and $\omega_{1\max}$ can be optimized to achieve uniform excitations over a very large (1 MHz, ~ 15,000 ppm for ^{195}Pt at 7.06 T) frequency range. In conjunction with a Carr-Purcell-Meiboom-Gill (CPMG) train of RF pulses to enhance signal acquisition,[18] WURST-CPMG pulse sequence (Fig. 7.3) can be applied to any nuclei and offers a 10-fold increase in broadband excitation and signal sensitivity over conventional RF pulses.

A comparison between α-PtO_2 spectra (Fig. 7.4) acquired under the same conditions using typical RF pulses and WURST-CPMG sweeps demonstrate the large increase in excitation bandwidth and signal sensitivity. A typical RF pulse excites only a small portion of the α-PtO_2 line-shape at 3,300 ppm and 6,000 ppm, but a single WURST sweep excites the entire line-shape. An accurate reproduction the WURST acquired line-shape would require several (> 40) point-by-point spectra using conventional RF pulses, which would still be limited in resolution due to the uncertainty in the co-addition of sub-spectra. Integration and interpolation of individual spikelets of the WURST-CPMG spikelet pattern provides the actual spectral lineshape composed of a distribution of ^{195}Pt environments. The application of WURST sweeps clearly provide a new avenue for obtaining accurate, high-resolution ^{195}Pt NMR line-shapes with faster acquisitions. The WURST-CPMG methodology is limited to static samples and its effectiveness depend upon properties of the sample, such as the width of the lineshape, as well as the length and distribution of relaxation times (see next section). Ideal samples have very large chemical shift distributions with similar and long transverse relaxation times (T_2), but with short inhomogeneous transverse relaxation times (T_{2inhom}).[19] Samples with narrow resonances and long T_{2inhom} times would not benefit from the application of WURT-CPMG. Signal relaxation that occurs during the WURST-CPMG pulses can be compensated for by performing experiments that sweep in increasing and decreasing frequency directions. As will be demonstrated further, this new methodology enables previously obscured molecular environments of bulk and surface Pt atoms to be distinguished and elucidated.

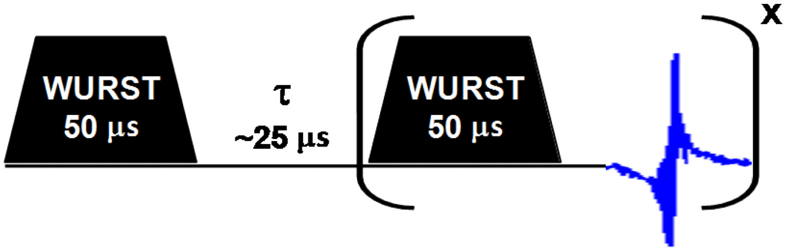

Figure 7.3. WURST-CPMG pulse sequence showing a 50 μs WURST sweep, followed by a delay of 25 μs, and subsequently X (e.g., 10-100) loops of 50 μs WURST sweeps with digital signal acquisition in between.

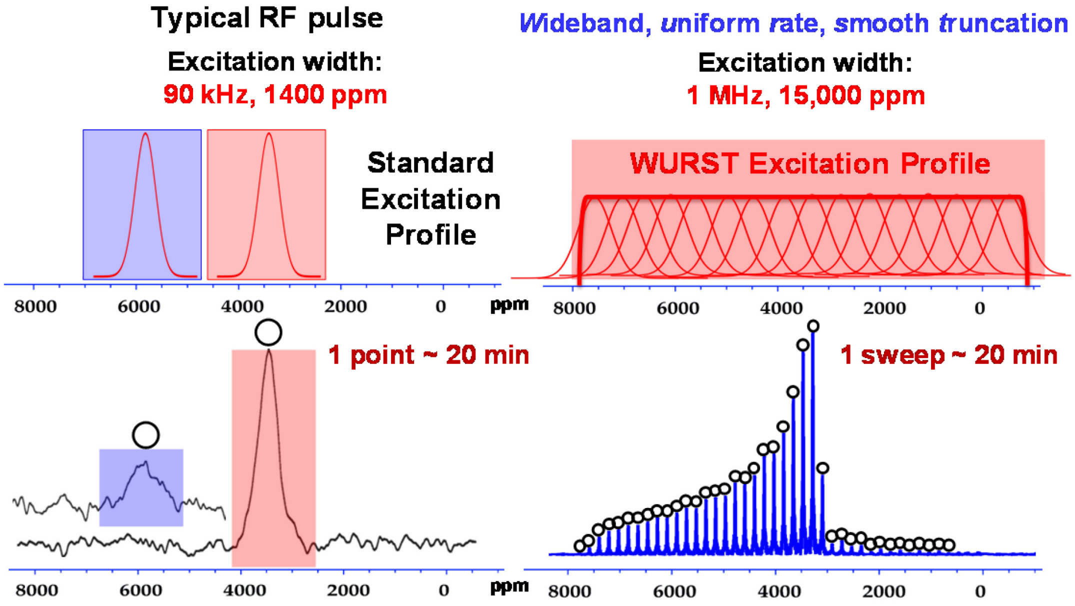

Figure 7.4. Solid-state ^{195}Pt NMR spectra of bulk α-PtO_2 acquired using (a) standard RF pulses to acquire a 2-point spectrum (centered at 3,300 and 6,000 ppm) and (b) a single swept WURST-CPMG pulse. Excitation profiles are shown below each spectrum.

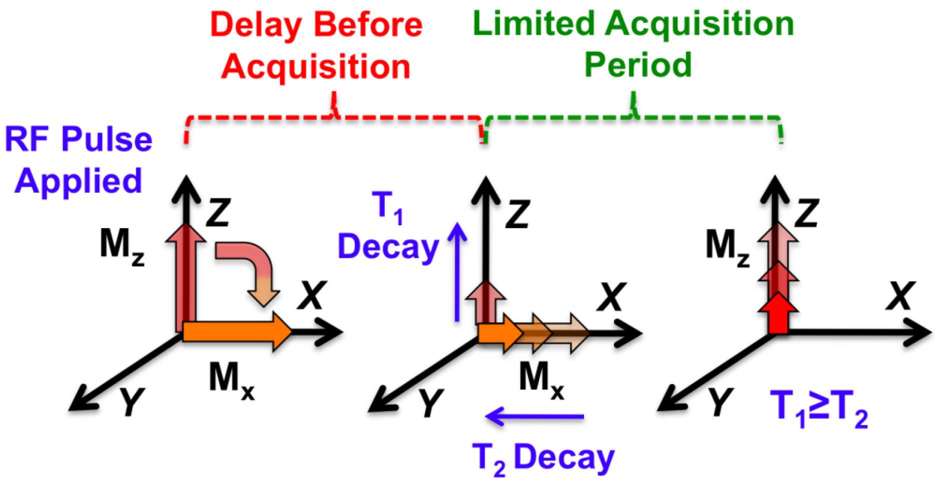

Figure 7.5. Progression of magnetization (M_z and M_x) in an NMR experiment showing resonant excitation (i.e., rotation) of M_z to the x-y plane producing a detectable signal, M_x. A limited signal acquisition period ensues, which is determined by relaxation times, T_1 and T_2. T_1 reflects the time it takes a material to establish its equilibrium magnetization (M_z), and T_2 reflects the decay time of detectable in-plane magnetization (M_x).

7.3.2. Signal Relaxation and Temperature Effects

Conduction electron interactions with ^{195}Pt nuclei, which are responsible for the large frequency shifts (i.e., Knight shifts[20]) of metallic Pt compounds, cause rapid relaxation of NMR signals. Signal relaxation (Fig. 7.5) is characterized by two distinct times, T_1 and T_2, which indicate the rate at which z and x components of magnetization, M_z and M_x, return back to equilibrium via energy exchange mechanisms, respectively. In the NMR experiment, a magnetic field is applied along the z-axis resulting in net sample magnetization, M_z, aligned with the magnetic field.

M_z is then rotated to the x-y plane by a resonant RF pulse to create M_x, which is recorded as an alternating voltage that can be Fourier transformed to produce an NMR spectrum. However, immediately after the RF pulse, M_x begins to decay to zero while M_z grows back to its equilibrium state with time constants T_2 and T_1, respectively. After M_x has decayed to zero, signal acquisition is no longer possible and M_z must return to its equilibrium magnetization before the process can be repeated (i.e., $T_2 \leq T_1$). Materials with short T_1 and T_2 result in signals that relax quickly and require extensive signal averaging to obtain reasonable signal-to-noise. In metals, T_1 and T_2 are extremely short (~10 - 100 of μs at 298 K) due to the same Fermi contact interactions that cause very large Knight shifts. A theoretical treatment can be used to relate Knight shifts in ^{195}Pt to T_1 and temperature (i.e., Korringa relation):[16]

$$T_1 \cdot T = 30 \text{ ms} \cdot \text{K} \qquad (14).$$

Decreasing temperature results in longer ^{195}Pt T_1 (and T_2) relaxation times, which increases the period of time when signal acquisition can occur. Moreover, this linear temperature dependence is only observed in conducting systems, making it a definitive test for the presence of conduction electrons.

Decreasing temperature, in addition to increasing ^{195}Pt relaxation times, results in a larger Boltzmann spin-population difference and enhanced NMR signal sensitivity. The distribution of spin-states in N_{upper} and N_{lower} energy states can be described by the Boltzmann equation:[16]

$$\frac{N_{upper}}{N_{lower}} = e^{\frac{-h\nu}{kT}} \quad (15).$$

Thus, the lower the temperature, the larger the spin-state population difference and adsorption of RF energy. At cryogenic temperatures of liquid N_2 (77 K) and He (4.2 K), NMR signal sensitivity increases a factor of 4 and 71, respectively. However, continuous cryogenic operation required mass-flow and temperature control of a homebuilt, thermally isolated, low temperature NMR probehead within the bore of a shielded superconducting magnet, the details of which are outlined in the following section.

7.3.3. Cyrogenic Probehead Design

Construction of a low temperature ^{195}Pt NMR probehead was carried out for the application of WURST-CPMG pulses at cryogenic temperatures (77 K and 4.2 K). The NMR probehead consisted of a transmission-line design (Fig. 7.6) commonly used for cryogenic experiments,[21,22] with a stainless steel outer conductor (~ 3' length, 2" diameter), a brass inner conductor (3' length, 0.625" diameter), and a copper solenoid sample coil (7 mm inner diameter, 0.036" gauge wire, 9 turns). Teflon spacers (0.25" length, 1.9" diameter) were used to isolate the inner and outer conductors. Variable capacitors were placed at the top (~10-50 pF) and bottom (~0.5-10 pF) of the transmission line to optimize tuning and matching conditions for efficient RF energy transfer to the sample coil. Isolation from the room temperature environment was achieved using a vacuum-insulated cryogenic dewar with a

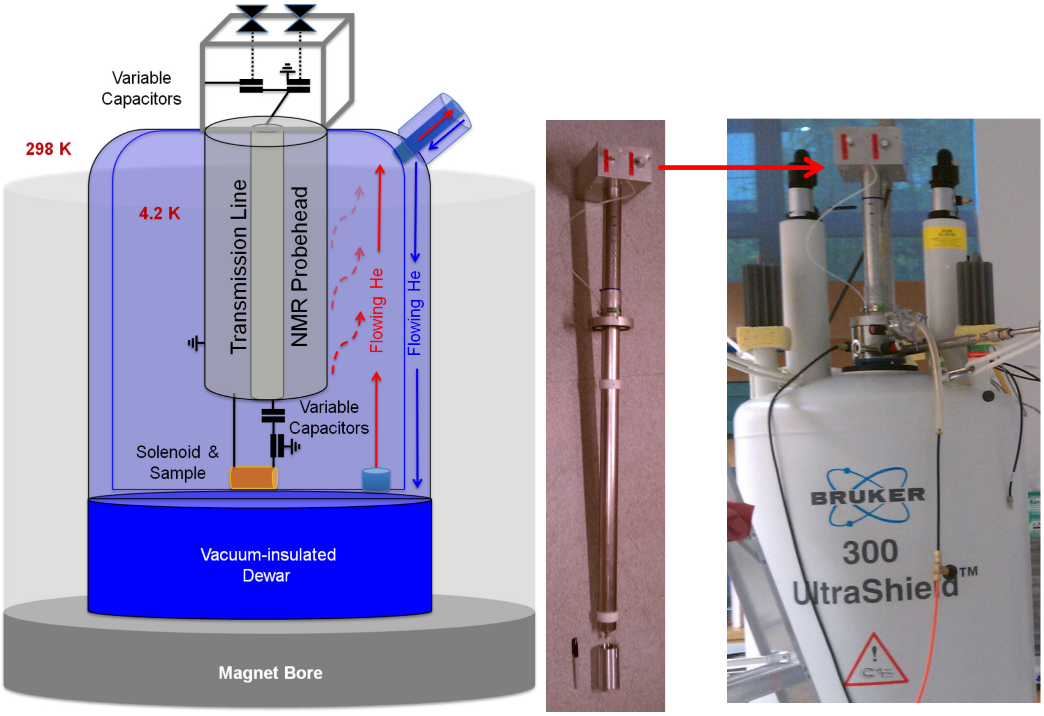

Figure 7.6. Schematic of a dewar-insulated, liquid He cooled, transmission line NMR probehead consisting of a stainless steel outer conductor, a brass inner conductor, and a copper solenoid sample coil. Variable capacitors are placed above and below the transmission line to optimize tuning and matching conditions for efficient RF energy transfer to the sample coil. Photographs of actual probe, solo and in the bore of a 7 T Bruker Superconducting Magnet in the CNSI at UCSB.

temperature sensor and mass-flow controlled transfer line (Oxford Instruments) for continuous delivery of liquid He and N_2 under slight vacuum (100's of mBar). The transmission line probehead was o-ring sealed (viton) to the dewar throudgh a circular aluminum plate (1" length x 5" diameter), and an o-ring sealed polycarbonate plug (1" length x 2" diameter) was used to cap the room temperature end of the transmission line.

7.4. Results and Discussion

7.4.1. Metallic Pt Environments

The effects of conduction electrons on distributions of ^{195}Pt environments in a bulk Pt powder sample were established using WURST-CPMG NMR and the homebuilt transmission line probehead at 298 K and 4.2 K. At 298 K, metallic Pt powder signals cannot be observed after 12 hours of acquisition (Fig. 7.7a), due to the very short T_1 (~100 μs) relaxation time. Typically, delays of 30-50 μs are required after RF pulses are applied to avoid electrical interference with signal acquisition, during which time ~ 83% of ^{195}Pt^0 signal has decayed and cannot be detected. However, after cooling the Pt powder to 4.2 K, a characteristic metallic ^{195}Pt resonance appears at -39,000 ppm after 20 minutes of acquisition (Fig. 7.7b). As detailed above, cooling the sample has two effects: (1) the T_1 relaxation time of Pt^0 increased to ~7 ms according to the Korringa relation (eqn. 14), and (2) the population difference between spin-states increased according to the Boltzmann expression (eqn. 15). The

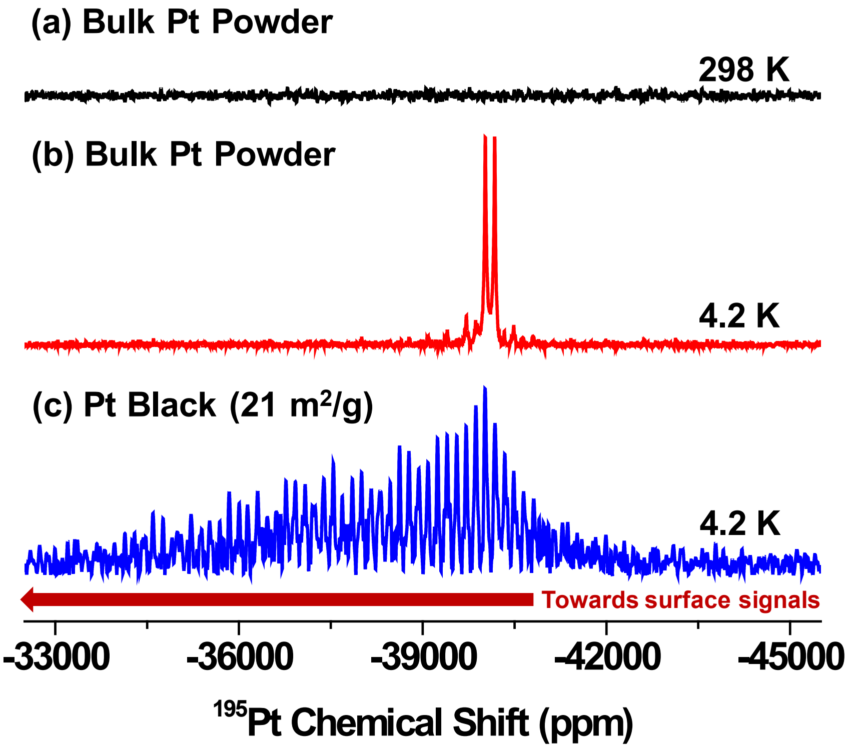

Figure 7.7. Solid-state ^{195}Pt WURST-CPMG NMR spectra of bulk Pt powder acquired at (a) 298 K and (b) 4.2 K, and Pt-black acquired at (c) 4.2 K.

combination of these two effects results in a very large ^{195}Pt signal that reflects a narrow distribution of locally-ordered metallic environments.

A solid-state ^{195}Pt WURST-CPMG NMR comparison between the bulk Pt powder and a high surface area Pt-black sample (21 m^2/g) at 4.2 K (Fig. 7.7) shows the influence of surface Pt environments on interior conduction electron environments. In contrast to the very narrow spectrum of the Pt powder (Fig. 7.7b), Pt-black (Fig. 7.7c) shows a much broader distribution of ^{195}Pt environments that extend towards more positive ppm values, where surface ^{195}Pt signals are known to resonate. The Knight shift is known to depend on the average conduction electron density, which varies from its bulk value in the interior to a semi-conducting regime at the surface of Pt.[20] Thus, as particle size decreases, surface effects become more prominent, and interior environments become less bulk-like. These characteristics are readily observed for the spectrum of Pt-black, which shows the presence of a bulk-like metallic ^{195}Pt environment with a significant distribution of environments that experience a smaller average electron density. Even for the relatively large particle sizes of Pt-black (~10-25 nm sintered grains), interior Pt atoms are no longer bulk-like. Deviations from bulk Pt conduction electron density can provide indications that surface Pt environments are contributing more strongly to the overall electronic structure of Pt particles.

7.4.2. Surface Pt Environments

Surface oxides and sulfides on Pt-black were measured to establish the influence of surface composition on distributions of ^{195}Pt environments. As previously demonstrated, Pt-black (Fig. 7.7c) shows the presence of metallic ^{195}Pt environments at -39,000 ppm, with additional signal intensity that extends towards more positive ppm values. A zoomed out view of the entire ^{195}Pt ppm range (Fig 7.8) shows that metallic Pt^0 signals arise from interior environments of Pt-black particles, while more positive ppm values correspond to surface environments. Specifically, oxidized

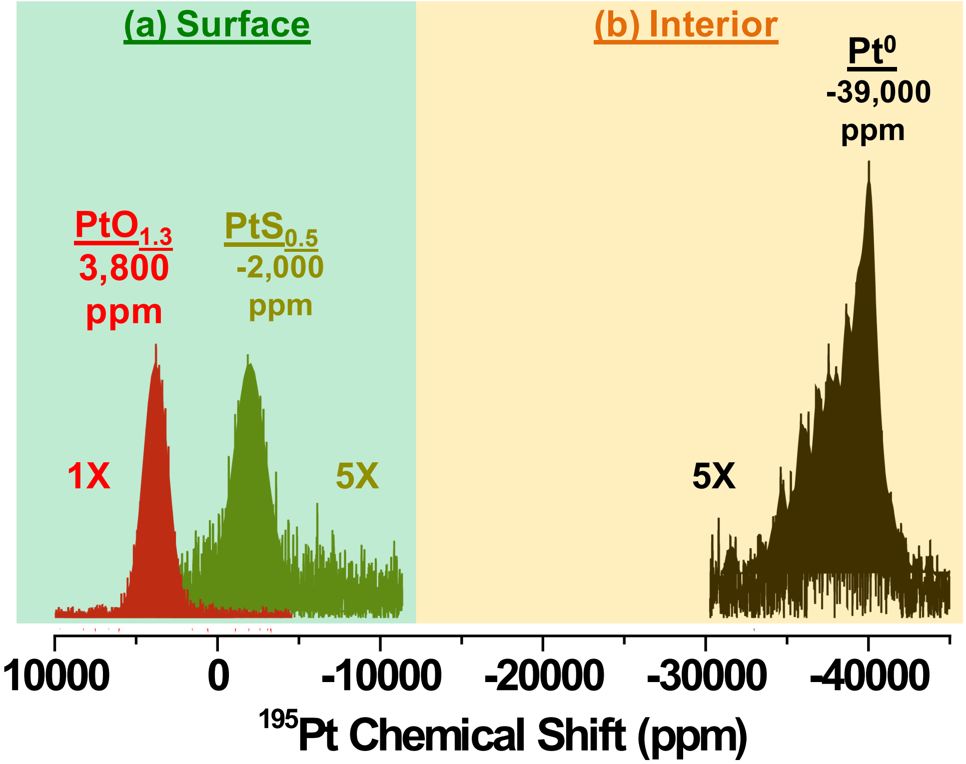

Figure 7.8. Solid-state ^{195}Pt WURST-CPMG NMR spectra of Pt-black (a) surface (shaded green, $PtO_{1.3}$ and $PtS_{0.5}$) and (b) interior (shaded blue, Pt^0) environments.

oxidation states of very different chemical environments (e.g., $PtO_{1.3}$ and $PtS_{0.5}$) are oftentimes similar. Being able to distinguish the molecular origins of unique Pt catalytic reactivity necessarily requires sensitivity to variations in local conduction and valence electron environments, which can be readily assessed using solid-state WURST-CPMG ^{195}Pt NMR.

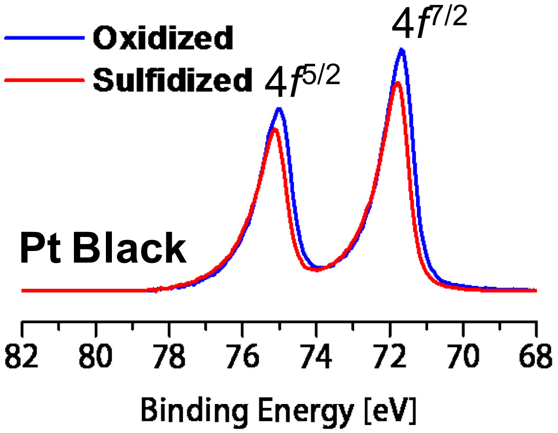

Figure 7.9. Pt 4*f* XPS spectra for oxidized (blue line) and sulfidized (red line) Pt-black. Due to the broad distribution of several overlapping Pt nanoparticle environments (i.e., PtO_x, PtS_x, Pt^0), lineshape deconvolutions were not confidently established.

7.4.3. Influence of CO adsorption

CO adsorption enabled measurements of surface ^{195}Pt ensembles and provided information regarding distributions of terrace, step, and defect sites on Pt-black surfaces. CO is well known for its ability to strongly bind to Pt surfaces, which is initiated by the carbon σ-orbital and further reinforced by "back- bonding" of surface Pt electrons to the oxygen π-orbital.[23,24] Due to these molecular interactions between CO and Pt, adsorption is highly dependent upon surface Pt coordination and electronic structure.

Conduction electrons also interact through Fermi contact with adsorbed ^{13}CO, which can be observed as a Knight shift in solid-state ^{13}C NMR spectra. Knight-shifted ^{13}CO signals (Fig. 7.12, 200-800 ppm) are far beyond the typical range of ^{13}C species (-200-200 ppm). At 298 K, the distribution of adsorbed ^{13}CO environments is very broad, indicative of surface diffusion occurring on Pt. The narrower components from -200-200 ppm are attributed to the fluorocarbon sample housing, the viton o-ring used to seal the sample, and gas-phase CO_2.[25,26] The generation of CO_2 may come from the reduction of residual surface Pt-oxides, the presence of H_2O causing water-gas shift, or CO disproportionation. A comparison with adsorbed $^{13}CO_2$ on Pt-NaY shows a similar Knight-shifted ^{13}CO spectrum with a much larger $^{13}CO_2$ component at ~124 ppm (Fig. 7.12). ^{13}CO is likely generated from dissociative $^{13}CO_2$ adsorption and/or small amounts of reverse water-gas shift reaction, both of which are consistent with a smaller center of mass position for Knight-shifted ^{13}CO (390 ppm vs. 415 ppm). A shift to lower ppm indicates a reduction in conduction electron spin density at the surface of Pt, suggestive that ^{13}CO is competitively adsorbed with another molecule (i.e., H_2O, OH, O).

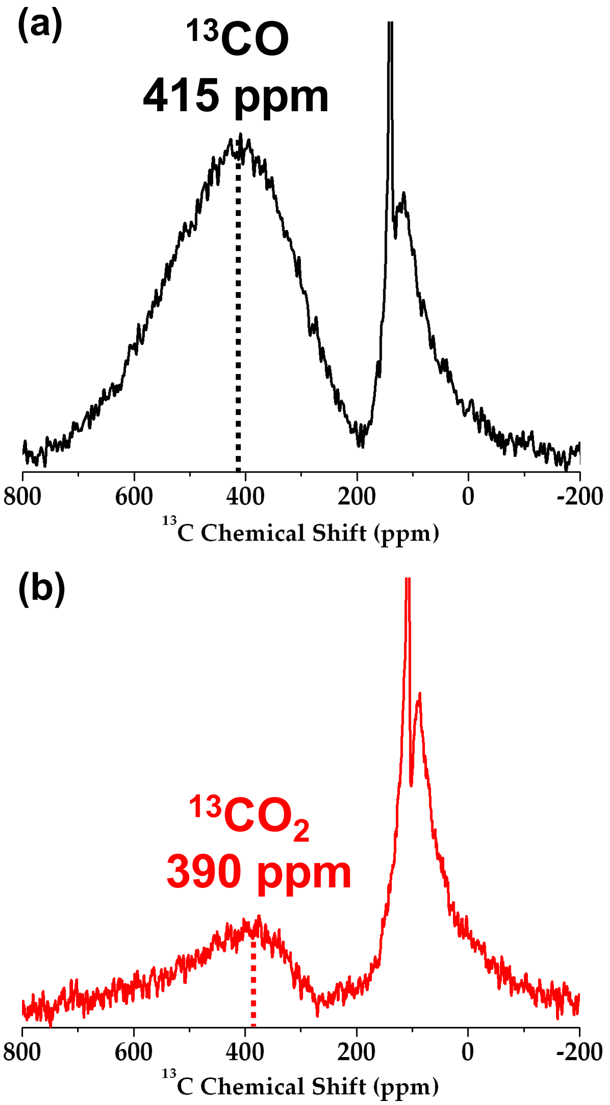

Figure 7.12. Solid-state ^{13}C NMR spectra (298 K) of (a) ^{13}CO and (b) ^{13}CO$_2$ adsorbed on Pt-NaY zeolite (2-5 nm , 15 wt%). Adsorbed ^{13}CO is located from 800-200 ppm. Signals from 200 to -200 ppm are attributed to the fluorocarbon sample housing, viton o-ring sample cap, and gas-phase CO$_2$.

7.5. Conclusions

Recently advanced solid-state ^{195}Pt WURST-CPMG NMR methods provided enhanced sensitivity and resolution enabling novel identification of chemically distinct Pt atoms in interior and surface environments. A homebuilt transmission line NMR probe was constructed for continuous cryogenic ^{195}Pt NMR measurements down to 4 K. Cryogenic temperatures lengthened signal relaxation times so that interior metallic environments within bulk Pt powder and Pt Black could be practically interrogated, which showed how the influence of surface species strongly affects interior Pt atoms. Solid-state ^{13}C NMR of ^{13}CO and $^{13}CO_2$ exposed to Pt-NaY showed the presence of both adsorbed CO and gas-phase CO_2. The interactions between CO and surface Pt atoms caused large ^{13}C shift values (i.e., Knight shifts) characteristic of conductive carbons. Moreover, these large shifts seen after CO_2 adsorption indicates that the CO oxidation reaction is reversible, but is likely poisoned by CO that cannot desorb until high temperatures, where CO_2 does not adsorb appreciably.

7.6. Acknowledgements

Experiments were conducted in the Central Facilities of the UCSB Materials Research Laboratory MRSEC Program of the NSF under Award No. DMR-1121053; a member of the NSF-funded Materials Research Facilities Network(www.mrfn.org). Use of the Central Facilities was supported by the U.S. National Science Foundation under Grant No. CHE-1059108. L.C.J thanks the NSF-

IOSE-PIRE Program (0968399) and the NSF ConvEne IGERT Program (NSF-DGE 0801627) for fellowship support.

7.7. References

(1) Jones, L. C.; Gordon, M. J.*The Journal of Physical Chemistry C* **2012**, *116*, 23472.

(2) Lundwall, M. J.; McClure, S. M.; Goodman, D. W. *J. Phys. Chem. C* **2010**, *114*, 7904.

(3) Somorjai, G. A.; Park, J. Y. *Chemical Society Reviews* **2008**, *37*, 2155.

(4) Zaera, F.; Somorjai, G. *Langmuir* **1986**, *2*, 686.

(5) Baker, L. R.; Kennedy, G.; Van Spronsen, M.; Hervier, A.; Cai, X.; Chen, S.; Wang, L.-W.; Somorjai, G. A. et al. *Journal of the American Chemical Society*, *134*, 14208.

(6) Yamada, Y.; Tsung, C.-K.; Huang, W.; Huo, Z.; Habas, S. E.; Soejima, T.; Aliaga, C. E.; Somorjai, G. A.; Yang, P. *Nature Chemistry* **2011**, *3*, 372.

(7) Tao, F.; Dag, S.; Wang, L.-W.; Liu, Z.; Butcher, D.; Bluhm, H.; Salmeron, M.; Somorjai, G. A. *Science* **2010**, *327*, 850.

(8) Stuckert, N. R.; Wang, L.; Yang, R. T. *Langmuir* **2010**, *26*, 11963.

(9) Rhodes, H.; Wang, P.; Stokes, H.; Slichter, C.; Sinfelt, J. *Physical Review B* **1982**, *26*, 3559.

(10) Rhodes, H.; Wang, P.; Makowka, C.; Rudaz, S.; Stokes, H.; Slichter, C.; Sinfelt, J. *Physical Review B* **1982**, *26*, 3569.

(11) Stokes, H.; Rhodes, H.; Wang, P.; Slichter, C.; Sinfelt, J. *Physical Review B (Condensed Matter)* **1982**, *26*, 3575.

(12) Garwood, M.; Delabarre, L. *Journal of Magnetic Resonance* 2001, *153*, 155.

(13) MacGregor, A.; O'dell, L. A.; Schurko, R. W. *J. Magn. Reson*. **2011**, *208*, 103.

(14) Lucier, B. E. G.; Reidel, A. R.; Schurko, R. W. *Canadian Journal of Chemistry* **2011**, *89*, 919.

(15) Harris, K. J.; Lupulescu, A.; Lucier, B. E.; Frydman, L.; Schurko, R. W. *Journal of Magnetic Resonance* **2012**, *224*, 38.

(16) Slichter, C. P. *Principle of Magnetic Resonance* (Harper and Row, New York, N.Y **1963**).

(17) Kupce, E.; Freeman, R. *J. Magn. Reson. A* **1995**, *115,* 273.

(18) Siegel, R.; Nakashima, T. T.; Wasylishen, R. E. *Journal Of Physical Chemistry B* 2004, *108*, 2218.

(19) Bhattacharyyra, R.; Frydman, L. *J. Chem. Phys.* **2007***, 127,* 194503.

(20) Tong, Y.; Rice, C.; Wieckowski, A.; Oldfield, E. *Journal of the American Chemical Society* **2000**, *122*, 11921.

(21) Traficante, D. D. *Concepts in Magnetic Resonance* **1993**, *5*, 57.

(22) Rath, A. R. *Magnetic Resonance in Medicine* **1990**, *13*, 370.

(23) Borodko, Y.; Somorjai, G. A. *Applied Catalysis A: General* **1999**, *186*, 355.

(24) Becerra, L.; Klug, C.; Slichter, C. *J. Phys. Chem.* **1993**, *97*, 12014

(25) Yahnke, M.; Rush, B.; Reimer, J.; Cairns, E. *J. Am. Chem. Soc* **1996**, *118*, 12250.

(26) Shoemaker, R. K.; Apple, T. M. *J. Phys. Chem.* **1985**, *89*, 3185.